

Institut de Physique de l'Université de Neuchâtel (Suisse)



# Probing nanoscale ferroelectricity by photoelectron diffraction

Thèse

Présentée à la Faculté des Sciences  
de l'Université de Neuchâtel

Pour l'obtention du grade de Docteur ès Sciences

Par

**Laurent Despont**

Soutenue le 2 avril 2007

En présence du directeur de thèse

Prof. Philipp Aebi

et des rapporteurs

Prof. Jean-Marc Triscone et Prof. Christophe Ballif

Neuchâtel, 2007



## IMPRIMATUR POUR LA THESE

# Probing nanoscale ferroelectricity by photoelectron diffraction

## Laurent DESPONT

---

UNIVERSITE DE NEUCHATEL

FACULTE DES SCIENCES

La Faculté des sciences de l'Université de Neuchâtel,  
sur le rapport des membres du jury

MM. P. Aebi (directeur de thèse),  
C. Ballif et J.-M. Triscone (Genève)

autorise l'impression de la présente thèse.

Neuchâtel, le 18 juin 2007

Le doyen :  
T. Ward

UNIVERSITE DE NEUCHATEL  
FACULTE DES SCIENCES  
Secrétariat-Décanat de la faculté  
Rue Emile-Argand 11 - CP 158  
CH-2009 Neuchâtel



# Contents

<b>Preface</b>	<b>9</b>
List of acronyms used throughout this work . . . . .	12
<b>Introduction</b>	<b>13</b>
<b>1 Introduction to ferroelectricity</b>	<b>15</b>
1.1 General remarks . . . . .	15
1.2 Origin of the ferroelectric instability . . . . .	16
1.3 Ferroelectric finite size-effect . . . . .	18
References for chapter 1 . . . . .	19
<b>2 Experimental techniques</b>	<b>21</b>
2.1 Introduction . . . . .	21
2.2 X-ray photoelectron spectroscopy . . . . .	22
2.3 X-ray photoelectron diffraction . . . . .	24
References for chapter 2 . . . . .	25
<b>3 Multiple scattering calculations</b>	<b>27</b>
3.1 Introduction . . . . .	27
3.2 EDAC: General remarks . . . . .	28
3.2.1 Introduction . . . . .	28
3.2.2 Calculation procedure coupled with the reliability factor . . . . .	29
References for section 3.2 . . . . .	34
3.3 X-ray photoelectron diffraction study of Cu(111): Multiple scattering investigation	37
3.3.1 Introduction . . . . .	37
3.3.2 Experimental and Computational Details . . . . .	38
3.3.3 Results and Discussion . . . . .	39
3.3.4 Conclusion . . . . .	44
References for section 3.3 . . . . .	44
3.4 Multiple scattering investigation of the $1T$ -TaS <sub>2</sub> surface termination . . . . .	47
3.4.1 Introduction . . . . .	47
3.4.2 Experimental and computational details . . . . .	48
3.4.3 Results and discussion . . . . .	49
3.4.4 Conclusion . . . . .	55

References for section 3.4 . . . . .	56
3.5 InN surface polarity investigated by single scattering . . . . .	59
3.5.1 Introduction . . . . .	59
3.5.2 Experimental and computational details . . . . .	59
3.5.3 Results and discussion . . . . .	60
References for 3.5 . . . . .	61
<b>4 Local structure of Nb-SrTiO<sub>3</sub></b> . . . . .	<b>63</b>
4.1 Introduction . . . . .	63
4.2 X-ray photoelectron diffraction on Nb-SrTiO <sub>3</sub> . . . . .	64
4.2.1 Experimental results . . . . .	64
4.2.2 Multiple scattering investigation . . . . .	65
4.3 Nb-SrTiO <sub>3</sub> surface reconstruction . . . . .	65
References for chapter 4 . . . . .	69
<b>5 Structural and spectroscopic investigation of PbTiO<sub>3</sub> films</b> . . . . .	<b>71</b>
5.1 General remarks . . . . .	71
References for section 5.1 . . . . .	72
5.2 X-ray photoelectron diffraction study of ultrathin PbTiO <sub>3</sub> films . . . . .	73
5.2.1 Introduction . . . . .	73
5.2.2 Experimental and computational details . . . . .	74
5.2.3 Results and Discussion . . . . .	77
5.2.4 Conclusion . . . . .	81
References for section 5.2 . . . . .	81
5.3 Direct evidence for ferroelectric polar distortion in ultrathin lead titanate perovskite films . . . . .	85
5.3.1 Introduction . . . . .	85
5.3.2 Ferroelectric distortion versus surface relaxation . . . . .	87
5.3.3 Experimental results and discussion . . . . .	89
5.3.4 Conclusion . . . . .	94
References for section 5.3 . . . . .	94
5.4 Investigation of effective screening length in ferroelectrics by photoemission . . . . .	97
5.4.1 Introduction . . . . .	97
5.4.2 Experiments . . . . .	97
5.4.3 Results and discussion . . . . .	99
5.4.4 Conclusion . . . . .	101
References for 5.4 . . . . .	102
5.5 Influence of the boundary conditions . . . . .	105
5.5.1 Local structure investigation of SrTiO <sub>3</sub> /PbTiO <sub>3</sub> superlattices . . . . .	105
5.5.2 PbTiO <sub>3</sub> on La <sub>0.67</sub> Sr <sub>0.33</sub> MnO <sub>3</sub> . . . . .	107
5.5.3 Ferroelectric polarization switching using XPD . . . . .	108
5.5.4 Reversible PbTiO <sub>3</sub> surface states, applying O and H plasma . . . . .	109
5.5.5 Monodomain to polydomain transition in ferroelectric PbTiO <sub>3</sub> thin films on SrRuO <sub>3</sub> substrates. . . . .	111
5.5.6 How to obtain LEED patterns of PbTiO <sub>3</sub> surfaces? . . . . .	114

---

References for section 5.5 . . . . .	116
5.6 Antiferrodistortive distortion at the (001) $\text{PbTiO}_3$ surface . . . . .	119
5.6.1 Basic notions . . . . .	119
5.6.2 MSC analysis . . . . .	119
References for section 5.6 . . . . .	121
<b>6 Conclusions and future perspectives</b>	<b>123</b>
<b>A MSC shell script example</b>	<b>125</b>
<b>B MSC calculated diffraction patterns for <math>\text{Cu}(111)</math> surface</b>	<b>129</b>
<b>C <math>\text{Nb-SrTiO}_3</math> (<math>4 \times 2</math>) multi-domain surface reconstruction</b>	<b>133</b>
<b>D Plasma characterization</b>	<b>135</b>
D.1 Introduction . . . . .	135
D.2 How the ion analyzer works and how to calibrate the plasma . . . . .	135
D.3 Results and discussion . . . . .	136
D.4 Cleaning parameters for the $\text{PbTiO}_3$ surface preparation . . . . .	139
References for Appendix D . . . . .	139
<b>Acknowledgements</b>	<b>141</b>
<b>Curriculum vitae</b>	<b>143</b>



## Preface

This thesis is based on research carried out at the *Institut de Physique, Université de Neuchâtel, Neuchâtel, Switzerland* during the period 2003 - 2007, in collaboration with the *DPMC, University of Geneva*, where the samples have been grown. It consists of six different chapters and four appendices. The chapters 3 and 5 contain sections from independent articles. Therefore, these sections stand completely on their own with an abstract, introduction, and an experimental section. This allows the reader to study these sections independently and in any order, with no loss of continuity, depending on the personal interest. For sequential reading, this leads to some redundancy concerning the introductions and the descriptions of experimental procedures. These parts may therefore be skipped.

The first chapter gives an introduction to the ferroelectricity. It explains shortly the concept of phonon softening which is at the origin of the ferroelectric instability but also why this instability can be suppressed in very thin films. The notion of ferroelectric charge screening is explained together with the origin of the depolarizing field.

The second chapter is dedicated to the photoemission techniques used in this thesis, namely the x-ray photoelectron spectroscopy, as a probe of the *electronic structure*, and the x-ray photoelectron diffraction, that provides the *local atomic structure* around a given atom.

The third chapter deals with the theoretical approach of the photoelectron diffraction. Here a new code taking into account multiple scattering events is described and the main parameters used in the multiple scattering program are discussed. The first part of this chapter has been arranged as a tool for further multiple scattering investigations. In the second part, differences and similarities between single and multiple scattering are discussed for the Cu(111) surface for two different photoelectron kinetic energies. Then the  $1T$ -TaS<sub>2</sub> surface termination has been investigated using the multiple scattering approach and the application of this method to other similar systems is discussed. Finally, using single scattering calculations have been used in order to determine the polarity of an InN(0001) surface. The aim of all these examples is to show, despite some limitations, the utilization domain of scattering calculations.

In the fourth chapter we report an analysis of the Nb-SrTiO<sub>3</sub> which has been mainly employed as substrate for the ferroelectric films studied in the fifth chapter. A multiple scattering based structure optimization of the substrate suggests that, contrary to long-established beliefs, its surface is not paraelectric but exhibits a polar distortion analogous to the one observed in ferroelectric films. In this chapter, we also emphasize some aspects regarding the surface reconstruction and the chemistry at the Nb-SrTiO<sub>3</sub> surface according to different cleaning procedures.

The fifth chapter consists of a wide investigation of ferroelectric PbTiO<sub>3</sub> films. The ferroelectricity is typically regarded as a collective phenomenon and is consequently expected to be strongly influenced by finite-size and surface effects. Both of these aspects are investigated in this chapter. First the intra-cell polar atomic distortion and the tetragonality associated with the ferroelectricity have been explored leading to information about the non-centro-symmetry in films a few unit cell thick, the preservation of the ferroelectricity in films as thin as 3 unit

cell and the influence of the surface relaxation on the ferroelectric distortion switchability. Second, the environment of the PbTiO<sub>3</sub> films has been modified, either by changing the interface/substrate (La<sub>0.67</sub>Sr<sub>0.33</sub>MnO<sub>3</sub> and SrRuO<sub>3</sub>), the surface boundary conditions using plasma based cleaning procedures for instance, or even both using a superlattice configuration made of alternated layers of PbTiO<sub>3</sub> and SrTiO<sub>3</sub>. Finally, we have suggested a way to understand an unexpected behavior of XPS line positions as a function of the film thickness, combining XPS and XPD measurements together with an electrostatic model. This approach could be used to determine the effective screening length characterizing the screening efficiency of electrode materials.

The appendix brings together different practical hints for the utilization of a conventional multiple scattering shell script, for the Nb-SrTiO<sub>3</sub> (4 × 2) multi-domain surface reconstruction preparation or the plasma characterization.

Some results presented in this thesis have been published in the following articles<sup>a</sup>:

- **X-ray photoelectron diffraction study of Cu(111): Multiple scattering investigation**  
L. Despont, D. Naumović, F. Clerc, C. Koitzsch, M. G. Garnier, F. J. Garcia de Abajo, M. A. Van Hove and P. Aebi ,  
*Surf. Sci.* **600**, 380-385 (2006)
- **Multiple scattering investigation of the 1T-TaS<sub>2</sub> surface termination**  
L. Despont, F. Clerc, M. G. Garnier, H. Berger, L. Forró and P. Aebi,  
*Eur. Phys. J. B* **52**, 421-426 (2006)
- **X-ray photoelectron diffraction study of ultrathin PbTiO<sub>3</sub> films**  
L. Despont, C. Lichtensteiger, F. Clerc, M. G. Garnier, F. J. Garcia de Abajo, M. A. Van Hove, J.-M. Triscone and P. Aebi,  
*Eur. Phys. J. B* **49**, 141-146 (2006)  
♣ Highlighted in *Europhysics News* **37**, No 3 (2006)
- **Direct evidence for ferroelectric polar distortion in ultrathin lead titanate perovskite films**  
L. Despont, C. Lichtensteiger, C. Koitzsch, F. Clerc, M. G. Garnier, F. J. Garcia de Abajo, E. Bousquet, P. Ghosez, J.-M. Triscone and P. Aebi,  
*Phys. Rev. B* **73**, 094110 (2006)
- **Investigation of effective screening length in ferroelectrics by photoemission**  
L. Despont, C. Monney, C. Battaglia, H. Cercellier, M. G. Garnier, C. Lichtensteiger, M.

---

<sup>a</sup>Please note that the references for the publications are placed at the end of the respective paper!

Dawber, J.-M. Triscone and P. Aebi,  
*To be submitted (2007).*

- **Monodomain to polydomain transition in ferroelectric PbTiO<sub>3</sub> thin films with La<sub>0.67</sub>Sr<sub>0.33</sub>MnO<sub>3</sub> electrodes**

C. Lichtensteiger, M. Dawber, N. Stucki, J.-M. Triscone, J. Hoffman, J.-B. Yau, C. H. Ahn, L. Despont and P. Aebi,  
*Appl. Phys. Lett.* **90**, 052907 (2007)

- **Structural investigations of epitaxial InN by X-ray photoelectron diffraction and X-ray diffraction**

D. Hofstetter, L. Despont, M. G. Garnier, E. Baumann, F. R. Giorgetta, P. Aebi, L. Kirste, H. Lu and W. J. Schaff,  
*Appl. Phys. Lett.* **90**, 191912 (2007)

## List of acronyms used throughout this work

AFD	antiferrodistortive
AFM	atomic force microscope
ARPES	angle-resolved photoelectron spectroscopy
$E_B$	binding energy
$E_F$	Fermi energy
$E_V$	vacuum level
FF	forward focusing
imfp	inelastic mean free path
LEED	low energy electron diffraction
LSMO	$\text{La}_{0.67}\text{Sr}_{0.33}\text{MnO}_3$
MSC	multiple scattering
MT	muffin-tin
PFM	piezoresponse mode of the atomic force microscopy
PTO	$\text{PbTiO}_3$
R-factor	reliability factor
RT	room temperature
SSC	single scattering
SRO	$\text{SrRuO}_3$
STO	$\text{SrTiO}_3$
UHV	ultra-high vacuum
UPS	ultraviolet photoelectron spectroscopy
XPD	x-ray photoelectron diffraction
XPS	x-ray photoelectron spectroscopy
XRD	x-ray diffraction

## Introduction

A ferroelectric is generally defined as a material with two or more stable states of different non-zero intrinsic lattice polarization  $P$  which can be reversed through the application of an external electric field  $E$  greater than the coercive field  $E_c$ . An external electric field of  $\approx 50$  kV/cm is required to reverse the polarization of a typical ferroelectric. In order to integrate ferroelectric material in most electronic applications (silicon chips  $\leq 5V$ ), submicrometer film thicknesses are needed, which is no longer a problem thanks to various deposition techniques.

The information storage in ferroelectric random access memories (FeRAM) is a quite evident and interesting application for such materials but requires a wide technical know-how to achieve a mass production comparable to the ongoing "flash memory" fabrication. However, nowadays FeRAM are already commercially utilized (for instance by Fujitsu in the SONY Playstation 2). The difficulties to reduce the flash memory operating voltage, from 5V at present to 0.5V in the near future, could help to develop the utilization of FeRAM at large scale by simply reducing the ferroelectric film thickness.

The semiconducting field-effect transistors (FETs), based on the manipulation of charge carrier densities, are widely used in modern electronics, such as in cellular phones, computers, cars, etc. The main idea is to modulate the charge densities, and thus the electrical resistance through the application of an electric field. However, the best polarization obtained using  $\text{SiO}_2$  in oxides FETs is rather small ( $3\mu\text{C}/\text{cm}^2$ ) compared to ferroelectric oxides ( $10\text{-}80\mu\text{C}/\text{cm}^2$ ), which limits the carrier density modulation. The utilization of ferroelectric oxide could thus be used to increase the efficiency of field-effect transistors.

Other short-term applications could arise using ferroelectric materials. For instance during the switching, the ferroelectrics emit a large number of electrons from their surface. Larger current, lifetimes and their instantaneous ignition make ferroelectric electron emitters more efficient than conventional thermionic cathodes, and can be used for miniaturized x-ray sources. The ferroelectrics also reveal an electrocaloric effect (pyroelectric). In other words, by applying an electric field to them, it is possible to reduce their temperature ( $\Delta T = 12K$  at  $25V$  across  $350\text{nm}$  of  $\text{PbZr}_{0.95}\text{Ti}_{0.05}\text{O}_3$ ). This temperature gradient is sufficient to design CPU coolers. Finally, similarly to carbon nanotubes (either metallic or semiconducting), applications of ferroelectric nanotubes (insulating) have been investigated. For instance, when a voltage is applied to them, they expand, contract or bend (piezoelectric), making them suitable for nanoscale devices (ink-jet printers, control of molecular species, nanoscale delivery vehicles).

Despite the evident potential of ferroelectric materials and most specifically of thin ferroelectric films, some questions concerning their limitations remain open. One of them consists in whether or not ferroelectricity can be maintained at reduced dimensions and represents the main topic of this thesis.

At the same time to the development and the miniaturization of electronic devices, surface science has become an intense field of research. Indeed surfaces constitute the boundaries of condensed matter, solids and liquids and have a main importance for catalysis, corrosion, lubrication, adhesion, crystal growth, as well as in integrated circuits, food packing and cosmetics.

Owing to the refinement of measurement techniques, it is nowadays possible to "see" single atoms or molecules adsorbed on a surface and even to displace and rearrange them one by one. As a consequence to this development, the scientific knowledge is rapidly expanding which in turns permits to fabricate even smaller/more efficient electronic devices.

Not only the advance of the measurement techniques but also progresses of theoretical models are often coupled with improvements in the understanding of physical behaviors. It is clear that to better reproduce the complexity of physical behaviors, specially in extrem conditions like it is the case for very thin films, the calculation algorithms become more and more elaborate and thus computer demanding.

All these aspects are interrelated. A deeper understanding of physical behaviors leads to progresses in measurement techniques, electronic devices miniaturization or CPU performances, and inversely. I hope that the new data obtained in this thesis will stimulate further photoemission investigations in the fascinating and important field of the ferroelectrics at reduced dimension.

# Chapter 1

## Introduction to ferroelectricity

### 1.1 General remarks

Ferroelectric materials are pyroelectrics<sup>a</sup> with two or more stable states with nonzero remanent polarizations. Using an electric field larger than the coercive field<sup>b</sup>, it is possible to switch between the different ferroelectric states. The spontaneous polarization can be atomically visualized using negative and positive ions whose centers of charge do not coincide. Above the Curie temperature<sup>c</sup>, the crystal structure of most ferroelectric materials is based on the centro-symmetric  $ABO_3$  cubic perovskite composed by mono- or di-valent A atoms, tetra- or penta-valent B atoms and O atoms (Fig. 1.1). But below the Curie temperature, the structure is slightly distorted permitting to consider the spontaneous polarization as due to an assembly of electric dipoles made of positive and negative ion pairs<sup>d</sup>. Note that, depending on their components, the ferroelectric structure can undergo different phase transitions when the temperature is lowered. For instance,  $BaTiO_3$ , as well as  $KNbO_3$  have three different ferroelectric phase transitions, from cubic to slightly distorted structures successively of tetragonal, orthorhombic and rhombohedral symmetry. Some other ferroelectric perovskites have only one phase transition from cubic to a tetragonal state, like  $PbTiO_3$ .

The magnitude of the electric field requested for switching the spontaneous polarization is proportional to the ferroelectric film thickness (several  $V/\mu m$ ), making thin films suitable for electronic applications such as non-volatile memory (FRAM), thermal infrared pyroelectric detectors, surface acoustic wave filters used in telecommunications, ultrasonic sensors for medical imaging and many others.

In parallel, the understanding of fundamental aspects of the ferroelectricity at low dimension still evolves with new measurement methods and new theoretical refinements. The ferroelectricity has been regarded as a collective phenomenon associated with the electric dipole alignment

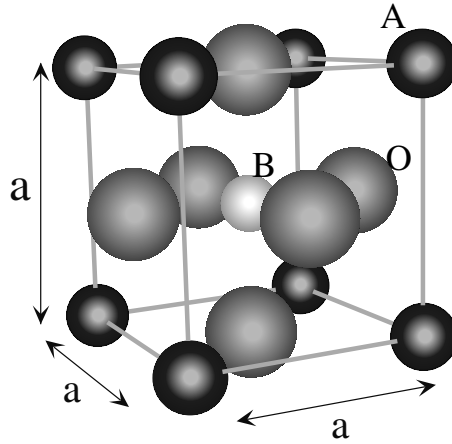
---

<sup>a</sup>The pyroelectricity is the property of a class of materials which change their polarization proportionally to their temperature.

<sup>b</sup>Typically of the order of several  $kV/cm$ .

<sup>c</sup>The Curie temperature defines the temperature above which the crystal is no longer ferroelectric.

<sup>d</sup>Note that the total polarization is composed of the ionic polarization owing to ion displacement but also of the electronic polarization due to the electronic shell displacement with respect to the positive nucleus.

Figure 1.1: Cubic general  $ABO_3$  perovskite structure.

over a large volume. It has been argued for many years that the ferroelectric phase is suppressed below a relatively large critical volume due to the limitation of the long-range Coulomb interactions responsible of the ferroelectric phase stabilization. Nevertheless, since 1998, many experimental [1–3] and theoretical [4–7] results show that the real critical volume below which the ferroelectric phase disappears is in fact much smaller than expected, presumably due to the electrostatic boundary conditions.

The ferroelectric surface and interface analysis is thus of great importance to improve the understanding of the ferroelectric behavior. Due to both its extremely high surface sensitivity and its chemical sensitivity, x-ray photoelectron diffraction appears like an unescapable tool for the nanoscale ferroelectricity analysis.

## 1.2 Origin of the ferroelectric instability

Above the Curie temperature, the atoms primarily occupy the ideal centro-symmetric sites (no polarization) but when the temperature is reduced below the Curie temperature, the centro-symmetric structure becomes unstable and a ferroelectric distortion appears. The free energy as a function of the polarization is shown in Fig. 1.2 for three different temperatures. For  $T > T_C$ , the free energy minimum is obtained for a centro-symmetric structure and thus a paraelectric state, while for  $T < T_C$ , a double well shape of the free energy appears, with two possible minima for two equivalent structure distortions corresponding to the ferroelectric state. This structure modification can be explained by the "soft-mode" picture. Here we attempt to explain shortly the concept of phonon softening. Note that this phase transition is equivalent to a second-order Jahn-Teller effect (terminology used by chemists and some physicists).

Two different electronic shell hybridizations occur in PTO. The most common hybridization in perovskite oxides occurs between transition metal states, here the Ti 3d, and the O 2p states. The Ti-O hybridization appears as essential for the ferroelectric instability. In parallel, the  $ns^2$  electron configuration of the  $Pb^{2+}$  permits to create partially covalent Pb-O bonds. The effective

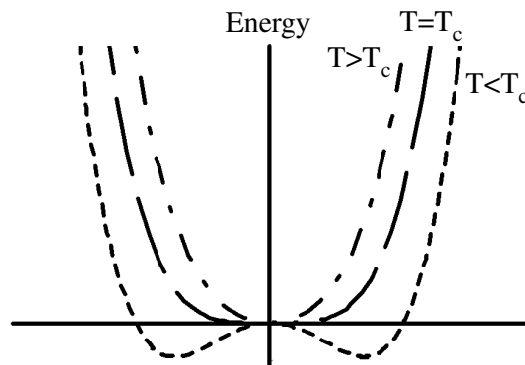


Figure 1.2: Free energy as a function of the polarization at  $T > T_C$ ,  $T = T_C$  and  $T < T_C$ .

static charges associated to each atom are drastically modified by these hybridizations and are difficult to quantify. However the dynamical charge defined by the change of polarization induced by the atomic displacement, called the Born effective charge  $Z^*$ , appears as a more fundamental quantity. It allows to visualize the mechanism of polarization as electronic currents produced by dynamical changes of orbital hybridizations. The effective charge  $Z^*$  can be used to predict the spontaneous polarization in ferroelectric material.

The phonon frequencies can be deduced from a classic dynamical matrix calculation. In this calculation, the phonon frequencies correspond to the eigenvalues of the dynamical matrix obtained by the second derivative of the potential (including the long-range Coulomb (dipole-dipole) interaction proportional to  $Z^*$ ) as a function of the eigendisplacements. The eigenvectors associated with the eigenvalues permit to distinguish the longitudinal (LO) and transversal (TO) optical modes.

The phonon dispersion calculated for a simple cubic PTO structure reveals imaginary frequencies for the TO modes [8]. This special feature has significant implications regarding the properties of the system, like allowing to associate the ferroelectric instability to the lattice dynamic. Indeed, if the calculated phonon frequency tends to zero ("soft-mode") or becomes imaginary, it means that the structure included in the calculation is not stable. To obtain a stable system, the structure has to be modified. The stabilization is reached for a non-centrosymmetric structure which induces the creation of a dipole moment. As the dynamical charge  $Z^*$  is directly related to the change of polarization created by the atomic displacement, it reflects how the system reacts when a structure distortion occurs. In fact, anomalously large  $Z^*$  values are found in the literature and seem to be a general feature of perovskite compounds [8–10]. This leads to large spontaneous polarization for small distortions.

For the particular PTO case, the calculation of the eigenvectors shows that the Ti atoms are displaced against the O along the Ti-O chains and that Pb atoms move against the O in the Pb-O planes. Moreover an antiferrodistortive instability (cooperative rotation of the O octahedra) appears in *ab initio* calculations which reveal a strong correlation in the plane perpendicular to the axis of rotation [8].

### 1.3 Ferroelectric finite size-effect

The ferroelectricity is a collective phenomena thus sensitive to the system dimension. For instance, by decreasing the thickness of a ferroelectric film, we act on the long-range Coulomb interactions which are essential in the ferroelectric phase stabilization. Indeed, the polarization creates charges at the ferroelectric surface and compensation charges provided by electrodes are required in order to stabilize the ferroelectric ground state.

Using perfect electrodes, these charges can be completely screened at the electrode-ferroelectric interface. However, real electrodes can not entirely screen the polarization charges at the physical interface. In fact, using real electrodes, the screening charge plane is displaced relative to the ferroelectric-electrode interface by a distance called the *effective screening length*  $\lambda^{eff}$  and consequently a net charge is created at the interface, as illustrates in Fig. 1.3. This uncompensated charge is at the origin of the depolarizing field at the ferroelectric film boundaries which could be large enough to suppress the ferroelectric instability in very thin films [11].

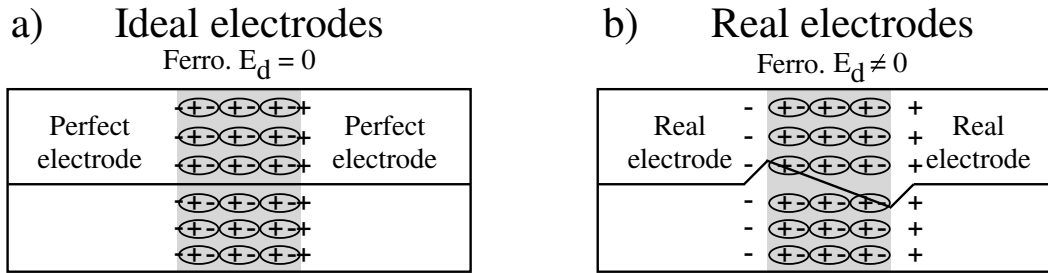


Figure 1.3: Depolarizing fields  $E_d$  for ideal (a) and real electrodes (b). The solid line corresponds to the uncompensated electrostatic potential.

A simple electrostatic model based on the compensation charges induced by real electrodes and on the incomplete cancellation of polarization shows that the depolarizing field amplitude depends only on three parameters: the ferroelectric distortion (proportional to the bulk spontaneous polarization), the effective screening length and the ferroelectric film thickness. The electrostatic model developed in Ref. [12] has been applied here to the  $\text{PbTiO}_3$  ( $P_S = 83 \mu\text{C}/\text{cm}^2$  and  $\lambda^{eff} = 0.12 \text{ \AA}$  [13]) and the results are illustrated in Fig. 1.4 a and b.

The figures show that the depolarizing field increases linearly when the atomic displacement relative to the centro-symmetric state increases (a) and that the depolarizing field is inversely proportional to the film thickness (b) and demonstrates its crucial role for the ferroelectricity suppression at finite size. Furthermore, it also illustrates that even above the critical thickness below which the ferroelectricity disappears, a non-zero depolarizing field tends to reduce the amplitude of the spontaneous polarization.

Note that at the interface region, atomic relaxations occur which tend to modify structure parameters by (i) interplanar distance reduction (compression) or increase (extension) and (ii) atomic rumpling [14]. The rumpling describes the individual ion displacement relative to the mean position of each atomic plane given by the interplanar relaxation. This phenomenon will be widely explained in Section 5.3.

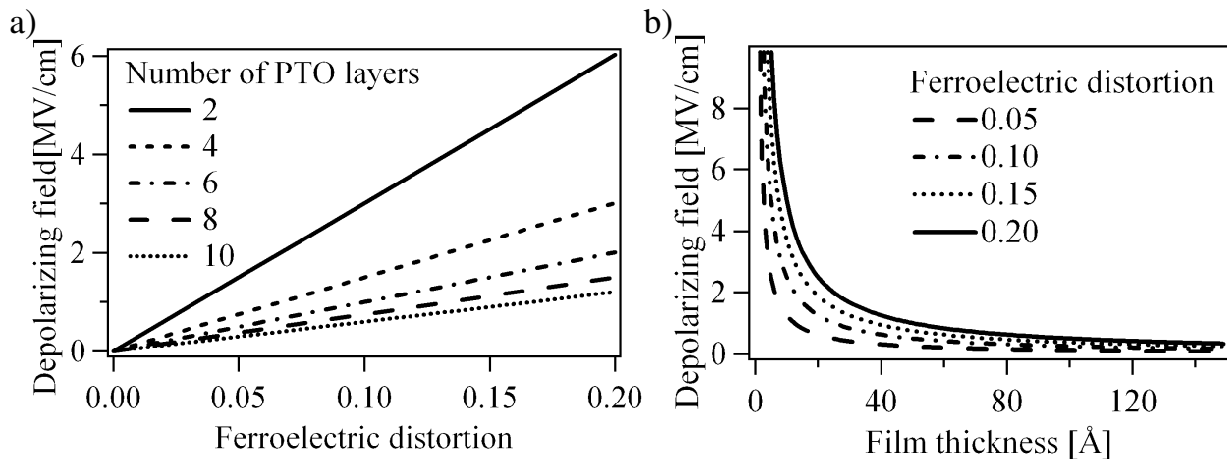


Figure 1.4: (a) Evolution of the depolarizing field as a function of the ferroelectric distortion for different film thicknesses. The paraelectric state corresponds to a ferroelectric distortion equivalent to 0 while the bulk tetragonal ferroelectric phase corresponds to 1. (b) Evolution of the depolarizing field as a function of the film thickness for different ferroelectric distortions.

## References for chapter 1

- [1] T. Tybell, C. H. Ahn, and J.-M. Triscone, *Appl. Phys. Lett.* **75**, 856 (1999).
- [2] S. K. Streiffer, J. A. Eastman, D. D. Fong, C. Thompson, A. Munkholm, M. V. Ramana Murty, O. Auciello, G.R. Bai and G.B. Stephenson, *Phys. Rev. Lett.* **89**, 067601 (2002).
- [3] D. D. Fong, G. B. Stephenson, S. K. Streiffer, J. A. Eastman, O. Auciello, P. H. Fuoss and C. Thompson, *Science* **304**, 1650 (2004).
- [4] P. Ghosez and K. M. Rabe, *Appl. Phys. Lett.* **76**, 2767 (2000).
- [5] B. Meyer and D. Vanderbilt, *Phys. Rev. B* **63**, 205426 (2001).
- [6] J. Junquera and P. Ghosez, *Nature* **422**, 506 (2003).
- [7] N. Sai, A. M. Kolpak and A. M. Rappe, *Phys. Rev. B* **72**, 020101(R) (2005).
- [8] Ph. Ghosez, E. Cockayne, U. V. Waghmare and K. M. Rabe, *Phys. Rev. B* **60**, 836 (1999).
- [9] W. Zhong, R. D. King-Smith and D. Vanderbilt, *Phys. Rev. Lett.* **72**, 3618 (1994).
- [10] G. Sági-Szabó, R. E. Cohen and H. Krakauer, *Phys. Rev. Lett.* **80**, 4321 (1998).
- [11] J. Junquera and Ph. Ghosez, *Nature* **422** 506 (2003).
- [12] Ph. Ghosez and J. Junquera, *Handbook of theoretical and computational nanotechnology*, Vol. 9, Chapter 134, American Scientific Publishers, Stevenson Ranch, USA, (2006).

- [13] C. Lichtensteiger, J.-M. Triscone, J. Junquera and P. Ghosez, *Phys. Rev. Lett.* **94**, 047603 (2005).
- [14] B. Meyer, J. Padilla and D. Vanderbilt, *Faraday Discuss.*, **144** 395 (1999).

# Chapter 2

## Experimental techniques

### 2.1 Introduction

The photoelectric effect has been discovered by Heinrich Hertz in 1887 [1] and explained 18 years later by Albert Einstein [2] by appealing for the first time the quantum nature of light, for which he received the Nobel Prize (1921). The photoelectron spectroscopy is based on this photoelectric effect. In 1924, Karl Manne Georg Siegbahn received the Nobel Prize for his research work mainly devoted to x-ray spectroscopy.

A typical photoelectron experiment is sketched in Fig. 2.1. The sample is illuminated by a photon beam of an ideally monochromatic energy  $h\nu$ . In penetrating the sample, the photons give their energy to the electrons which are excited into higher previously unoccupied energy final states. If the excited electron energy is larger than the vacuum level potential barrier, they are ejected in the vacuum and some of them are collected in the analyzer as a function of their kinetic energy at a given  $(\theta, \phi)$  angular set. The sample, usually metallic or semiconducting, is grounded in order to avoid charge effects. As will be shown further, thin insulating films on conducting substrates can be also measured with this method.

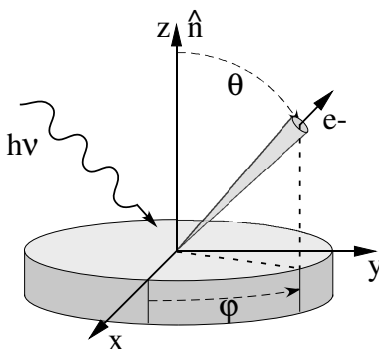


Figure 2.1: Scheme of a photoemission experiment. The sample is illuminated by light of a given energy  $h\nu$ . The excited electrons are ejected and collected in the detector.

Usually, two photon energy regimes are considered, ultraviolet photoelectron spectroscopy (UPS) where photons of low energy (less than 50eV) probe valence electrons and x-ray photoelectron spectroscopy (XPS) where photons of higher energy (up to 2000eV) probe mostly the non-dispersive core levels allowing for surface chemical analysis. The light used for the XPS energy range is usually obtained by the transition of a L shell electron into an unoccupied K shell. This desexcitation process generates  $K\alpha$  radiation whose energy depends on the material in which the desexcitation takes place. The most commonly used materials are aluminium( $h\nu=1486\text{eV}$ ) and magnesium( $h\nu=1256.3\text{eV}$ ) for which the line width is small. Silicon( $h\nu=1740\text{eV}$ ) is less widespread.

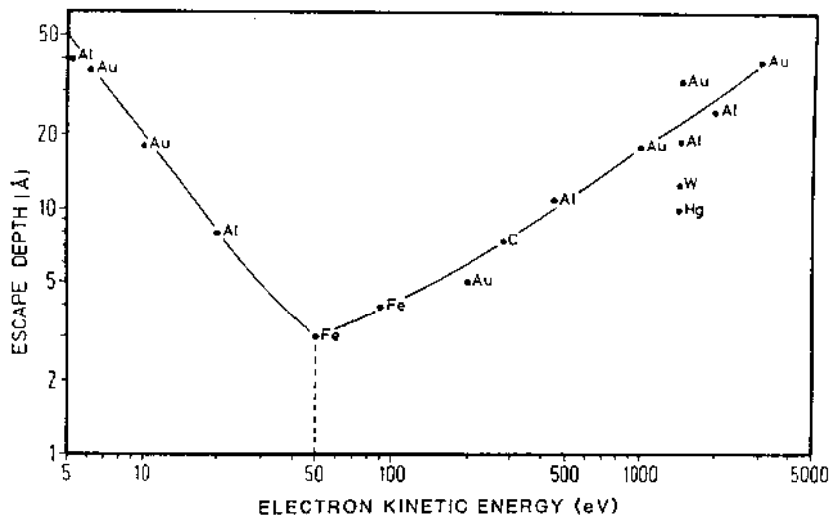


Figure 2.2: Electrons escape depth as a function of their kinetic energy, for various metals. The line represents a universal curve, the data being spreaded around this line. [3]

Fig. 2.2 illustrates the surface sensitivity of the photoemission experiment in the considered energy regime, reflected by the inelastic mean free path (imfp). In the conventional photoelectron kinetic energy range (20eV-2000eV), the imfp takes values between approximately 10 and 40Å . The minimum imfp corresponds to electrons with a kinetic energy around 50eV. This small escape depth is typical for electrons and is a keypoint of the photoelectron spectroscopy. Moreover, electrons can easily be focused, accelerated and detected.

The next two sections describe first the basis of the photoemission process illustrated by the three step model and second the particular case of the angle-resolved photoemission.

## 2.2 X-ray photoelectron spectroscopy

The semiclassical "three step model", which is the most commonly used interpretation of the photoemission process, distinguishes three distinct steps.

- The photon induced excitation of an electron from an occupied initial state to higher previously unoccupied final states, labeled with (1) in Fig. 2.3a.
- The electron travel through the crystal towards the sample surface with simultaneous creation of secondary electrons (2).
- The transmission through the surface potential barrier to the vacuum (3).

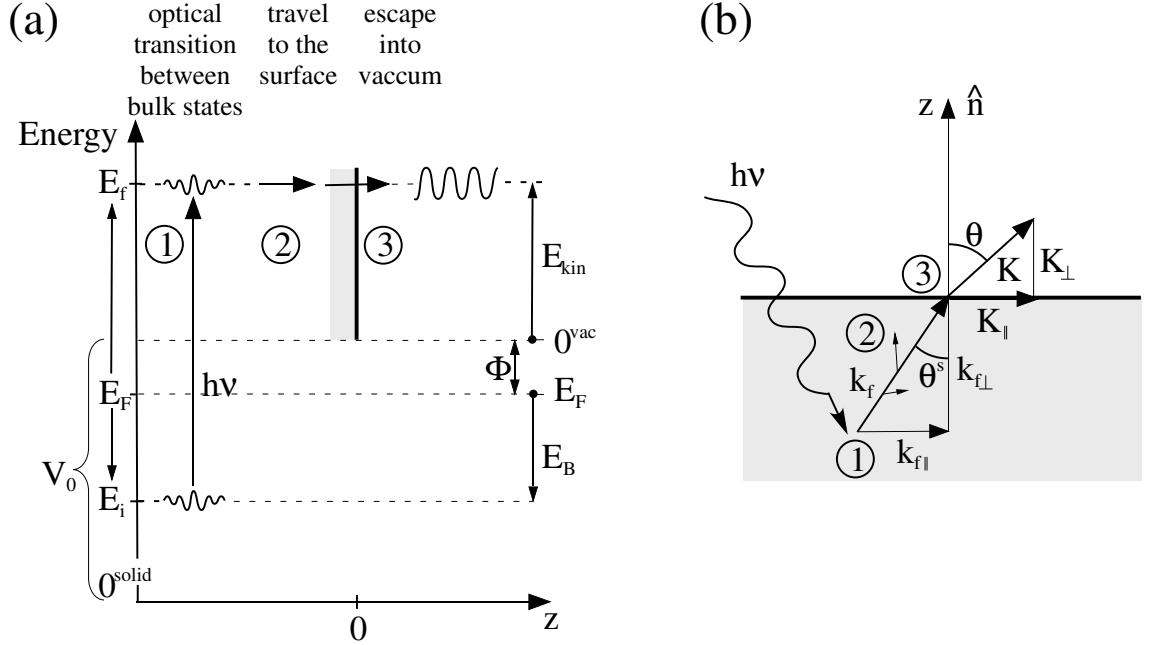


Figure 2.3: (a) Scheme of the three step model [3].1: Photoexcitation 2: Travel to the surface 3: Escape into the vacuum. (b) Illustration of the photoelectron momentum vector refraction at the solid surface.

(1) An electron in its initial state  $|i\rangle$  with energy  $E_i$  is excited by a photon of a given energy  $h\nu$  which induces the transition of the electron to a final state  $|f\rangle$  with energy  $E_f$ . The optical transition related to the photon absorption can be described by the following Fermi's golden rule:

$$\omega_{if} \propto |\langle f | H_{int} | i \rangle|^2 \delta(E_f - E_i - h\nu) \quad (2.1)$$

where the  $H_{int}$  is the Hamiltonian describing the interaction between the electron and the electromagnetic field (the photon) and  $\delta$  insures the energy conservation.

$$H_{int} = \frac{e}{2mc} (\vec{A} \cdot \vec{p} + \vec{p} \cdot \vec{A}) \quad (2.2)$$

where  $\vec{A} = \vec{A}_0 e^{i\vec{q}\cdot\vec{r}}$  is the electrostatic potential vector and  $\vec{p} = -i\hbar\vec{\nabla}$  is the electronic momentum operator.

(2) The electron travelling towards the surface undergoes electron-electron scattering. This scattering limits the number of electrons reaching the surface and creates an electronic background due to the multiple inelastic events.

(3) The last step consists of the transit of the electron through the surface. To escape into the vacuum, the electron has to overcome the surface potential barrier  $\Phi$ . Moreover the kinetic energy part correlated to the perpendicular component of the momentum,  $\frac{\hbar^2}{2m}k_{f\perp}^2$ , has to be larger than the surface potential step  $V_0$ . The Fig. 2.3b illustrates the transit through the surface under the condition of parallel momentum conservation,  $\vec{k}_{f\parallel} = \vec{K}_{\parallel}$ . However the momentum component perpendicular to the surface is not conserved, as the photoelectron is refracted when passing through the surface. There are two relationships between the photoelectron kinetic energy and its parallel and perpendicular momentum components,  $K_{\parallel} = \frac{\sqrt{2mE_{kin}}}{\hbar} \sin\theta$  and  $K_{\perp} = \frac{\sqrt{2mE_{kin}\cos^2\theta - V_0}}{\hbar}$ .

## 2.3 X-ray photoelectron diffraction

A theoretical description of the photoemission process is schematically illustrated in Fig. 2.4a. The absorbed photon produces a spherical, primary electron wave  $exp(ikr)/r$  centered at the emitting atom, with an angular distribution depending on the electron initial state and  $\vec{\epsilon}$ , the photon polarization vector. This primary electron wave is scattered by the neighboring atoms described by a spherically symmetric potential located at  $r_i, r_j, \dots$ . Each scattered wave of angular momentum  $l$  then undergoes a phaseshift  $\delta_l$  and the total scattering amplitude is given by the scattering factor  $f_j(\theta_j) = \frac{1}{k} \sum_l (2l+1) P_l(\cos\theta_j) e^{i\delta_l} \sin\delta_l$ , with  $l$  the angular momentum with respect to site  $j$ ,  $P_l$  the Legendre polynom and  $\theta_j$  the scattering angle. Atomic vibrations  $\langle u_j^2 \rangle$  are taken into account using a Debye-Waller factor and the electron wave amplitude attenuation due to inelastic processes during its propagation to the surface is determined by the inelastic mean free path  $\Lambda_e$ . The coherent superposition of direct( $\phi_o$ ), single( $\phi_i, \dots$ ) and multiple scattered waves( $\phi_j, \dots$ ) is then refracted at the surface potential step ( $V_o$ ). Depending on photoelectron kinetic energy and atom positions around the emitter, the coherent sum reveals an anisotropic behavior as a function of angle. The strong anisotropic distribution of photoelectrons emitted from crystalline materials has already been observed in 1970 by Siegbahn [4] on NaCl(001) crystal and is shown in Fig. 2.4b.

A schematic illustration of the photoelectron diffraction process is shown in Fig. 2.5a. For photoelectron kinetic energies higher than approximately 500eV, a clear anisotropic scattering amplitude is observed. As seen in Fig. 2.5b, the main scattering amplitude  $f(\theta)$  is found at  $\theta = 0^\circ$  and corresponds to the "forward focusing" direction. This enhancement is directly correlated to the emitter-scatterer direction, and one finds that the photoelectron angular direction is to first order approximation a forward projected picture of the atomic structure around the emitter. The Al scattering amplitude is calculated for different energies in Fig. 2.5b. In particular, it clearly shows that there is almost no backscattering ( $\theta = 180^\circ$ ) flux at 1000eV. Thus this behavior permits a very straightforward interpretation of XPD data.

In order to perform XPD, a precise control of the angular position of the sample is required together with an energy and angle resolving electron detection facility. The data presented in



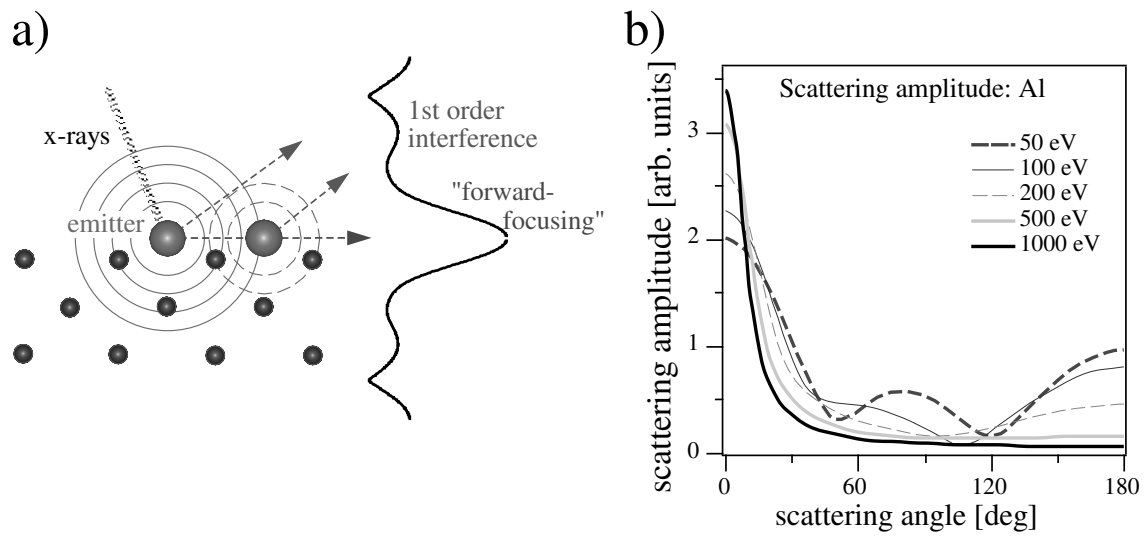


Figure 2.5: (a) Illustration of the forward focusing effect in the direction of the nearest-neighbors. (b) Calculations of plane waves scattering amplitudes for Al.

[4] K. Siegbahn, U. Gelius, H. Siegbahn and E. Olson, Phys. Lett. **A32**, 221 (1970).

# Chapter 3

## Multiple scattering calculations

### 3.1 Introduction

To obtain precise information about the structure of crystalline samples, simulations of the photoelectron diffraction process are essential. In many cases, a single scattering formalism, which considers only one scattering event on each atom of a given cluster, is sufficient to calculate diffraction patterns, e.g. for the orientation of adsorbed molecules [1], or to optimize atom positions of submonolayer coverages of adatoms via a R-factor analysis [2]. Moreover, this approach has the advantage to be much less computing time consuming, permitting to consider larger clusters than with the multiple scattering formalism. However, as will be shown in this thesis, this approach is not accurate enough for surface termination determination of quasi-two-dimensional systems (see Section 3.4), for which the multiple scattering approach becomes essential.

This chapter is organized as follows: Section 3.2 introduces some calculation parameters and their influence on calculations. A description of the optimization process for the well-known Cu(111) surface is also presented. Then a comparison between single and multiple scattering is done in Section 3.3. And finally the Section 3.4 describes how it is possible to determine the crystal surface termination using the MSC approach, and what are the possible limitations of such studies depending on the type of scatterer, the atomic distance or the stacking sequence. This chapter has been arranged for two different kind of readers. The reader interested in understanding the MSC but without performing calculations can skip the footnote where the "EDAC command" are briefly explained. However, the reader who would like to perform calculations with the EDAC code can use the footnote as a user guide together with the EDAC manual available in Ref. [3].

## 3.2 EDAC: General remarks

### 3.2.1 Introduction

The EDAC (electron diffraction in atomic clusters) code [4] adopts a cluster approach. The cluster shape (spherical<sup>a</sup> or parabolic<sup>b</sup>) and size ( $\propto R_{max}$ <sup>c</sup>) define the number of atoms surrounding the emitter, as seen in Fig. 3.1. The excitation process defined by the photon polarization vector<sup>d</sup> creates an initial spherical photoelectron wave which is scattered by the surrounding atoms. This code takes into account the attenuation of the wave amplitude during its propagation in the solid<sup>e</sup>, the atomic thermal vibrations<sup>f</sup> and the refraction at the surface potential step<sup>g</sup>. The coherent superposition of the initial photoelectron wave and the scattered waves defines the final amplitude<sup>h</sup> measured by the detector<sup>i</sup> at a given angle<sup>j</sup>.

The calculations are performed using an exact representation of the Green function propagator, meaning that no further approximation has to be done except for the muffin-tin approximation<sup>k</sup>. The muffin-tin model implies that a spherical atomic potential of a given atom vanishes further than  $r_{mt}$ . The  $r_{mt}$  can be estimated via the average nearest-neighbour distance. The calculation time is proportional to  $nN^2(l_{max} + 1)^3$ , where  $n$  is the scattering order,  $N$  the number of atoms used in the cluster and  $l_{max}$  the value of the maximum angular momentum in the multipole expansion of the wave function around each atomic center of scattering.

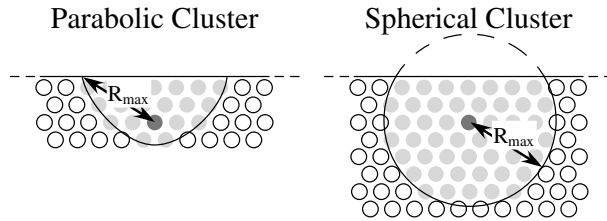


Figure 3.1: Cluster shapes as a function of the  $R_{max}$ . The light and gray disks correspond to scatterers and to the emitter, respectively.

<sup>a</sup>EDAC command: *cluster surface off*

<sup>b</sup>EDAC command: *cluster surface on*

<sup>c</sup>EDAC command: *cluster Rmax l(A)  $\alpha$* , where  $\alpha$  is the maximum distance in Å from the emitter up to which atoms are considered to belong to the cluster.

<sup>d</sup>EDAC command: *polarization LPx/LPy/LCP/RCP*

<sup>e</sup>EDAC command: for one simple inelastic mean free path: *imfp inline 1 l(A)  $\alpha$* , where  $\alpha$  is the suitable value

<sup>f</sup>EDAC command: *Debye-temperature i  $\theta_D$*  to select independant  $\theta_D$  in Kelvin for each atom type  $i$

<sup>g</sup>EDAC command: *V0 E(eV)  $\alpha$* , where  $\alpha$  is the energy value of the vacuum level in eV.

<sup>h</sup>EDAC command: *scan pd OutputName*

<sup>i</sup>EDAC command: *emission angle window  $\alpha$* , where  $\alpha$  is the half-width angle of the acceptance cone

<sup>j</sup>EDAC commands: *emission angle phi  $\phi_i \phi_f n_{step}$*  and *emission angle theta  $\theta_i \theta_f n_{step}$*

<sup>k</sup>EDAC command: *muffin-tin*

### 3.2.2 Calculation procedure coupled with the reliability factor

A good starting point of an atomic structure optimization in EDAC begins by another parameter setting optimization. Indeed, the calculated diffraction patterns can strongly depend on the initial value of parameters such as  $R_{max}$ ,  $l_{max}$ ,  $d_{max}$  (the maximum distance between two successive scattering events taking place at cluster atom positions)<sup>1</sup>, Debye temperature, inelastic mean free path, etc... To analyze the effect of these parameters on EDAC simulations, and at the same time to suggest how to use EDAC to obtain better agreement between measured and calculated diffractograms, we propose an R-factor [5] based self-consistent optimization procedure, here applied on the well-known Cu(111) surface.

Indeed, to obtain a quantitative value of the agreement between calculated and measured diffractograms, an R-factor analysis based on the multipole expansion of the angular intensity distribution, *i.e.*, the expansion into spherical harmonics, has been used. In short, the multipole coefficients  $a_{lm}$  for the experimental and the calculated diffraction patterns  $I(\theta, \phi)$  are obtained by

$$a_{lm} = \frac{1}{4\pi} \int \chi(\theta, \phi) Y_{lm}^*(\theta, \phi) d\Omega, \quad (3.1)$$

where  $Y_{lm}^*$  are the complex conjugates of the spherical harmonics, and  $\chi(\theta, \phi)$  is the oscillatory part of the diffraction pattern obtained by normalization with respect to the average intensity  $I_0(\theta)$  for each polar angle  $\theta$ :

$$\chi(\theta, \phi) = \frac{I(\theta, \phi) - I_0(\theta)}{I_0(\theta)}. \quad (3.2)$$

The R-factor is then obtained by summing the distance between the points in the complex plane representing the experimental and theoretical multipole coefficients  $a_{lm}$  over all  $l$  and  $m$ 's considered [5]:

$$R - factor = \sum_{l=0}^{l_{max}} \sum_{m=-l}^l | a_{lm}^{th} - a_{lm}^{exp} |. \quad (3.3)$$

Thus, based on various observations related to the variation of R-factors between one given experimental result and different MSC calculations, it is possible to establish a procedure to optimize non-structural and structural parameters.

First of all, the non-structural parameters which strongly influence MSC patterns, and of course R-factors, (as  $R_{max}$  or  $l_{max}$ ) are optimized, followed by the non-structural parameters which have less impact on calculated diffractograms, such as Debye temperatures or inelastic mean free paths.<sup>m</sup>

<sup>1</sup>EDAC command:  $dmax\ l(A)\ \alpha$ , where  $\alpha$  is the  $d_{max}$  value in  $\text{\AA}$ . As default, this value is fixed to infinity.

<sup>m</sup>Note that this rule can suffer from exceptions. Indeed, if a non-realistic value for one of these parameters is given (for the inelastic mean free path or the scattering order for instance), abnormal high R-factors corresponding to completely wrong calculated MSC patterns can be obtained.

In Fig. 3.2a-e, we show different  $R_{max}$  vs  $l_{max}$  R-factor grids showing the influence of  $d_{max}$ ,  $imfp$ , Debye temperature and the number of emitters. Fig. 3.2f shows the R-factor variation as a function of  $d_{max}$ , for 9 emitters,  $R_{max}=19\text{\AA}$  and  $l_{max}=8$ .

For a given cluster shape, the number of atoms taken into account is a function of the number of emitters and is defined by the  $R_{max}$  value. For the above example, the number of atoms is, for 9 emitters, 30, 114, 219 and 336 atoms for  $R_{max}= 19, 20, 21, 22 \text{\AA}$  respectively and for 6 emitters, 71, 107, 167 and 224 atoms for  $R_{max}= 14, 15, 16$  and  $17\text{\AA}$  respectively<sup>n</sup>.

Contrary to what could be expected, the R-factor does not necessary decrease with an increasing  $R_{max}$ . This is counterintuitive as with a larger  $R_{max}$  the number of atoms in the cluster increases and should therefore lead to a MSC calculation more similar to the real experiment. However, this counterintuitive phenomenon could be seen as an advantage because the calculation time is related to the number of atoms.

In Fig. 3.2, R-factors are always smaller for small  $l_{max}$  value. This behavior is specific to this measurement and not observed on other systems. As seen in Appendix Fig. B.2, B.1 and B.3 the  $l_{max}$ , which approximates the outgoing photoelectron wave function using a combination of  $l_{max}^o$  spherical harmonics, can strongly affect MSC calculations. Note that its value is estimated by  $l_{max} \approx kr_{mt}$  where  $k$  is the photoelectron wave vector ( $\propto \sqrt{E_{kin}}$ <sup>p</sup>). However, surprisingly the  $l_{max}$  corresponding to the smaller R-factor value does not in every case scale with the photoelectron kinetic energy, contrary to the  $l_{max} \approx kr_{mt}$  approximation. For example, as seen in Section 3.3, optimal values for  $l_{max}$  of 13 and 8 are obtained for the two different  $E_{kin}=320.8 \text{ eV}$  and  $E_{kin} = 807.2 \text{ eV}$  (corresponding to the excitation of Cu  $2p_{3/2}$  line by MgK $\alpha$  and SiK $\alpha$  radiation respectively). This unexpected behavior is not problematic as the important point is to calculate with a large enough  $l_{max}$  to obtain the best approximation of the outgoing photoelectron wave function using a combination of  $l_{max}$  spherical harmonics.

As can be seen in Fig. 3.2a-c, the R-factors obtained for different  $d_{max}$  (10, 15 and  $20\text{\AA}$ ) values are similar and the minimal R-factor values are obtained for the same set of parameters. Note that  $d_{max}$  is the only parameter which has been changed between the three graphs. This behavior is helpful for minimizing the calculation time. Indeed, the calculation time increases with an increasing  $d_{max}$  (with a 3.2Ghz processor, order=8 for  $d_{max}=10\text{\AA} \approx 1h20$  and for  $d_{max}=20\text{\AA} \approx 4h$ ).

Between Fig. 3.2c and e, the only differences in the initial calculation parameter setting are the  $d_{max}$  ( $20\text{\AA}$  and "unlimited" respectively) and the number of emitters (9 and 6 emitters). Two informations can be obtained by studying these two figures. First, when a sufficiently large number of emitters is selected (here 6), the minimal R-factor value is located at the same position (same  $R_{max}$  and  $l_{max}$  values) than for a larger number of emitters, indicating that very deep emitters do not strongly affect the MSC calculation (which is also naturally the case in experiment). Second, the use of a limited  $d_{max}$  (9 emitter case) does not affect the diffraction

---

<sup>n</sup>Trick to determine a useful range for  $R_{max}$  values: try to first calculate with different  $R_{max}$  values using degenerated (=1)  $l_{max}$  and recursion order. It permits to check the cluster (EDAC command: *cluster output l(A) ClusterName*) and the number of considered atoms for each  $R_{max}$  (EDAC command: *report natoms*) with a short calculation time.

<sup>o</sup>EDAC command: *lmax*  $\alpha$ , where  $\alpha$  is the  $l_{max}$  value

<sup>p</sup>EDAC command: *emission energy E(eV) E<sub>i</sub> E<sub>f</sub> n<sub>step</sub>*

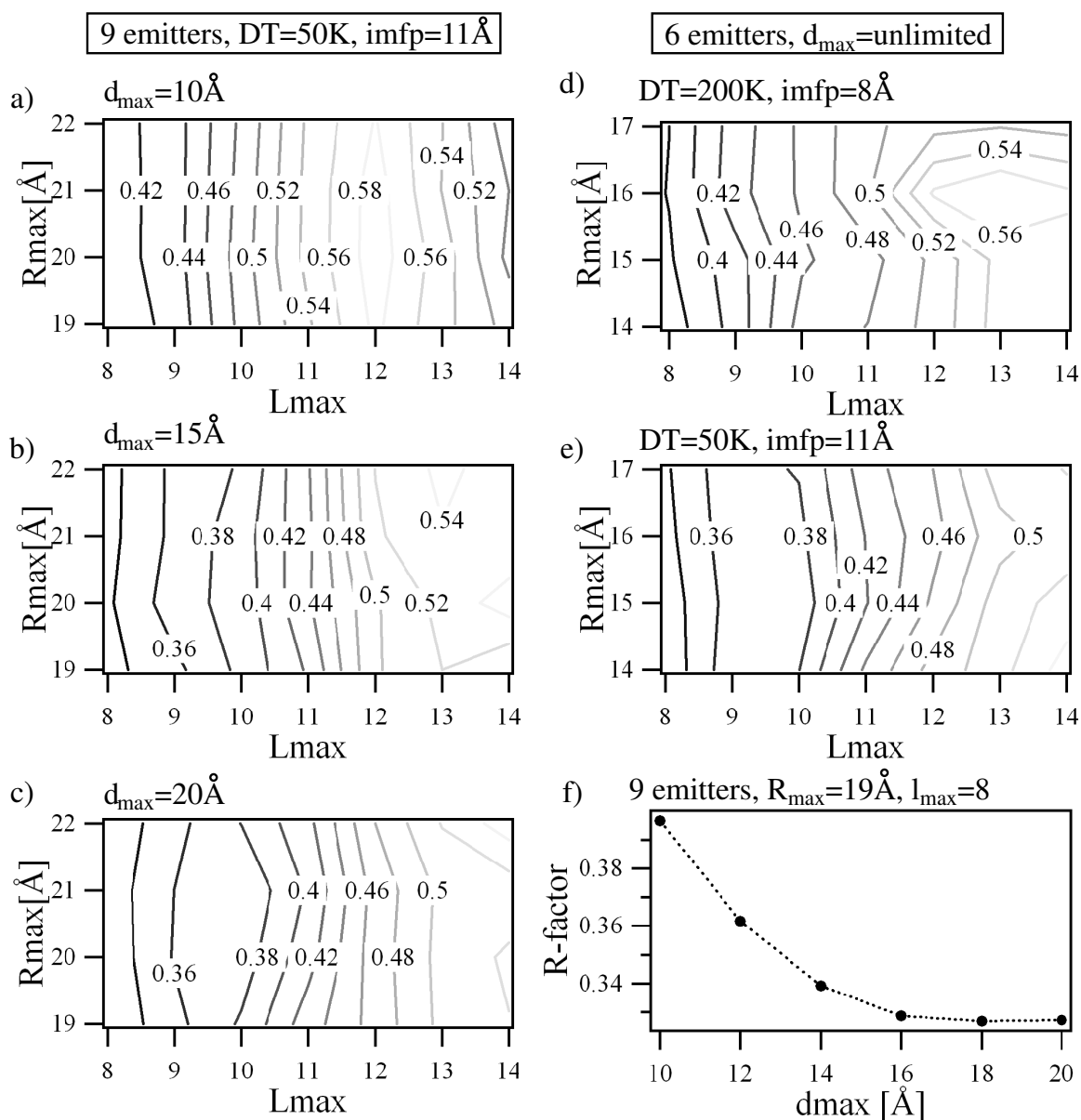


Figure 3.2: (a)-(e)  $R_{max}$  vs  $l_{max}$  R-factor grids for various parameters. Fig. 3.2f shows the R-factor variation as a function of  $d_{max}$ , for 9 emitters,  $R_{max}=19\text{\AA}$  and  $l_{max}=8$ .

pattern if it is large enough.

Note that it is very important to use the smallest number of emitters (for which the MSC pattern is "good") to perform a complete optimisation procedure. Indeed, it can strongly reduce the calculation time even if the number of atoms becomes larger. For instance, as shown in Table 3.1, the calculation performed for 6 emitters ( $R_{max}=14\text{\AA}$  and 71 atoms) runs during  $\approx 1\text{h}$  while for 9 emitters and a similar diffraction pattern and R-factor value, the calculation runs during more than  $\approx 4\text{h}$  even with less atoms ( $R_{max}=19\text{\AA}$  and 30 atoms) and a limited  $d_{max}=20\text{\AA}$ . Obviously in this last case, the calculation time can be reduced by decreasing the  $d_{max}$  (for

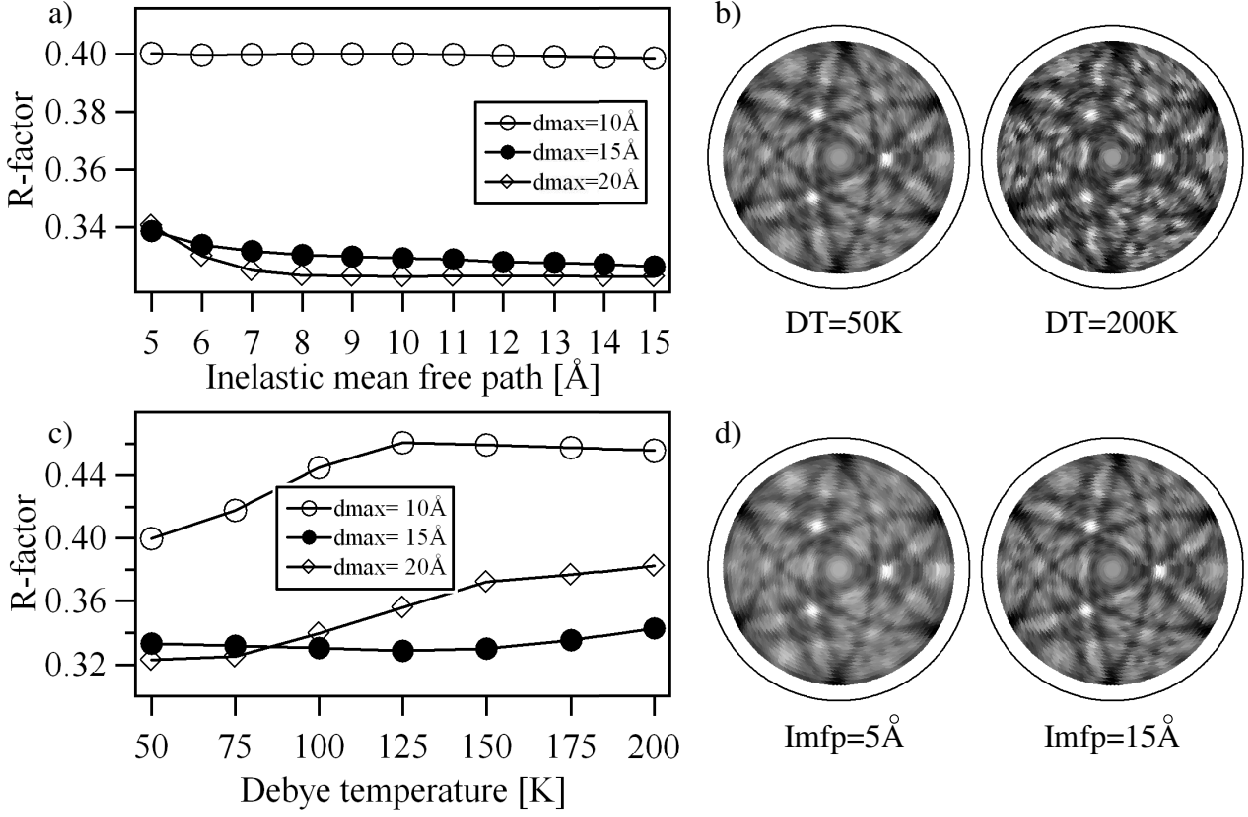


Figure 3.3: (a) R-factor as a function of the Debye temperature for different  $d_{max}$  values and (b) two MSC calculations corresponding to two different Debye temperatures for  $d_{max}=20\text{Å}$ . (c) R-factor as a function of the imfp for different  $d_{max}$  values and (d) two MSC calculations corresponding to two different imfp for  $d_{max}=20\text{Å}$ .

Numbers of emitters	$R_{max}$ [Å]	Number of atoms	$d_{max}$ [Å]	Calc. time
6	14	71	$\infty$	$\approx 1\text{h}$
9	19	30	20	$\approx 4\text{h}$
9	19	30	10	$\approx 1\text{h}20$

Table 3.1: Calculation time as a function of various parameters. Calculations performed with a 3.2Ghz processor.

$d_{max}=10\text{\AA} \approx 1h20$ ), but here at the detriment of the R-factor value as seen in Fig. 3.2f.

The R-factor evolution as a function of the Debye temperature is shown in Fig. 3.3a for different  $d_{max}$  values. Here only the 9 emitters case is studied as it is very similar to the 6 emitters case for  $d_{max}=20\text{\AA}$ , and also because the modification of  $d_{max}$  can strongly affect MSC calculation patterns which is a good way (only one parameter to change) to observe the impact of the Debye temperature on lower accuracy MSC calculations. As shown in Fig. 3.3a, the R-factor becomes worse for larger Debye temperatures, and this whatsoever the  $d_{max}$  value. This effect, not strong for  $d_{max}=15\text{\AA}$  in this example, is a permanent feature in the different studies performed during this thesis. The R-factor is always better for Debye temperatures smaller than those found in the litterature. This behavior suggests that features obtained in MSC calculations performed with "conventional" Debye temperatures are too sharp comparing to features displayed in experimental diffraction pattern. This is shown in Fig. 3.3b for two MSC calculations performed with two Debye temperatures for  $d_{max}=20\text{\AA}$ .

As for Debye temperatures,  $imfp$  can be seen as a "smoothing" parameter. The R-factor variation as a function of  $imfp$  is shown in Fig. 3.3c. First of all, the R-factor is only feebly affected by the  $imfp$  increase. But this small variation becomes larger for larger  $d_{max}$  (better R-factor). It thus suggests that for poor agreement between the MSC calculation and the experiment ( $d_{max}=10\text{\AA}$ ), the effect of the  $imfp$  is smaller than for more adequate MSC calculations ( $d_{max}=20\text{\AA}$ ). The effect of the  $imfp$  on MSC calculations is shown in Fig. 3.3d, where calculations for  $imfp=5$  and  $15\text{\AA}$  are displayed. It shows how a smaller  $imfp$  can slightly smooth the diffraction patterns.

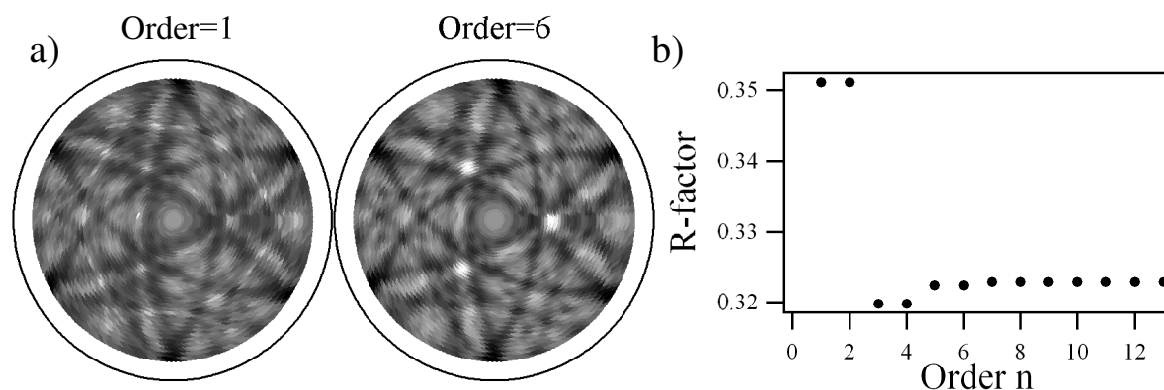


Figure 3.4: (a) Calculated diffraction patterns for two different recursion orders. (b) R-factor vs recursion order plot.

Obviously, the order of recursion plays an important role regarding to the accuracy of the result. But the choice of a large enough value is, as first approximation, quite easy to do as reflected in Fig. 3.4a which shows how the whole MSC calculation changes as a function of the recursion order for the Cu(111)  $2p_{3/2}$  emission case. Moreover, in some cases (not shown here),

if a too small order is chosen, singularities can appear in MSC diffraction patterns<sup>9</sup>. If such singularities are obtained, the recursion order value can be increased until their disappearance. As the calculation time increases linearly with the recursion order, a particular attention to this parameter has to be given. In the EDAC code, two kinds of iteration procedure can be utilized. For the *direct Jacobi iteration* method (by default), each iteration corresponds directly to an order of scattering while in the *modified recursion method*<sup>†</sup>, the result obtained from one iteration is mixed with the previous result to improve the convergence. In the latter case, the convergence is also faster, as explained in Ref. [4].

Finally, to perform an atomic structure optimization related to an experimental XPD, we can proceed following the way described in Fig. 3.5. First, based on physical considerations, known bulk structure or literature, an initial structural model is guessed. The number of emitters,  $N_e$ , could be selected in such a way that the depth of the deeper emitter is  $\approx 1.5$  imfp. The other parameters are determined using the above explanation (and with horse sense). The experimental diffraction pattern is then simulated and compared to the measured result. By modifying alternatively the above-discussed non-structural parameters ( $R_{max}$ ,  $l_{max}$ , Debye temperature,  $d_{max}$ , recursion order, imfp) and the number of emitters, a minimal value is obtained for the R-factor.

Second, when a reasonably low R-factor value is obtained (using a given setting of non-structural parameters), various structural parameters can be varied until the best agreement with experiment as judged by the R-factor. The new optimized positions can define a new cluster which can be used as initial parameter of the first R-factor analysis loop. This procedure can be repeated until the final lowest R-factor (or the non-structural and structure parameters) does not vary anymore.

## References for section 3.2

- [1] R. Fasel, P. Aebi, R. G. Agostino, D. Naumović, J. Osterwalder, A. Santaniello, L. Schlapbach, Orientation of adsorbed C<sub>60</sub> molecules determined via x-ray photoelectron diffraction, *Phys. Rev. Lett.* **76** (25) (1996) 4733–4736.
- [2] R. Fasel, P. Aebi, J. Osterwalder, L. Schlapbach, R. G. Agostino, G. Chiarello, Local structure of c(2×2)-Na on Al(001):Experimental evidence for the coexistence of intermixing and on-surface adsorption, *Phys. Rev. B* **50** (19) (1994) 14516–14524.
- [3] <http://csic.sw.edu.es/jga/software/edac/manual/edac.html>
- [4] F. J. Garcia de Abajo, M. A. Van Hove, C. S. Fadley, Multiple scattering of electrons in solids and molecules: A cluster-model approach, *Phys. Rev. B* **63** (2001) 075404–1–16.
- [5] R. Fasel, Adsorbed monolayers and submonolayers studied by angle-scanned photoemission, Ph.D. thesis, University of Fribourg (1996).

---

<sup>9</sup>Note that a small number of singularities does not drastically affect the R-factor value.

<sup>†</sup>EDAC command: *iteration recursion*

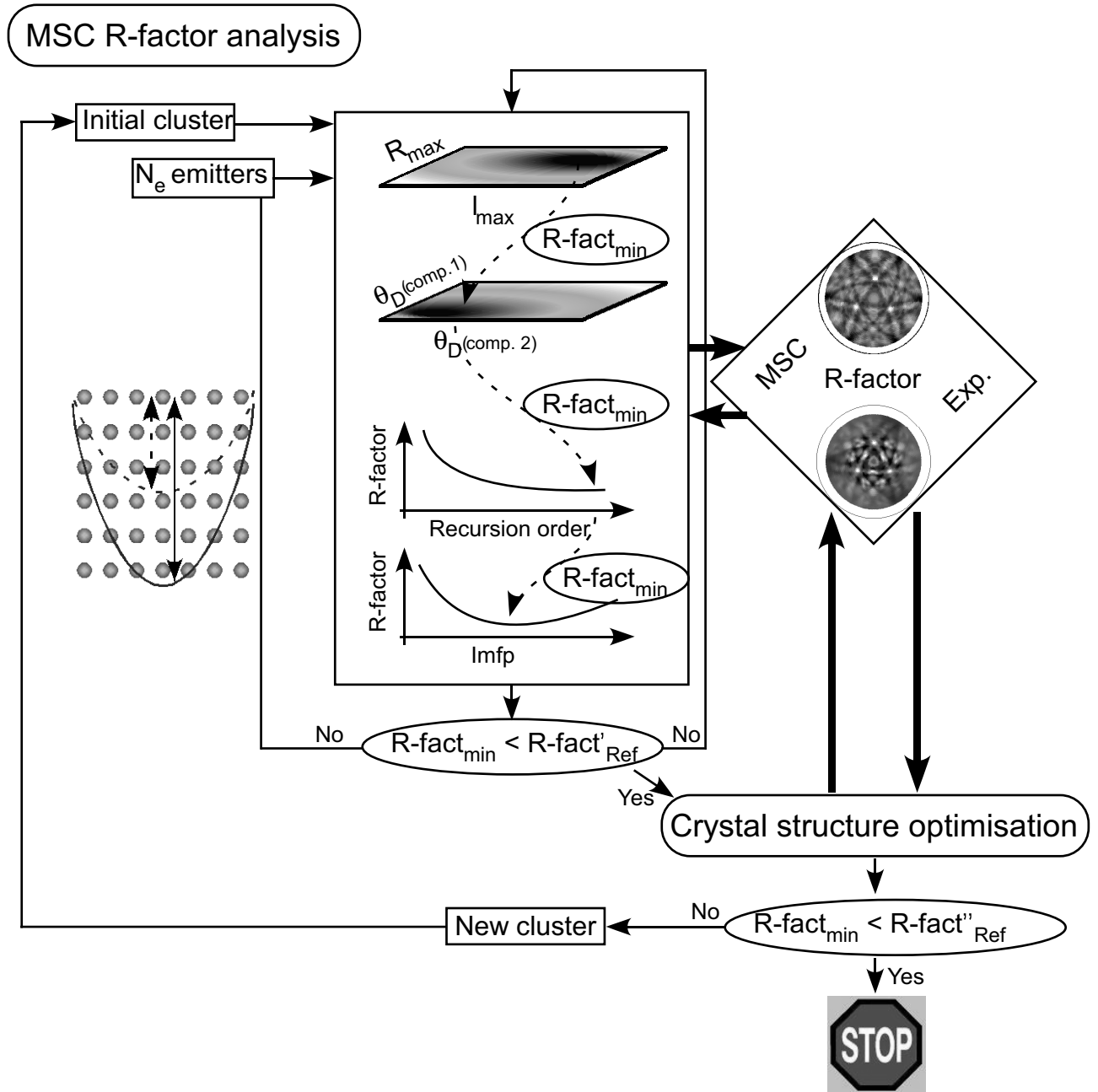


Figure 3.5: Illustration of the trial-and-error scheme for calculation parameter determination and crystal structure refinement in XPD using the EDAC code and a R-factor analysis.



### 3.3 X-ray photoelectron diffraction study of Cu(111): Multiple scattering investigation

L. Despont,<sup>1</sup> D. Naumović,<sup>2</sup> F. Clerc,<sup>1</sup> C. Koitzsch,<sup>1</sup> M. G. Garnier,<sup>1</sup> F. J. Garcia de Abajo,<sup>3</sup>,  
M. A. Van Hove,<sup>4</sup> P. Aebi,<sup>1</sup>

<sup>1</sup> *Institut de Physique, Université de Neuchâtel, Rue A.-L. Breguet 1, CH-2000 Neuchâtel, Switzerland*

<sup>2</sup> *Institut de Physique, Université de Fribourg, Pérolles, CH-1700 Fribourg, Switzerland*

<sup>3</sup> *Centro Mixto CSIC-UPV/EHU, 20080 San Sebastián, Spain*

<sup>4</sup> *Materials Sciences Division and Advanced Light Source, Lawrence Berkeley National Laboratory, Berkeley, CA 94720, and Department of Physics, University of California, Davis, CA 95616.*

Published in Surf. Sci. **600**, 380-385 (2006)

Multiple scattering theory based on a cluster model is used to simulate full hemispherical x-ray photoelectron diffraction measurements in order to verify how state of the art multiple scattering simulations are able to reproduce the experiment. This approach is applied to the Cu(111) surface for two different photoelectron kinetic energies. Differences and similarities between single and multiple scattering are discussed in comparison with experimental results. We find that the present approach gives very good results despite some limitations.

#### 3.3.1 Introduction

The complete knowledge of the atom positions is a necessary prerequisite for the understanding of the various properties of material's surfaces. Among the numerous techniques available to the scientist to obtain this crystalline information, x-ray photoelectron diffraction (XPD) has proven to be very powerful, owing to its chemical sensitivity and its ability to measure sub-angstrom atomic displacements. However without theoretical simulations it is often difficult to understand the different structures appearing in XPD data and to link them to true crystalline positions. Single scattering codes are used for some time now to simulate diffractograms and are sufficient to calculate the major crystalline structure, the orientation of adsorbed molecules [1], or to optimize atom positions of submonolayer coverages of adatoms via a R-factor analysis [2]. However, this approach appears insufficient for multilayer systems like in ferroelectric films or for surface termination determination of quasi-two-dimensionnal systems [3], for which the multiple scattering approach becomes essential.

Recently, thanks to the development of new computer codes and the availability of faster computers, it has become possible to simulate XPD diffractograms using a MSC formalism (see Ref. [4] and references therein). It is the aim of this paper to perform an as complete as possible comparison of Cu(111) surface XPD measurements with the MSC simulations using the EDAC (Electron Diffraction in Atomic Clusters) computer code [4]. Therefore, this study serves to verify to what degree state of the art EDAC multiple scattering simulations are able to reproduce full hemispherical XPD patterns.

### 3.3.2 Experimental and Computational Details

The XPD measurements are performed in a modified Vacuum Generators ESCALAB Mark II X-ray photoelectron spectrometer equipped with a fixed hemispherical electron energy analyzer, and a three channeltron detection system, operated with a base pressure in the lower  $10^{-11}$  mbar region. The x-ray tube contains a  $\text{MgK}\alpha$  ( $h\nu=1253.6$  eV) and  $\text{SiK}\alpha$  ( $h\nu=1740$  eV) twin anode. The samples are fixed on a computer-controlled two-axis goniometer capable of scanning the emission angle over the full hemisphere above the surface [5–10]. Data has been collected for a polar angle range  $\theta \in [0^\circ, 78^\circ]$  and an azimuthal angle range  $\phi \in [0^\circ, 360^\circ]$ .

For electron kinetic energies higher than approximately 500 eV the analysis of diffraction patterns is made easier by the so-called "forward focusing" effect which consists in an enhancement of the emission intensity along densely packed atomic planes and rows of atoms (corresponding to low-index crystallographic directions) [11]. In the above-mentioned energy range, the photoelectron inelastic mean free path ( $\lambda$ ) is large and thus the number of scattering events can be also large. The scattering on the first few atoms has a tendency to focus the emission in the emitter-scatterer direction while on the subsequent atoms it tends to defocus the signal [12]. It is a clear indication for the necessity to use MSC in order to get precise information on the intensity and shape of the "forward focusing" peaks. Furthermore, the defocusing is also linked to the development of the conventional Kikuchi bands which become more intense when the forward-scattering peak intensity diminishes [12]. Thus MSC is also required to reproduce Kikuchi band intensities as well as diffraction pattern structure details. Single scattering (SSC) is well-known to overemphasize the intensity of the "forward focusing" peaks [11].

The cluster model approach of the EDAC code [4] used here to simulate the XPD experiment is based on the muffin-tin potential approximation [13]. EDAC evaluates the MSC expansion using a fully convergent recursion method. In order to overcome the rapidly-growing computational demand, EDAC contains the Rehr and Albers [14] procedure consisting in a separable representation of the free-electron Green function. The Haydock recursion method is used to calculate an iterative solution of the MSC series. The computation time needed to determine the scattered wave function is proportional to  $nN^2(l_{max}+1)^3$ , where  $n$  is the scattering order,  $N$  the number of atoms used in the cluster and  $l_{max}$  the maximum angular momentum quantum number. This last parameter permits an approximation of the outgoing photoelectron wave function using a combination of  $l_{max}$  spherical harmonics. The number of spherical harmonics is approximately given by  $l_{max} \approx kr_{mt}$  [13] where  $k$  is the photoelectron wave vector and  $r_{mt}$  the muffin-tin radius. By estimating an average nearest-neighbour distance and selecting a photoelectron kinetic energy  $E_{kin}$ , the  $l_{max}$  parameter can roughly be deduced.

The number  $N$  of scattering atoms in the cluster is defined with the parameter  $R_{max}$ . Figure 3.6 shows how  $R_{max}$  defines the scattering volume using the emitter either as the focus of a parabola or as a sphere center. The following  $R_{max}$  values are chosen:  $R_{max}=22$  Å for  $E_{kin}=807.2$  eV (Cu  $2p_{3/2}$  core level excited with  $\text{SiK}\alpha$ ) and  $R_{max}=13$  Å for  $E_{kin}=320.8$  eV (Cu  $2p_{3/2}$  core level excited with  $\text{MgK}\alpha$ ). To increase the contribution of scattering of the atoms located between the emitters and the surface, the parabolic shape is selected in the present study, which gives a scattering volume containing approximately 300 atoms for the high energy case and 100 atoms for the low energy one. The electron inelastic mean free path  $\lambda$  can be

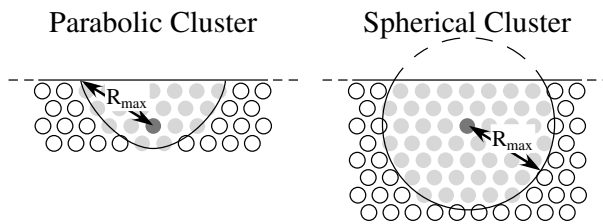


Figure 3.6: Cluster shapes as a function of  $R_{max}$ . The light and dark gray disks correspond to scatterers and to the emitter, respectively.

deduced from the universal relationship between kinetic energy and inelastic mean free path, given by [15, 16]:

$$\lambda(\text{\AA}) = \frac{538 \cdot d}{E_{kin}^2(eV)} + 0.13 \cdot \sqrt{d^3 \cdot E_{kin}(eV)}, \quad (3.4)$$

where  $d$  is the Cu(111) interlayer spacing ( $d = 3.6149 \cdot \frac{1}{\sqrt{3}} \text{\AA}$ ). In the case of photoelectrons with  $E_{kin}=807.2 \text{ eV}$ ,  $\lambda \approx 11 \text{\AA}$ , nine emitters distributed down to  $-16.7 \text{\AA}$  below the surface are chosen. At lower photoelectron kinetic energy,  $E_{kin}=320.8 \text{ eV}$  with  $\lambda \approx 7 \text{\AA}$  five emitters distributed over five layers are chosen down to  $-8.3 \text{\AA}$ . The introduction of an inner potential  $V_o$  permits to consider the refraction of the photoelectron wave at the surface-potential step. For Cu,  $V_o=13.5 \text{ eV}$  is taken [13]. The calculations were performed for a temperature  $T=300 \text{ K}$  and thermal vibrations are introduced by means of a reasonable non-zero Debye temperature  $\theta_D$ . Best agreement between experiment and MSC theory is obtained by optimizing  $l_{max}$ ,  $R_{max}$ ,  $\theta_D$ ,  $n$  and the number of emitters.

To obtain a quantitative value of the agreement between calculated and measured diffractograms, an R-factor analysis based on the multipole expansion of the angular intensity distribution, *i.e.*, the expansion into spherical harmonics, has been used. The R-factor calculation method is detailed in Ref. [2].

### 3.3.3 Results and Discussion

The calculated and measured diffractograms of Cu(111)  $2p_{3/2}$  measured with  $\text{SiK}\alpha$  ( $E_{kin} = 807.2 \text{ eV}$ ) are presented in Fig. 3.7, using the same linear gray scale and stereographic projection. Experimental diffractograms are acquired simultaneously at two different kinetic energies: one exactly at the center of the  $2p_{3/2}$  photoemission line ( $E_{kin} = 807.2 \text{ eV}$  in this case) and one slightly above ( $E_{kin} = 812.2 \text{ eV}$ ) to monitor the background intensity variation. The subtraction of the second from the first diffractogram, taking into account the channeltron sensitivities, allows to get rid of the inelastic electron background. Taking advantage of the threefold symmetry of the Cu(111) the measured diffractograms are azimuthally averaged. In order to facilitate the comparison with the calculation, a smooth polar angle dependent background is subtracted from both the measured and the calculated diffractograms. This polar angle dependent background originates from three different effects. First, the analyzed surface area changes with  $1/\cos(\theta)$  by scanning the polar angle ( $\theta$ ) from normal emission ( $\theta=0^\circ$ ) to grazing

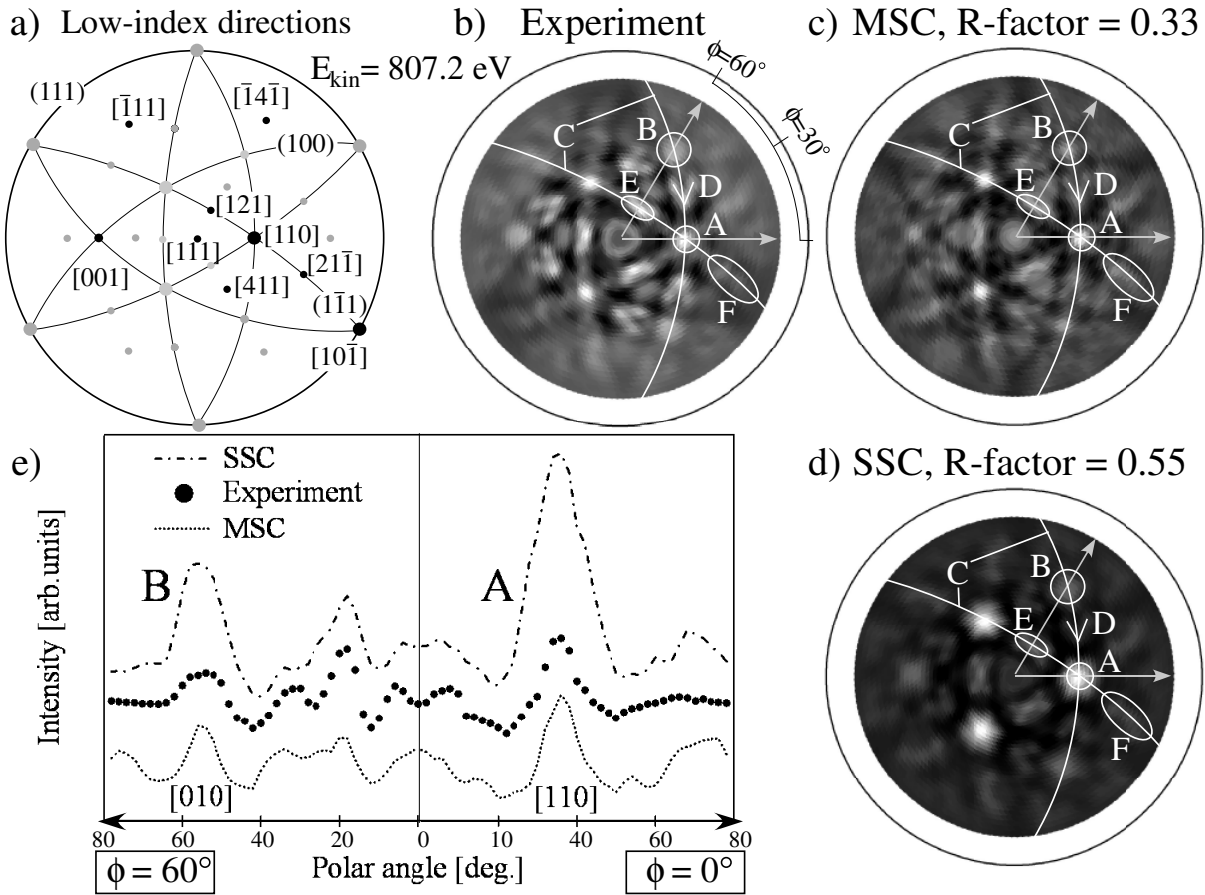


Figure 3.7: Stereographic projections for Cu(111). (a) The projections of some low-index crystal planes (lines) and the major directions (dots) are drawn in order to facilitate the discussion. The labeled low-index directions are indicated by black dots. Stereographic projections of (b) measured and (c), (d) multiple and single scattering simulated diffractograms for Cu  $2p_{3/2}$  at 807.2 eV. (SiK $\alpha$ ,  $h\nu=1740$  eV). (e) Polar scans at  $\phi = 60^\circ$  and  $0^\circ$ . The experimental profiles are represented by black dots. Polar scans are normalized with respect to their mean intensity and offset with respect to each other.

emission ( $\theta = 78^\circ$ , here). Secondly, due to the refraction at the surface (linked to the inner potential), the photoelectron intensity is anisotropically reduced with larger polar angles. And finally, the photoelectron intensity depends on the photoelectron escape depth, which is a function of the polar angle. The removal of a polar angle dependent background therefore permits to obtain a diffractogram independent of these aspects, emphasizing the features due to interference.

Figure 3.7a shows the stereographic projection of the low-index crystal planes and directions. In all the theoretical and experimental data, see Fig. 3.7b, c and d, the "forward focusing" peaks along  $\langle 110 \rangle$  directions are dominant (label "A" in Fig. 3.7b, c and d), and those along the  $\langle 001 \rangle$  directions are less intense (B). The shapes and widths of these two features are better reproduced by the MSC calculation than by the SSC, as can be seen in Fig. 3.7e. Kikuchi bands representing  $\{100\}$  and  $\{111\}$  type planes (C) are present in MSC with a width

and intensity comparable to the experiment while they appear broader in SSC. The same V-like structure (D) is observed in all diffractograms on the  $\{100\}$  Kikuchi bands between the dominant  $\langle 110 \rangle$  peaks and the  $\langle 001 \rangle$  directions. Again, this experimental V-like feature is better reproduced by the MSC code. Interferences of two neighbouring  $\langle 110 \rangle$  directions generate modulations along the  $1\bar{1}1$  planes with maxima near  $[121]$  (E) [6]. Similar features (F) appear in the  $[21\bar{1}]$  direction along the same planes, produced by interferences of the scattering by  $[110]$  and invisible  $[10\bar{1}]$  neighbours. The E and F modulations are roughly the same for the experiment, MSC and SSC simulations. So far MSC has given very good results. However, the experimental diffractogram on Fig. 3.7b exhibits a doughnut-like feature in the center which is not reproduced in the calculation. In fact, SSC gives a better agreement (see Fig. 3.7e at  $0^\circ$ ). By changing  $l_{max}$ , the number of spherical harmonics taken into account, this feature can be reproduced in the MSC simulation but at the expense of disagreement in other diffractogram structures, leading to an increase of the below-discussed R-factor. This points to a possible instability with respect to the  $l_{max}$  convergence.

In order to give a more quantitative comparison between measurement and calculations, and especially between MSC and SSC, two polar cuts at  $\phi = 60^\circ$  and  $0^\circ$  are displayed (Fig. 3.7e), for the measured and calculated Cu  $2p_{3/2}$  diffractograms. All polar cuts are normalized with respect to their mean intensity and offset with respect to each other. The most striking difference between the two calculations lies in the "forward focusing" peaks, (label A and B), whose intensities is much better reproduced by MSC calculation. As already mentioned, this overemphasizing of the "forward focusing" peaks is a well-known shortcoming of SSC. What is visible locally in the interference patterns is confirmed by a global match approach which uses the reliability R-factor to judge the quality of the fit between the complete experimental interference pattern data and theory. The much smaller value for MSC,  $R\text{-factor} \approx 0.33$ , than for SSC,  $R\text{-factor} \approx 0.55$ , confirms the better global agreement obtained with MSC [17] and confirms what has been obtained by eye. Note that the better agreement is not only due to the overemphasized "forward focusing" peaks with the SSC approach but also due to better agreement with the small structures comparing the MSC and the experimental result. This has been checked by artificially putting the intensities in the "forward focusing" areas to a common mean value. The idea is to remove the contribution of the overemphasized "forward focusing" peaks in the SSC to the R-factor. The obtained R-factor for the SSC approach is still worse than for MSC, indicating that the "forward focusing" peaks are not the only reason of the better agreement between the experiment and MSC.

This conclusion is corroborated with the result of the following analysis using a smaller photoelectron energy. In fact, the same  $2p_{3/2}$  photoelectron line is selected, but excited with  $MgK\alpha$  radiation ( $h\nu = 1253.6$  eV), changing the photoelectron kinetic energy to 320.8 eV. MSC effects are damped owing to the shorter inelastic mean free path  $\lambda$ , which still corresponds to 2-3 atomic distances. In this case, the SSC model should perform better than at high photoelectron kinetic energy.

The same procedure in terms of data treatment as for the high kinetic energy has been used in order to facilitate the comparison between both energies. In Fig. 3.8, the intensity enhancements along  $\langle 110 \rangle$  directions are still dominant (label A'), as in the true "forward focusing" regime at high kinetic energies. These peaks correspond to scattering on nearest neighbour atoms. Nevertheless, the signal is broader at lower kinetic energy, because the photoelectron

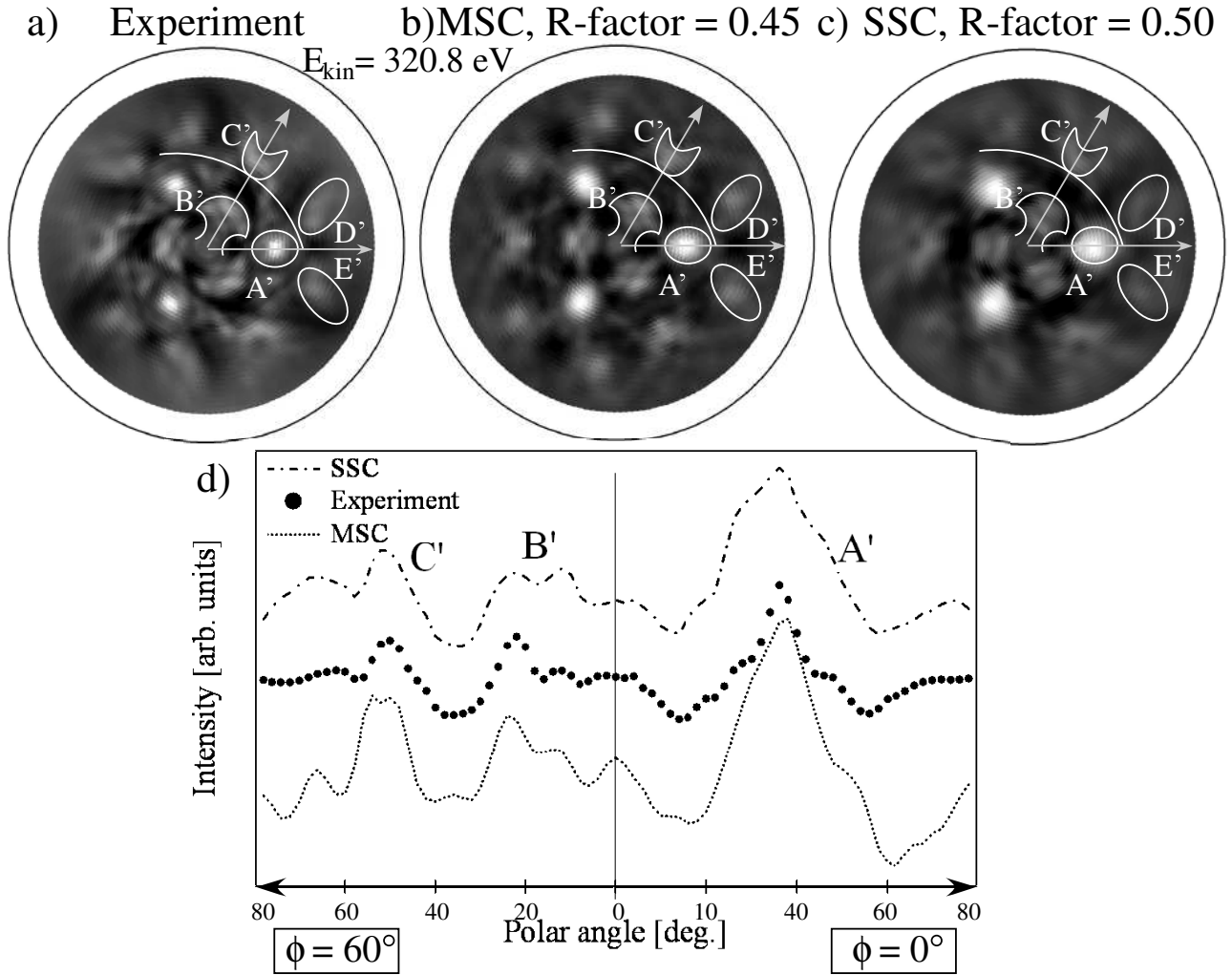


Figure 3.8: Stereographic projections of (a) measured, (b) MSC calculated and (c) SSC simulated diffractograms for Cu  $2p_{3/2}$  at 320.8 eV. (d) Polar scans as labeled.

scattering amplitudes become more isotropic. In the SSC calculation this enlargement is too prominent owing to the absence of defocusing [12]. At the diffractogram center, the intensity modulation (E) in Fig. 3.7 has been replaced by a mushroom-shaped feature (B'), with a higher intensity area on the top. Its shape and width are well reproduced in the MSC simulation. The C' structure, which was a "forward focusing" peak at higher kinetic energy, is now broader. It has a V-like shape with a small asymmetry visible in the measured and SSC interference patterns, originating from photon polarization effects owing to the oblique photon incidence in our setup. These asymmetry effects are especially visible at lower energies [6]. Presently, our special setup geometry and therefore this asymmetry behaviour cannot be simulated with EDAC. Finally, the shapes and intensities of the D' and E' regions are globally the same between experimental data and theory. Two polar cuts at  $\phi = 60^\circ$  and  $0^\circ$  are displayed in Fig. 3.8d. The A' and C' peaks, corresponding to nearest neighbour emitter-scatterer directions, are well described with the MSC approach, as well as the more complex B' feature. For the

specific polar scan, MSC does not appear better than SSC. In particular, the center part of feature A' in the experiment has a narrowness which is not reproduced in both calculations. Note that features in a localized angle-range may be better reproduced by choosing a different set of parameters but this results in a worse global agreement with a higher R-factor.

Despite the polarization effect not being taken into account by MSC, the R-factor analysis performed on the diffractograms displayed in Fig. 3.8 shows a better agreement between experiment and calculation using the MSC (R-factor  $\approx 0.45$ ) [18] than SSC (R-factor  $\approx 0.50$ ), confirming the importance to use a multiple scattering formalism to simulate diffractograms.

For a more detailed comparison of the agreement between the experiment and both calculation methods and for both kinetic energy cases, the local anisotropy,  $A = \frac{I(\theta, \phi) - I_{min}}{I_{max}}$ , is calculated for different features, as well as for the total diffractogram, and is reported in Table 3.2. The anisotropy does not give information about similarities in the shape of particular features in the different cases (MSC, experiment, SSC) but indicates the intensity variations only. First, the anisotropy has been calculated for the entire MSC, SSC and experimental diffractograms, for both  $E_{kin}=807.2$  eV and  $E_{kin}=320.8$  eV cases. In the high kinetic energy case, as shown on the left part of Table 3.2, the anisotropy of the full experimental diffractogram (55%) is more similar to the one for MSC (68%) than to the one for SSC (84%) due to the overemphasized "forward focusing" peak intensities in the latter case. For the same reason, the anisotropy values of the A and B labeled regions are more similar comparing experiment with MSC than comparing with SSC. Also, a comparable observation can be done for the two Kikuchi band modulations labeled with D and F. Globally, smaller anisotropies were obtained for the experiment and the MSC while the SSC pattern regions always show much larger anisotropy values in the high kinetic energy case. However it is the opposite in the lower energy case, right part of the Table 3.2, and especially in regions sensitive to photon polarization effects owing to the oblique photon incidence, namely the C', D', E' labeled regions but with a less dramatic difference in the entire diffractogram. Indeed, the anisotropy values of these features in the SSC are closer to experimental anisotropies than the ones calculated with MSC. However, for the A' labeled region as well as for the diffractogram center (around the normal emission) the SSC and MSC anisotropies are comparable.

Table 3.2: Anisotropies calculated on different diffractogram regions for both kinetic energy cases. (Fig. 3.7, Fig. 3.8)

Region	A( $E_{kin}=807.2$ eV)			Region	A( $E_{kin}=320.8$ eV)		
	SSC	Exp	MSC		SSC	Exp	MSC
Entire diffractogram	84%	55%	68%	<i>idem</i>	63%	49%	76%
A	66%	39%	47%	A'	48%	40%	52%
B	44%	21%	34%	C'	30%	22%	45%
D	63%	40%	33%	D'	35%	24%	50%
F	56%	22%	39%	E'	41%	28%	50%
Circle ( $0 \leq \theta < 30^\circ$ )	44%	21%	34%	<i>idem</i>	52%	38%	59%

This comparison, using the anisotropy, between both calculation methods gives complemen-

tary information about the intensity agreement of local features and complete the feature shape analysis performed above(R-factor).

#### 3.3.4 Conclusion

In the presented diffractograms, diffraction patterns are dominated by the "forward focusing" peaks along low-index crystallographic directions for both photoelectron kinetic energies. For the higher energy pattern, the relative intensities of "forward focusing" peaks are perfectly reproduced using the MSC code EDAC. Kikuchi bands and less intense peaks are also well simulated and appear with the same width and intensity in the experiment as in MSC. However, a specific doughnut shaped feature close to normal emission is not reproduced for the simulation with the best R-factor. For the lower energy pattern the "forward focusing" is less well reproduced and the difference between MSC and SSC is not as drastic. Nevertheless, for both energies, the lowest R-factors were obtained for MSC simulations, indicating the best match with experimental diffractograms. It appears that it is possible to have a good match in a limited angular range with worse agreement on the global pattern. Therefore, in order to judge a particular parameter set, the capabilities of an algorithm or simulation program, it is of prime importance to test is on an as extended as possible data set. Note that remaining inadequacies of the MSC description are certainly related to the fact that presently it is not possible to converge all available parameters simultaneously, because of memory and CPU requirements. Furthermore, if certain parameters are pushed too far, the algorithms may become numerically unstable. In general, calculations using MSC prove to be necessary to accurately simulate experimental interference patterns and increase the confidence in theoretical results, specially in peak widths and intensities. Such agreement cannot be achieved with SSC calculation.

#### Acknowledgements

We are grateful to S. Despont and M. Bravo for helpful comments during the preparation of the manuscript. Skillful technical assistance was provided by our workshop and electric engineering team. This project has been supported by the Fonds National Suisse pour la Recherche Scientifique and in part by the Office of Science, Materials Sciences Division, of the U.S. Department of Energy under Contract No. DE-AC03-76SF00098.

#### References for section 3.3

- [1] R. Fasel, P. Aebi, R. G. Agostino, D. Naumović, J. Osterwalder, A. Santaniello, L. Schlappbach, Orientation of adsorbed C<sub>60</sub> molecules determined via x-ray photoelectron diffraction, *Phys. Rev. Lett.* **76**, 4733–4736 (1996).
- [2] R. Fasel, P. Aebi, J. Osterwalder, L. Schlappbach, R. G. Agostino, G. Chiarello, Local structure of c(2×2)-Na on Al(001): Experimental evidence for the coexistence of intermixing and on-surface adsorption, *Phys. Rev. B* **50**, 14516–14524 (1994).

- [3] L. Despont, C. Lichtensteiger, F. Clerc, M. G. Garnier, F. J. Garcia de Abajo, M. A. Van Hove, P. Aebi, *Eur. Phys. J. B* **49**, 141-146 (2006) .
- [4] F. J. Garcia de Abajo, M. A. Van Hove, C. S. Fadley, Multiple scattering of electrons in solids and molecules: A cluster-model approach, *Phys. Rev. B* **63** 075404–1–16, (2001).
- [5] J. Osterwalder, T. Greber, A. Stuck, L. Schlapbach, Experimental full-solid-angle substrate photoelectron-diffraction data at 1-keV energies: implications for photoelectron holography, *Phys. Rev. B* **44**, 13764–13767 (1991).
- [6] D. Naumović, A. Stuck, T. Greber, J. Osterwalder, L. Schlapbach, Full-hemispherical photoelectron-diffraction data from Cu(001): energy dependence and comparison with single-scattering-cluster simulations, *Phys. Rev. B* **47**, 7462–7479 (1993).
- [7] R. Fasel, P. Aebi, J. Osterwalder, L. Schlapbach, Direct structural information from x-ray photoelectron diffraction: intermixing and on-surface adsorption of Na on Al surfaces, *Surf. Sci.* **331–333**, 80–87 (1995).
- [8] J. Osterwalder, P. Aebi, R. Fasel, D. Naumović, P. Schwaller, T. Kreuz, L. Schlapbach, T. Abukawa, S. Kono, Angle-scanned photoelectron diffraction, *Surf. Sci.* **331–333**, 1002–1014 (1995).
- [9] D. Naumović, J. Osterwalder, A. Stuck, P. Aebi, L. Schlapbach, Growth of Au on Cu(001) studied by full hemispherical photoelectron diffraction, *Surf. Sci.* **287–288**, 950–954 (1993).
- [10] T. Greber, J. Osterwalder, D. Naumović, A. Stuck, S. Hüfner, L. Schlapbach, Auger electron and photoelectron angular distributions from surfaces: importance of the electron source wave, *Phys. Rev. Lett.* **69**, 1947–1950 (1992).
- [11] C. S. Fadley, *Synchrotron Radiation Research: Advances in Surface Science*, Plenum, New York, 1990.
- [12] H. A. Aebischer, T. Greber, J. Osterwalder, A. P. Kaduwela, D. J. Friedman, G. S. Herman, C. S. Fadley, Material dependence of multiple-scattering effects associated with photoelectron and Auger electron diffraction along atomic chains, *Surf. Sci.* **239**, 261–264 (1990).
- [13] J. B. Pendry, *Low Energy Electron Diffraction*, Academic Press, London, 1974.
- [14] J. J. Rehr, R. C. Albers, Scattering-matrix formulation of curved-wave multiple scattering theory: Application to x-ray absorption fine structure, *Phys. Rev. B* **41**, 8139–8149 (1990).
- [15] M. P. Seah, W. A. Dench, Quantitative electron spectroscopy of surfaces: A standard data base for electron inelastic mean free paths in solids, *Surf. Interface Anal.* **1**, 2–11 (1979).
- [16] R. E. Ballard, Empirical mean free path curves for electron scattering in solids, *J. Electron Spectrosc. Relat. Phenom.* **25**, 75–78 (1982).
- [17] The parameters used are  $l_{max} = 8$  and  $\theta_D = 50$ .
- [18] The parameters used are  $l_{max} = 13$  and  $\theta_D = 150$ .



## 3.4 Multiple scattering investigation of the $1T$ -TaS<sub>2</sub> surface termination

L. Despont,<sup>1</sup> F. Clerc,<sup>1</sup> M. G. Garnier,<sup>1</sup> H. Berger,<sup>2</sup> L. Forró,<sup>2</sup> P. Aebi,<sup>1</sup>

<sup>1</sup> *Institut de Physique, Université de Neuchâtel, Rue A.-L. Breguet 1, CH-2000 Neuchâtel, Switzerland*

<sup>2</sup> *Institut de Physique de la Matière Complexe, EPFL, CH-1015 Lausanne, Switzerland*

Published in Eur. Phys. J. B **52**, 421-426 (2006)

Multiple scattering theory based on a cluster model is used to simulate full hemispherical x-ray photoelectron diffraction measurements on a  $1T$ -TaS<sub>2</sub>(0001) surface. Key points to determine the surface termination are discussed. As the commonly applied single scattering simulations do not give satisfying results, a multiple scattering approach has to be used to accurately simulate the full hemispherical photoelectron diffraction patterns. Differences and similarities between calculations of Ta and S terminated surfaces are presented along with experimental results at room temperature using both, the single and the multiple scattering approaches. We find that the surface is S terminated and that the quantitative difference between the calculations for both terminations permits to show the limits of the single scattering approach for solving surface termination problems. Moreover, by generalizing the results obtained using the multiple scattering approach, we discuss the application of this method to other similar systems.

### 3.4.1 Introduction

In general, the complete knowledge of the atom positions is necessary to understand the various properties of material's surfaces. Among the numerous techniques available to obtain information on the crystal structure, x-ray photoelectron diffraction (XPD) has proven to be very powerful, due to its chemical sensitivity and ability to measure sub-angstrom atomic displacements. However, without theoretical simulations it is often difficult to understand the different structures appearing in an XPD result and to rely them to true atomic positions. The use of multiple scattering (MSC) is unavoidable especially for bulk-emission XPD [1], as in the present case, because the simpler single scattering approach dramatically overemphasizes the so-called emitter-scatterer "forward focusing" effect, rendering the interpretation of finer interference features, which is necessary for the determination of the surface termination, very difficult.

Transition metal dichalcogenides are since long of strong interest because of their quasi-two-dimensional character, interesting electronic properties and various phase transitions. The basic structure of  $1T$ -TaS<sub>2</sub> is "sandwich-like": Hexagonal planes of Ta are sandwiched by two hexagonal S planes leading to a quasi-two-dimensional material, see Fig. 3.9. The forces between the sandwiches (of the magnitude of Van der Waals forces) are small, letting the

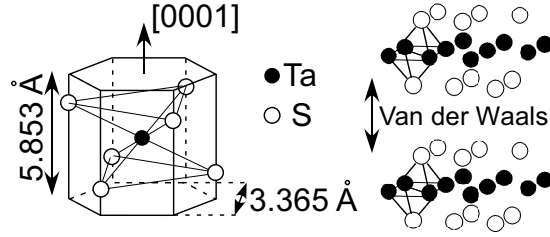


Figure 3.9: Unit cell of  $1T$ -TaS<sub>2</sub>. Ta atom (black) planes are "sandwiched" between the S atoms (white).

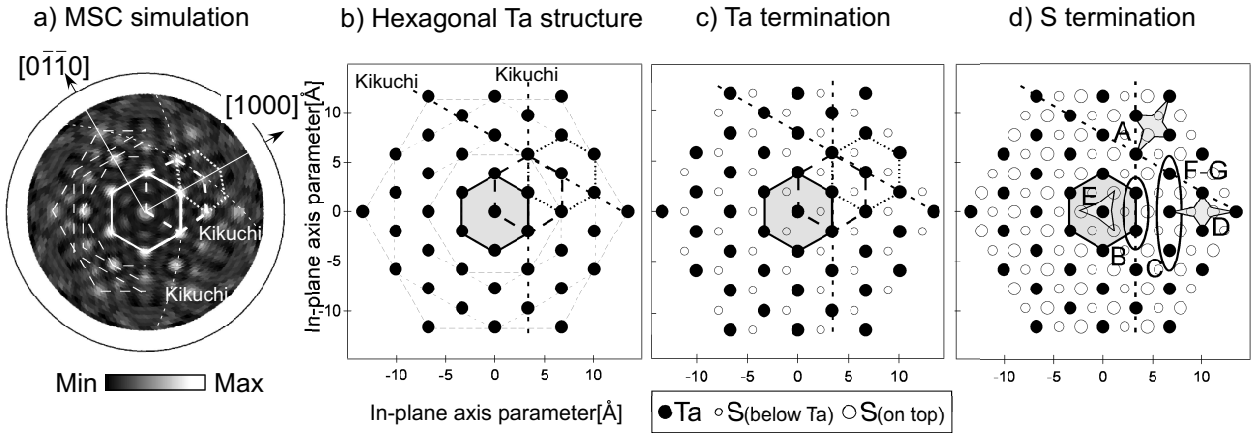


Figure 3.10: (a) Stereographic projection of the calculated Ta  $4f_{7/2}$  emission intensity of the structure shown in (b). In-plane cuts are displayed for (b) a hypothetical hexagonal Ta structure, (c) the Ta-terminated and (d) S-terminated surface. The two dashed lines in the (a)-(d) parts correspond to the low-index atomic planes from which the Kikuchi bands contained in the diffractograms originate. The labeled regions in the S-terminated cut are discussed in the text.

layered crystal be easily cleaved (between two S layers as will be shown in the present article). Similar surfaces, i.e. MoS<sub>2</sub>, NbSe<sub>2</sub> and TiSe<sub>2</sub>, were studied in the past by dynamical low energy electron diffraction [2, 3].

Here we investigate the  $1T$ -TaS<sub>2</sub> surface termination using room temperature XPD measurements together with MSC and SSC calculations. We show that the surface termination determination is very difficult using only the SSC approach while the MSC is more adapted to answer to this question. Furthermore we attempt to generalize this approach and discuss the applicability to other similar systems.

### 3.4.2 Experimental and computational details

Pure  $1T$ -TaS<sub>2</sub>, prepared by vapour transport [4, 5], was cleaved *in-situ* at a pressure in the lower  $10^{-10}$  mbar region. The surface quality was checked by low energy electron diffraction (LEED).

The XPD measurements are done in a modified Vacuum Generators ESCALAB Mk II x-ray photoelectron spectrometer equipped with a fixed hemispherical electron energy analyzer, and a three-channeltron detection system, operated with a base pressure in the lower  $10^{-11}$  mbar region. The x-ray tube contains a  $\text{MgK}\alpha$  ( $h\nu=1253.6$  eV) and  $\text{SiK}\alpha$  ( $h\nu=1740$  eV) twin anode. The samples are fixed on a computer-controlled two-axis goniometer capable of scanning the emission angle over the full hemisphere above the surface [6–11]. Data has been collected up to  $78^\circ$  polar angle.

Thanks to the chemical sensitivity of the photoemission technique, the core levels of a given type of atom can be selected. The chosen outgoing photoemitted electrons exhibit a strong anisotropic angular intensity distribution related to the local geometry around the selected atom. The analysis of the obtained diffraction patterns is simplified for electron kinetic energies higher than approximately 500eV by the so-called "forward focusing" effect. This effect consists in a strong intensity enhancement along the emitter-scatterer direction and more generally along densely packed atomic planes (resulting in so-called Kikuchi bands) and rows of atoms (corresponding to low-index crystallographic directions) [12].

Note that experimental diffractograms are acquired by simultaneously collecting electrons at two different kinetic energies: one exactly at the maximum of the Ta  $4f_{7/2}$  photoemission line ( $E_{kin}=1229$ eV) and one slightly above ( $E_{kin}=1234$ eV) to monitor the background intensity variation. The subtraction of the two signals, taking into account the channeltron sensitivities, allows to get rid of the inelastic electron background.

To simulate the XPD experiment, the cluster model approach of the EDAC (Electron Diffraction in Atomic Clusters) code [13] is used here. This code, based on the muffin-tin potential approximation [14], evaluates the MSC expansion implemented using a fully convergent recursion method.

The calculations are performed for the  $1T$  crystallographic structure (space group  $P\bar{3}m1$  and lattice parameters are  $a = b = 3.36$  Å ,  $c = 5.85$  Å ), for the Ta  $4f_{7/2}$  core level electrons ( $E_{kin} = 1229$  eV when excited with  $\text{MgK}\alpha$ ). Three Ta emitters distributed down to  $13$  Å below the surface are chosen. The calculations were performed for a temperature  $T = 300$  K and thermal vibrations are introduced by means of non-zero Debye temperatures  $\theta_D$ . To obtain a quantitative value for the agreement between calculated and measured diffractograms, an R-factor analysis based on the multipole expansion of the angular intensity distribution, *i.e.*, the expansion into spherical harmonics, has been used [16, 17]. Moreover, anisotropies of local interference features have been calculated.

### 3.4.3 Results and discussion

The MSC simulated diffractogram of a hypothetical hexagonal Ta structure is presented in Fig. 3.10a besides an in-plane cut of the crystal structure in Fig. 3.10b. The stereographically projected diffractogram is plotted using a linear gray scale with high intensity in white (the outer circle corresponds to grazing emission, whereas the center represents the normal emission direction). Three different Ta emitters are chosen. They are located in the center of the Fig. 3.10b, one at the surface and the two others just below, in the second and third unit cells. The 6-fold symmetry of the calculation is evident in Fig. 3.10a. Each peak of the diffraction pattern

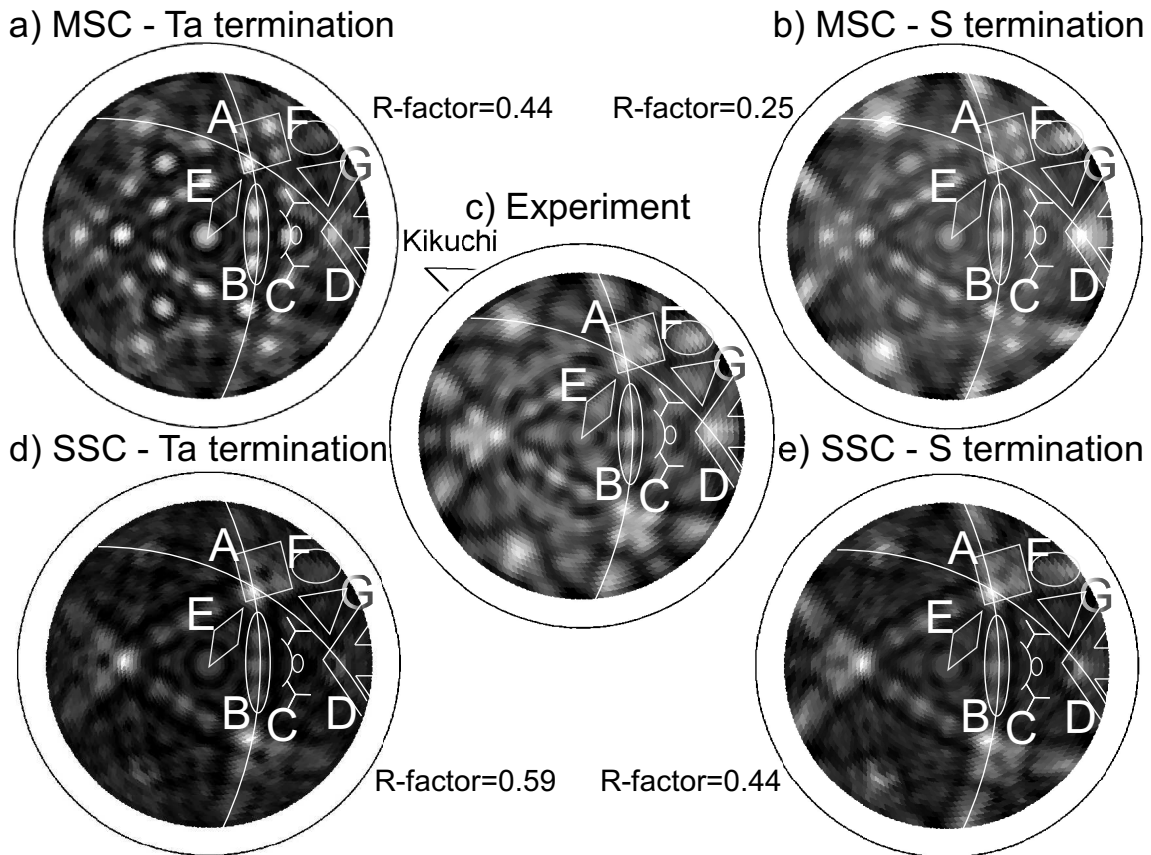


Figure 3.11: Stereographic projections of (a) MSC calculated (Ta-termination), (b) MSC calculated (S-termination), (c) measured, (d) SSC calculated (Ta-termination) and (e) SSC calculated (S-termination) diffractograms for Ta  $4f_{7/2}$  emission at 1229eV on a  $1T$ -TaS<sub>2</sub> (0001) surface.

corresponds to a "forward focusing" direction and is directly linked to a Ta-Ta direction.

The 6 most intense peaks, closest to normal emission, defining a center hexagon (plotted with a white line), are each surrounded by another hexagon (dashed line hexagon, displaced along the  $[1000]$  direction), and followed by another one (dotted). The hexagons are distorted in the diffractogram due to the stereographic projection. The discussed hexagons are plotted on the in-plane Ta structure in Fig. 3.10b and illustrate how it is possible to attribute directly each "forward focusing" peak (Fig. 3.10a) to an emitter-scatterer direction.

The insertion of S atoms into the hexagonal Ta structure, as in the  $1T$ -TaS<sub>2</sub> structure, breaks the 6-fold symmetry of the clusters as shown in Fig. 3.10c and d. MSC and SSC calculations are performed on both surfaces shown here. In the following, differences and similarities are discussed, first between the two terminations for the MSC and the SSC approaches separately and second between the two approaches.

### 3.4.3.1 Termination via multiple scattering

If the surface is either Ta-terminated (Fig. 3.11a), or S-terminated (Fig. 3.11b), the diffractograms become 3-fold symmetric, with the appearance of variations in the "forward focusing" peak intensities and the formation of other completely different structures.

In the theoretical and experimental data, see Fig. 3.11, the "forward focusing" peaks are dominant, like in the hypothetical hexagonal Ta structure shown in Fig. 3.10a. But, by introducing the S atoms, the 6-fold symmetry is broken. First, the feature labeled with A reveals four very sharp "forward focusing" peaks in the calculated Ta-terminated case, while there is more intensity inbetween in the experiment (Fig. 3.11c) and in the S-terminated case. This behavior is directly linked to the influence of the added uppermost S atom between the four Ta scatterers, see Fig. 3.10d, which does not exist in the Ta-terminated structure. A similar behavior is visible in the B labeled region, along the Kikuchi bands, as well as in the C structure, where the "forward focusing" peaks are very sharp and clearly distinct in the Ta-terminated case while they appear connected in both the experiment and the S-terminated case simulation. Note that the B labeled region contains three peaks, but not with the same intensity. The middle peak is modulated by the two neighbouring "forward focusing" peaks aligned along the Kikuchi bands, see Fig. 3.10d and by the presence or the absence of the S topmost layer. In the MSC S-terminated case and in the experiment (Fig. 3.11b and c), this middle peak has a higher intensity than the two outer ones neighbouring peaks, while it is the opposite for the Ta-terminated case (Fig. 3.11a).

The D labeled feature contains only a weak peak in the Ta-terminated case while it appears more intense and with a completely different shape in the S-terminated case, like in the experiment. The normal emission, which corresponds to the center of diffractograms, has a reduced intensity in the experiment and in the S-terminated MSC calculation, with respect to the Ta-terminated surface diffractogram. The opposite behavior is observed around the center, where the E labeled rhombus intensity is much weaker in the Ta-terminated case than in the two others diffractograms. Again, the formation of this centered three-branches star results from the scattering on the S topmost layer, as shown in Fig. 3.10d. The same observation can be made concerning the F (at the end of one Kikuchi band) and G regions.

So far, many similarities have been observed between the S-terminated crystal calculated case and the experiment and the agreement is better than for the Ta-terminated case. To evaluate the agreement between the complete experimental interference pattern data and the two theoretical cases, a global match approach, which uses the reliability R-factor, is employed and confirms what has been observed locally. The much smaller value obtained for the S-terminated case,  $R\text{-factor} \approx 0.25$ , than for the Ta-terminated case,  $R\text{-factor} \approx 0.44$ , confirms what has been obtained by eye, which does not let any doubt on the S termination.

### 3.4.3.2 Termination via single scattering

As shown in Fig. 3.11d and e, the S insertion into the hexagonal Ta structure also breaks the 6-fold symmetry, as in the MSC case. Globally, the same regions of the diffractograms can be detailed, but in the SSC case, the peaks are larger and some structures are missing in the

diffraction patterns.

In the experiment (Fig. 3.11c), the A labeled region contains four peaks of almost equal intensity while there is a clear lack of intensity for the most external peak in the SSC calculations. For both terminations, this lack is filled using the MSC approach proving the necessity of working with MSC in this system to accurately simulate the diffraction patterns. The B region is broader using the SSC as compared to MSC and the modulation of the middle peak intensity (as discussed above) is not as visible in the Fig. 3.11a and b as in the Fig. 3.11d and e. Indeed the three peaks contained in the B region have almost the same intensity in the SSC for both terminations, contrary to the MSC case. The C, D and G labeled regions show almost no intensity in the SSC calculations as compared to the experiment. However, the E and F regions are well reproduced by the SSC.

As well as for the MSC approach, we use the reliability R-factor to quantify the agreement between the complete experimental interference pattern data and the two theoretical cases. The smaller value obtained for the S-terminated case, R-factor  $\approx 0.44$ , than for the Ta-terminated case, R-factor  $\approx 0.59$ , indicates a better agreement for the S terminated surface. But the result is not as evident as for the MSC result since first, the feature shapes are broader and second, some structures are missing in SSC compared to the experiment, involving a weaker confidence in the SSC result. These differences result from known effects described in Ref. [1]. In fact, the scattering on the first few atoms has a tendency to focus the emission in the emitter-scatterer direction while on the subsequent atoms MSC tends to defocus the signal. It is a clear indication for the necessity to use MSC in order to get precise information on the intensity and shape of the "forward focusing" peaks. Note that the better agreement is not only due to the overemphasized "forward focusing" peaks obtained with the SSC approach but also due to the better agreement of the interference fine structures comparing the MSC and the experimental result.

#### 3.4.3.3 Multiple scattering vs single scattering

For a more detailed comparison of the agreement between the experiment and the simulations, the local anisotropy,  $A = \frac{I_{max}(\theta,\phi) - I_{min}(\theta,\phi)}{I_{max}(\theta,\phi)}$ , is calculated for different features. The anisotropy does not give information about similarities in the shape of particular features in the three different cases (Ta-terminated surface, S-terminated surface and experiment) but indicates the intensity variations only.

The local anisotropy calculated for the different features are generally closer to the experiment for the S-terminated surface. For example, the anisotropies for the A labeled feature are 33.2% for the experiment, 44.8% and 46.7% for the MSC for the S- and Ta-termination while they are 69.3% and 76.2%, respectively, for the SSC approach. In this later case, the local anisotropies are much larger than those of the experiment. The same behavior is observed for the B, C, and D features.

Moreover, to obtain a quantitative indication of the diffraction pattern intensity variation owing to the S topmost layer, the two different diffractograms (S- and Ta- terminated surface) have been subtracted and then normalized as shown in Eq. 3.5. Note that both clusters have the same reference system to insure that the signal attenuation due to the escape depth is equal

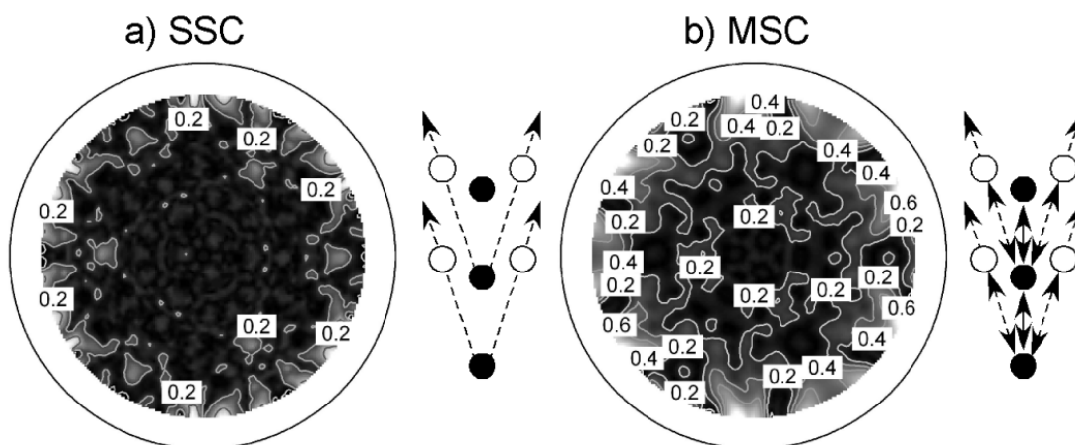


Figure 3.12:  $I_{Diff}(\theta, \phi)$  calculated for the (a) SSC and the (b) MSC approaches. The contour plots indicate the larger differences in both cases.

and thus that the calculated difference only contains information about the S topmost layer presence.  $I_{Diff}(\theta, \phi)$  is given by:

$$I_{Diff}(\theta, \phi) = \frac{|I_{S-term.}(\theta, \phi) - I_{Ta-term.}(\theta, \phi)|}{(I_{S-term.}(\theta, \phi) + I_{Ta-term.}(\theta, \phi))/2} \quad (3.5)$$

and is plotted in Fig. 3.12a and b for the SSC and MSC approaches. A larger difference is obtained for grazing emission angles, for both the SSC and MSC calculations. This is a logic consequence of the fact that by looking at grazing angle, the surface contribution is amplified compared to the one of the bulk. Indeed, the signal decreases proportionately to  $e^{-\frac{d}{\lambda}}$ , where  $\lambda$  is the electron inelastic mean free path and  $d$  is the path length. Emission from deeper lying emitters is thus strongly attenuated since it corresponds to long paths  $d$  at grazing emission.

Near normal emission,  $I_{Diff}(\theta, \phi)$  is only significant in the MSC case. This variation corresponds to the bulk emission sketched in Fig. 3.12. In SSC, the final emitted signal along a given "forward focusing" direction is proportional to the same emitter-scatterer signal multiplied by  $e^{-\frac{d_1}{\lambda}} + e^{-\frac{d_2}{\lambda}} + \dots$ , where  $d_i, i = 1, 2, \dots$ , are the emitter depths, depending on the number of emitters taken into account.

On the contrary, in MSC each scattering process (in all directions) contributes to modify independently the emitter-scatterer signal coming from the different emitters. It involves an intensity transfer (which is not considered in the SSC approach) between all the scatterers. As all the emissions are finally scattered by the topmost layer before escaping, the scattering contribution of the surface atoms is increased, leading to an enhancement of the influence of the surface termination.

This result is corroborated by the difference in the R-factor which can also be interpreted in these terms. Indeed, the difference in the R-factor between both terminations is 0.19 for the MSC (reduction of 76%) while it is 0.15 for the SSC (reduction of 34.1%). It indicates that there are less differences between the two terminations relative to the experiment for the SSC approach compared to MSC, leading to a larger sensitivity of the MSC to the S termination.

### 3.4.3.4 Generalization

In this section, key points to determine the surface termination for bulk-emission with the MSC approach are discussed. Based on the above results, and to obtain a quantitative indication about the nature of the surface topmost layer, we compare  $\langle I_{Diff.}(\theta, \phi) \rangle$  averaged over all  $(\theta, \phi)$  angles for different cases, thereby giving a simple measure to differentiate the two surface terminations. Three different parameters are modified, the *c*-axis parameter, the scatterer type and the stacking sequence. The other parameters are fixed, leading to hypothetical materials systems.

$\langle I_{Diff.}(\theta, \phi) \rangle$  is shown in Fig. 3.13 for *c*-axis parameters between 5.853 (bulk value) and 3.75 Å, for different kinds of scatterers (O, S, Se), and for the two most natural stacking sequences, the so-called 1*T* and 2*H* polytypes. The values obtained for the case studied in Fig. 3.12 ( $c = 5.853$  Å, 1*T*-TaS<sub>2</sub>) are reported in Fig. 3.13, left. First, as the *c*-axis becomes smaller,  $\langle I_{Diff.}(\theta, \phi) \rangle$  decreases. This is due to the increasing contribution of the bulk emission to the whole signal due to the electron inelastic mean free path. Indeed, as the *c*-axis is reduced, the emitter depths are also reduced and the signal coming from deep emitters is less attenuated. Consequently, the contribution of the topmost layer emission, and thus the difference between both terminations, is reduced relative to the whole signal. As plotted in Fig. 3.13, this attenuation is weakly dependent on the scatterer type. Nevertheless the  $\langle I_{Diff.}(\theta, \phi) \rangle$  variation as a function of the *c*-axis value becomes larger for heavy scatterers.

Next, we substitute the S atoms of the 1*T*-TaS<sub>2</sub> structure by two other scatterers, namely O and Se atoms. By changing scatterers, phase shifts are naturally changed, affecting the scattering strengths. This effect is well seen in Fig. 3.13. When S atoms of the 1*T*-TaS<sub>2</sub> are substituted by O atoms,  $\langle I_{Diff.}(\theta, \phi) \rangle$  drastically decreases, and becomes even lower than the reference value obtained by the SSC approach. For such a substitution, the Ta-Ta emission dominates the entire diffraction pattern and at the same time the Ta-O scattering becomes negligible [18]. This observation suggests that for too light scatterers (small scattering strength), it becomes very difficult to determine the surface termination for bulk-emission with this method. However, when S atoms of the 1*T*-TaS<sub>2</sub> are substituted by Se atoms,  $\langle I_{Diff.}(\theta, \phi) \rangle$  increases, leading to a larger sensitivity to the surface topmost layer.

Finally,  $\langle I_{Diff.}(\theta, \phi) \rangle$  has been calculated for the 2*H*-TaS<sub>2</sub> stacking sequence. As shown in Fig. 3.13, both 1*T* and 2*H* stacking sequences exhibit a similar  $\langle I_{Diff.}(\theta, \phi) \rangle$ , indicating that the stacking is not crucial for the surface topmost layer determination procedure.

The best R-factor has been obtained for the 1*T* stacking sequence, the *c*-axis parameter corresponding to 5.95 Å (corresponding to a slight (2%) surface relaxation) and obviously using S atoms as scatterers. For comparison, R-factor  $\approx 0.31$  and 0.55 have been obtained with the 2*H* stacking for the S- respectively Ta- surface termination. This R-factor is worse (by  $\approx 28\%$ ) than what is obtained for the 1*T* polytype (0.25, 0.44) showing the sensitivity of XPD to the stacking sequence.

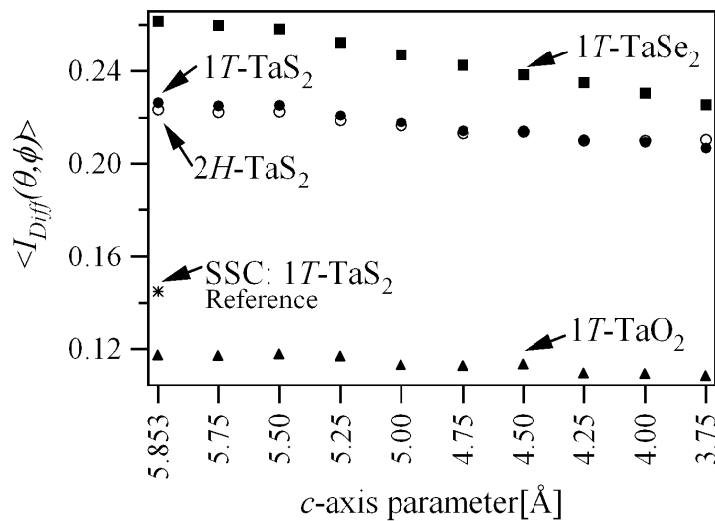


Figure 3.13:  $\langle I_{Diff}(\theta, \phi) \rangle$  calculated for different  $c$ -axis parameters, kind of scatterers and stacking sequences. The value obtained with the SSC approach shown in Fig. 3.12 is reported here as reference. The filled and empty markers correspond to the  $1T$  and  $2H$  stacking sequences respectively.

### 3.4.4 Conclusion

In all the presented experimental and calculated diffractograms, diffraction patterns are dominated by the "forward focusing" peaks along low-index crystallographic directions. But as seen, the variations of the peak widths, shapes and intensities are also strongly linked to the S atom presence at the surface. A larger confidence can be obtained with the MSC approach owing to a better agreement with the experiment (seen by eye and calculated via the R-factor). Moreover, it appears that the contribution of the topmost S layer is quantitatively very strong in the MSC approach, which permits to clearly distinguish both terminations. It is shown that the full hemispherical XPD combined with the MSC approach is a powerful method to determine the surface termination for bulk-emission and may be applied to similar systems in the future.

A generalization of this approach for other systems is discussed. It appears that for a chosen emitter it becomes very difficult to determine the surface termination with this method for too light scatterers. Finally, by comparing the R-factor for the two most natural polytypes ( $1T$ ,  $2H$ ) it is shown that XPD is also sensitive to the stacking sequence.

## Acknowledgements

We would like to thank the whole Neuchâtel workshop and electric engineering team for efficient technical support. This project has been supported by the Fonds National Suisse pour la Recherche Scientifique.

#### References for section 3.4

- [1] L. Despont, D. Naumović, F. Clerc, C. Koitzsch, M. Garnier, F. G. de Abajo, M. V. Hove, P. Aebi, X-ray photoelectron diffraction study of Cu(1 1 1): Multiple scattering investigation, *Surf. Sci.* **600** (2006) 380–385.
- [2] B. J. Mrstik, R. Kaplan, T. L. Reinecke, M. V. Hove, S. Y. Tong, Surface-structure determination of the layered compounds MoS<sub>2</sub> and NbSe<sub>2</sub> by low-energy electron diffraction, *Phys. Rev. B* **15** (1977) 897.
- [3] M. Kasch, E. Pehlke, W. Schattke, T. Kurberg, H. P. Barnscheidt, R. Manzke, M. Skibowski, Leed intensities of TiSe<sub>2</sub> including off-normal electron incidence, *Surf. Sci.* **214** (1989) 436–447.
- [4] B. Dardel, M. Grioni, D. Malterre, P. Weibel, Y. Baer, F. Lévy, Temperature-dependent pseudogap and electron localization in 1T-TaS<sub>2</sub>, *Phys. Rev. B* **45** (3) (1992) 1462–1465.
- [5] B. Dardel, M. Grioni, D. Malterre, P. Weibel, Y. Baer, F. Lévy, Spectroscopic signatures of phase transitions in a charge-density-wave system: 1T-TaS<sub>2</sub>, *Phys. Rev. B* **46** (12) (1992) 7407–7412.
- [6] J. Osterwalder, T. Greber, A. Stuck, L. Schlapbach, Experimental full-solid-angle substrate photoelectron-diffraction data at 1-keV energies: implications for photoelectron holography, *Phys. Rev. B* **44** (24) (1991) 13764–13767.
- [7] D. Naumović, A. Stuck, T. Greber, J. Osterwalder, L. Schlapbach, Full-hemispherical photoelectron-diffraction data from Cu(001): energy dependence and comparison with single-scattering-cluster simulations, *Phys. Rev. B* **47** (12) (1993) 7462–7479.
- [8] R. Fasel, P. Aebi, J. Osterwalder, L. Schlapbach, Direct structural information from x-ray photoelectron diffraction: intermixing and on-surface adsorption of Na on Al surfaces, *Surf. Sci.* **331–333** (1995) 80–87.
- [9] J. Osterwalder, P. Aebi, R. Fasel, D. Naumović, P. Schwaller, T. Kreutz, L. Schlapbach, T. Abukawa, S. Kono, Angle-scanned photoelectron diffraction, *Surf. Sci.* **331–333** (1995) 1002–1014.
- [10] D. Naumović, J. Osterwalder, A. Stuck, P. Aebi, L. Schlapbach, Growth of au on Cu(001) studied by full hemispherical photoelectron diffraction, *Surf. Sci.* **287–288** (1993) 950–954.
- [11] T. Greber, J. Osterwalder, D. Naumović, A. Stuck, S. Hüfner, L. Schlapbach, Auger electron and photoelectron angular distributions from surfaces: importance of the electron source wave, *Phys. Rev. Lett.* **69** (13) (1992) 1947–1950.
- [12] C. S. Fadley, *Synchrotron Radiation Research: Advances in Surface Science*, Plenum, New York, 1990.
- [13] F. J. Garcia de Abajo, M. A. Van Hove, C. S. Fadley, Multiple scattering of electrons in solids and molecules: A cluster-model approach, *Phys. Rev. B* **63** (2001) 075404–1–16.

- [14] J. B. Pendry, *Low Energy Electron Diffraction*, Academic Press, London, 1974.
- [15] J. J. Rehr, R. C. Albers, Scattering-matrix formulation of curved-wave multiple scattering theory: Application to x-ray absorption fine structure, *Phys. Rev. B* **41** (12) (1990) 8139–8149.
- [16] R. Fasel, P. Aebi, J. Osterwalder, L. Schlapbach, R. G. Agostino, G. Chiarello, Local structure of  $c(2 \times 2)$ -Na on Al(001): Experimental evidence for the coexistence of intermixing and on-surface adsorption, *Phys. Rev. B* **50** (19) (1994) 14516–14524.
- [17] R. Fasel, Adsorbed monolayers and submonolayers studied by angle-scanned photoemission, Ph.D. thesis, University of Fribourg (1996).
- [18] L. Despont, C. Lichtensteiger, F. Clerc, M. G. Garnier, F. G. Garcia de Abajo, M. V. Hove, J.-M. Triscone, P. Aebi, X-ray photoelectron diffraction study of ultrathin  $\text{PbTiO}_3$  films, *Eur. Phys. J. B* **49** (2006) 141–146.



## 3.5 InN surface polarity investigated by single scattering

### 3.5.1 Introduction

The kind of surface polarity is of considerable fundamental and practical interest concerning the crystal structure of the III-nitrides. More particularly, the basal (0001)-plane of such a crystal is a bilayer containing two closely spaced hexagonal arrangements of anions and cations. In these bilayers, either the anions (the metal ions) or the cations (the nitrogen ions) are sitting on top and determine whether we have to deal with group III or group V-face material.

Theoretical calculations predict that on sapphire, the so-called III-face surface is energetically more favorable [1]. At a strained GaN/AlGaN interface, the occurrence of a 2 dimensional electron gas is an indirect proof of the type of surface polarity [2]. At a more heavily strained InN/InGaN-interface, however, this method does generally not work well.

Other non-destructive methods like the x-ray standing wave method, Auger electron spectroscopy, electron diffraction or ion channeling have been used to determine the polarity of GaN and AlN [3]. XPD was reported for GaN samples fabricated with different growth methods [4], whereas convergent beam electron diffraction is the only non-destructive method used so far on InN [5].

There exist also a couple of destructive methods, like chemical etching procedures, which are especially suited for GaN [6]. In the past, XPD has been employed for investigations of tetragonality, surface termination, and crystal orientation in various materials, including GaN [4, 7, 8]. Indeed, owing to the chemical sensitivity of the XPD, local atomic structure around a given atom can be probed. Here, we use this versatile technique to determine the polarity of 1  $\mu\text{m}$  thick, high quality InN films.

### 3.5.2 Experimental and computational details

Fabrication of these layers was accomplished by plasma-assisted molecular beam epitaxy in the Department of Electrical and Computer Engineering at Cornell University. The structure is grown on C-face sapphire substrates and contains a 50 nm thick AlN nucleation layer, followed by roughly 250 nm of GaN. Between this buffer and the subsequent 1 micron thick InN layer, a 6 period InN/InGaN superlattice with a nominal period of 15 nm was inserted. The purpose of this stack was to bend dislocations and to improve the following InN material quality. The InN layer itself was grown by migration enhanced epitaxy, a growth method which offers indium and nitrogen atoms in an alternate way and never at the same time. At present this growth method results in the highest possible quality of InN. Note that prior to the measurements, the InN surface was cleaned *in situ* using soft oxygen plasma in order to increase the XPD signal.

In order to better understand the collected data, single-scattering calculations have been performed to simulate the experimental diffractograms. No structure optimization has been made; instead, the usual InN lattice parameters have been employed ( $a=b=3.544 \text{ \AA}$  and  $c=5.718 \text{ \AA}$ ) to create a cluster containing 1211 atoms. For the selected In  $3d_{5/2}$  photoelectron kinetic energy ( $E_{kin} = 809.5 \text{ eV}$ ), the photoelectron inelastic mean free path is about  $8 \text{ \AA}$  and therefore

we have chosen as emitters five In atoms down to a depth of approximately 12 Å below the surface. To obtain a quantitative value of the agreement between calculated and measured diffractograms, a reliability R-factor analysis has been used.

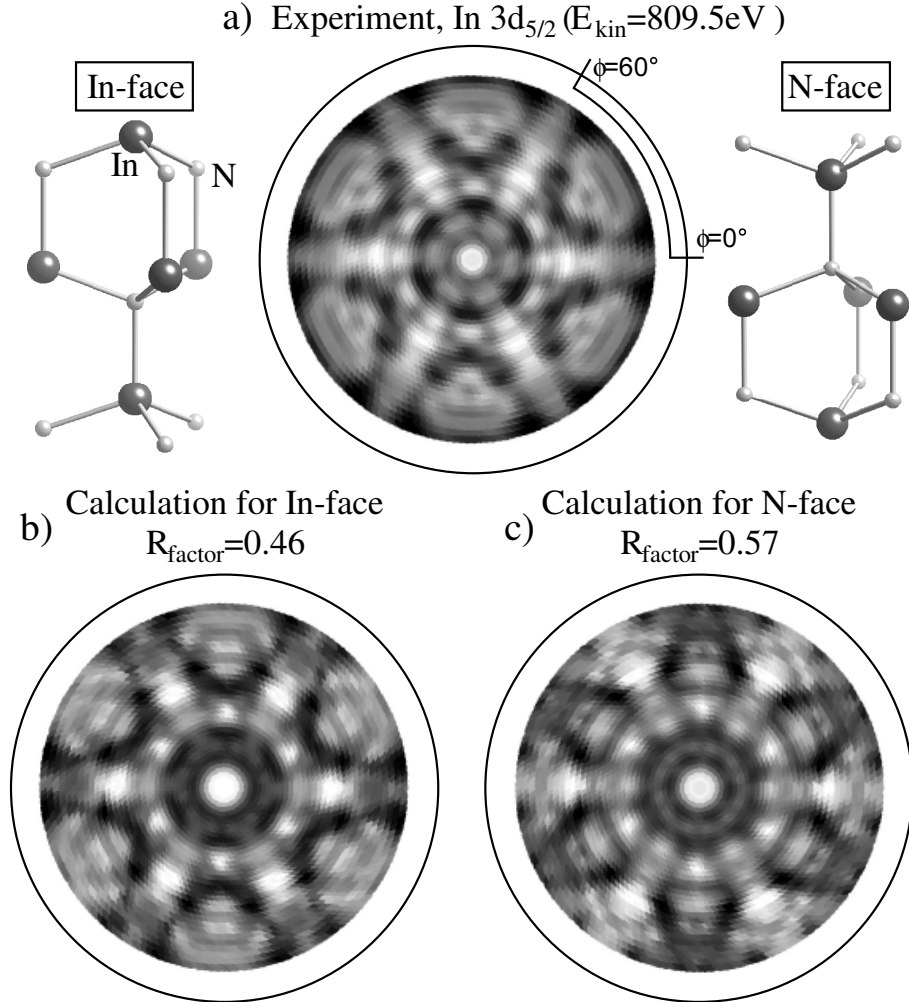


Figure 3.14: Stereographic projections of (a) measured and (b), (c) 2-fold symmetrized single-scattering simulated diffractograms for the In- and N-face respectively, for In 3d<sub>5/2</sub> photoelectrons at 809.5 eV (MgK $\alpha$ ).

### 3.5.3 Results and discussion

Measured and calculated diffractograms of InN(0001) 3d<sub>5/2</sub> are presented in Fig. 3.14 using the same linear gray scale and stereographic projection. According to the InN crystal structure, a threefold symmetrisation has been applied to the experimental diffractogram. This purely mathematical operation improves the contrast of the measured diffractogram. However, even without performing this symmetrisation procedure, the obtained result is six-fold symmetric. It suggests that the InN crystal surface is either made of two different domains rotated by 60°

around the [0001] axis with respect to each other or contained steps of half unit cells. The XPD measurement is not capable to distinguish between the two possibilities which create both a 2-fold symmetry of the diffraction pattern.

This observation made by eye has been confirmed by a global match approach which uses the afore-mentioned reliability R-factor. For both In-face and N-face material, smaller R-factor values (i.e. better agreement) are obtained for the 2-fold symmetry as shown in Table 3.3.

Moreover, the best agreement between the experiment and the single-scattering calculation is obtained for an In-face termination. This is in agreement with the result obtained by surface etching in Ref. [9].

	Without folding	2-fold symmetry
In-face	0.65	0.46
N-face	0.67	0.57

Table 3.3: R-factor calculated between the experimental diffractogram and single-scattering calculations for the two possible configurations and two different symmetrizations. The smallest R-factor corresponds to the best agreement.

### References for 3.5

- [1] A.R. Smight, R.M. Feenstra, D.W. Greve, J. Neugebauer, and J.E. Northrup, *Phys. Rev. Lett.* **79**, 3934 (1997).
- [2] O. Ambacher, J. Majewski, C. Miskys, A. Link, M. Hermann, M. Eickhoff, M. Stutzmann, F. Bernardini, V. Fiorentini, V. Tilak, B. Schaff, and L.F. Eastman, *Pyroelectric properties of Al(in)GaN/GaN hetero- and quantum well structures*, *J. Phys.: Condens. Matter* **14**, 3399 (2002).
- [3] A. Kazimirov, G. Scherb, J. Zegenhagen, T.-L. Lee, M.J. Bedzyk, M.K. Kelly, H. Angerer, and O. Ambacher, *Polarity determination of a GaN thin film on sapphire (0001) with x-ray standing waves*, *J. Appl. Phys.* **84**, 1703 (1998) and references therein.
- [4] M. Seelmann-Eggebert, J. L. Weyher, H. Obloh, H. Zimmermann, A. Rar, and S. Porowski, *Polarity of (00.1) GaN epilayers grown on (00.1) sapphire*, *Appl. Phys. Lett.* **71**, 2635 (1997).
- [5] T. Mitate, S. Mizuno, H. Takahata, R. Kakegawa, T. Matsuoka, and N. Kuwano, *InN polarity determination by convergent-beam electron diffraction*, *Appl. Phys. Lett.* **86**, 134103 (2005).
- [6] J.L. Rouviere, J.L. Weyher, M. Seelmann-Eggebert, and S. Porowski, *Polarity determination for GaN films grown on (0001) sapphire and high-pressure-grown GaN single crystals*, *Appl. Phys. Lett.* **73**, 668 (1998).

- [7] L. Despont, C. Koitzsch, F. Clerc, M.G. Garnier, P. Aebi, C. Lichtensteiger, J.-M. Triscone, F.J. Garcia de Abajo, E. Bousquet, and Ph. Ghosez, Direct evidence for ferroelectric polar distortion in ultrathin lead titanate perovskite films, *Phys. Rev. B* **73**, 094110 (2006).
- [8] L. Despont, F. Clerc, M.G. Garnier, H. Berger, L. Forr and P. Aebi, Multiple scattering investigation of the 1T-TaS<sub>2</sub> surface termination, *Eur. Phys. J. B* **52**, 421 (2006).
- [9] R.P. Bhatta, B.D. Thoms, M. Alevli, V. Woods, and N. Dietz, Surface structure, composition, and polarity of InN grown by high-pressure chemical vapor deposition, *Appl. Phys. Lett.* **88**, 122112 (2006).

# Chapter 4

## Local structure of Nb-SrTiO<sub>3</sub>

### 4.1 Introduction

Owing to its high dielectric constant, SrTiO<sub>3</sub> (STO) is a promising material that has the potential to replace silicon dioxide in some nanoelectronic devices. Moreover, STO is considered as a standard model to study oxide surfaces and is widely used as substrate for epitaxial film growth.

Here, Nb doped(0.5%) STO has been used as substrate as it exhibits almost the same lattice constant than PTO, preventing an in-plane lattice strain. Indeed a large stress due to a lattice mismatch can artificially increase the PTO tetragonality, which in turn will enhance its polarization.

During the last three decades, many different aspects of the STO have been studied. Like other perovskite compounds, STO shows a complex physical behavior. Its cubic ( $a=3.902\text{\AA}$ ) structure turns into a tetragonal phase at  $T < 105\text{K}$  but remains paraelectric for all temperatures. In the ideal non-reconstructed state, both TiO<sub>2</sub> and SrO terminations are possible. However, depending on various conditions, as temperature, atmosphere, doping, defect density, the picture becomes much more complex. For instance Jiang has reported  $c(6 \times 2)$  and  $c(4 \times 2)$  surface reconstruction of STO and suggested that the final ordering depends not only on the annealing conditions, but critically on the surface condition before the annealing [1].<sup>a</sup> Andersen has studied the effect of the Ca concentration on the STO surface reconstruction [2] while Erdman and Gunhold have shown how the  $(2 \times 1)$ ,  $c(4 \times 2)$  and  $c(6 \times 2)$  surface reconstructions were obtained under different oxidizing conditions on the STO (001) and (110) surface [3, 4]. The results obtained by different groups can sometimes differ or can be even contradictory, indicating the sensitivity of STO surface structures to preparation procedures. The aim of this chapter is not to entirely solve the problem of the STO surface preparation and characterization but to sensitize the reader to some aspects between the structure and chemistry of STO surfaces.

---

<sup>a</sup>According to Jiang, a  $c(4 \times 2)$  surface can be obtained by annealing the surface with the assistance of hydrogen, while annealing an O<sub>2</sub> pre-treated surface both with and without hydrogen generates a  $c(6 \times 2)$  reconstruction.

Several theoretical [5] and experimental [3,6–8] studies have been performed on the STO electronic structure. For instance the electronic structure of STO surfaces with defects produced by Ar ion sputtering, surfaces annealed before and after the ion sputtering and surfaces with adsorbed O<sub>2</sub> [9] have already been studied. Therefore, this aspect has not been discussed in the present thesis.

This chapter is organized as follows. The Section 4.2 is dedicated to XPD measurements and a MSC analysis which shows that the STO surface exhibits an unexpected polar distortion analogous to the one observed in PTO films and discussed in Chapter 5. Then in Section 4.3, a (1 × 1) surface obtained with different cleaning procedures is shown together with XPS measured after each cleaning process. The result is then discussed and general conclusions are given.

## 4.2 X-ray photoelectron diffraction on Nb-SrTiO<sub>3</sub>

### 4.2.1 Experimental results

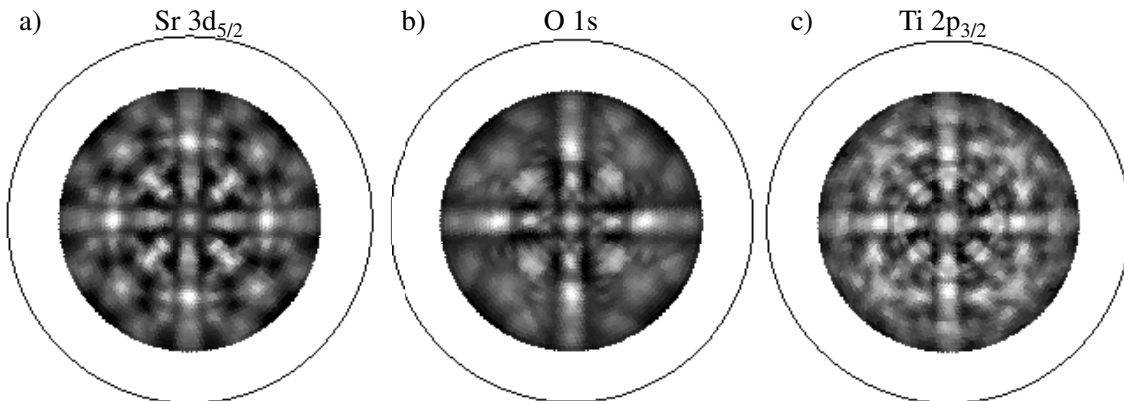


Figure 4.1: Experimental diffractograms up to  $\theta = 70^\circ$  for a Nb-STO substrate. MgK $\alpha$  excited (a) Sr3d<sub>5/2</sub>, (b) O1s and (c) Ti2p<sub>3/2</sub> photoelectrons.

Photoelectron diffraction patterns are plotted in Fig. 4.1a-c for a bare Nb-STO substrate. No surface cleaning procedure was applied and measurements were performed at room temperature. Despite the presence of surface contaminations, such as C and O, we obtain well-defined XPD patterns for the three selected emission kinetic energies, corresponding to the Sr3d<sub>5/2</sub>, O1s and Ti2p<sub>3/2</sub> emissions. Note that STO is an insulator in its primary state and thus hardly measurable using photoelectron spectroscopy. When it is reduced in UHV (heating to about 1000K for several hours), it becomes *n*-type with a maximum carrier concentration of the order of 10<sup>19</sup> electrons/cm<sup>3</sup> [9]. By doping cations such as Nb<sup>5+</sup>, the STO has also an *n*-type conductivity while *p*-type STO can be obtained if acceptor ions (Sc<sup>3+</sup>) are introduced into Ti<sup>4+</sup> ion sites [6].

As the structure of STO is very similar to the PTO which is presented thoroughly in Chapter 5, no detailed XPD analysis will be done. The only difference worth to be mentioned is that at room temperature, the STO is cubic while PTO is tetragonal, implying a measurable (using Sr3d<sub>5/2</sub> and Pb4f<sub>7/2</sub> emission lines) forward focusing peak position variation between both samples. This observation is discussed in Section 5.3.

## 4.2.2 Multiple scattering investigation

A structure optimization of the STO has been performed using the MSC approach for the O1s emission. The results ( R-factor grids ) are shown in Fig. 4.2a-d. Each figure shows R-factor values calculated between the measured XPD pattern (shown in Fig. 4.2e) and different MSC calculations obtained with various O and Ti atom positions, for one given *c*-axis structure parameter. O and Ti atoms have been shifted along the *c*-axis direction relative to the centrosymmetric position. The vertical and horizontal R-factor grid axis correspond to O and Ti shifts respectively. *c*-axis parameters between 3.7 and 4 Å are chosen. The MSC calculation corresponding to the smallest R-factor (= 0.34) is shown in Fig. 4.2f.

The minimal R-factor values correspond to the dark part of the R-factor grids. A paraelectric structure at the surface would lead to a minimal R-factor value located in the center of the grid, which is not the case here.

First, an approximately 0.4Å positive shift of the O atoms along the *c*-axis permits to decrease the R-factor values, almost independently of the *c*-axis parameter. This value corresponds to  $\approx 0.1/c$  while a shift of  $0.1118/c$  is obtained for the ferroelectric PTO [10]. This result suggests that, contrary to long-established beliefs, the STO surface is not paraelectric, but exhibits a polar distortion analogous to the one observed in PTO films.

Second, the R-factor grids suggest a more confusing behavior concerning Ti atom shifts. Indeed the determination of the Ti shift shows a larger uncertainty which indicate that shifts of Ti atoms in the two directions are compatible with our measurements. A structure optimization has been performed for the Ti emission including the presence of alternative up- and down-state Ti atom shifts, with different amplitudes, but no satisfying R-factor has been obtained up to now by comparing the measured experiment and MSC simulations calculated with this wide range of Ti atom positions. In parallel, based on the Sr emission diffraction pattern, we have been able to confirm the cubic structure of the STO surface, as shown in Section 5.3.

## 4.3 Nb-SrTiO<sub>3</sub> surface reconstruction

As discussed in the Introduction section of this chapter, many different surface reconstructions can be obtained using different preparation procedures. The aim of this section is to emphasize some aspects regarding the structure and chemistry at STO surfaces.

To permit a wide variety of cleaning procedures and more specifically to heat the sample in a gaz or plasma atmosphere, we built the sample holder described in Fig. 4.3. With this sample holder, it is possible to directly pass a given current through the sample laying on an

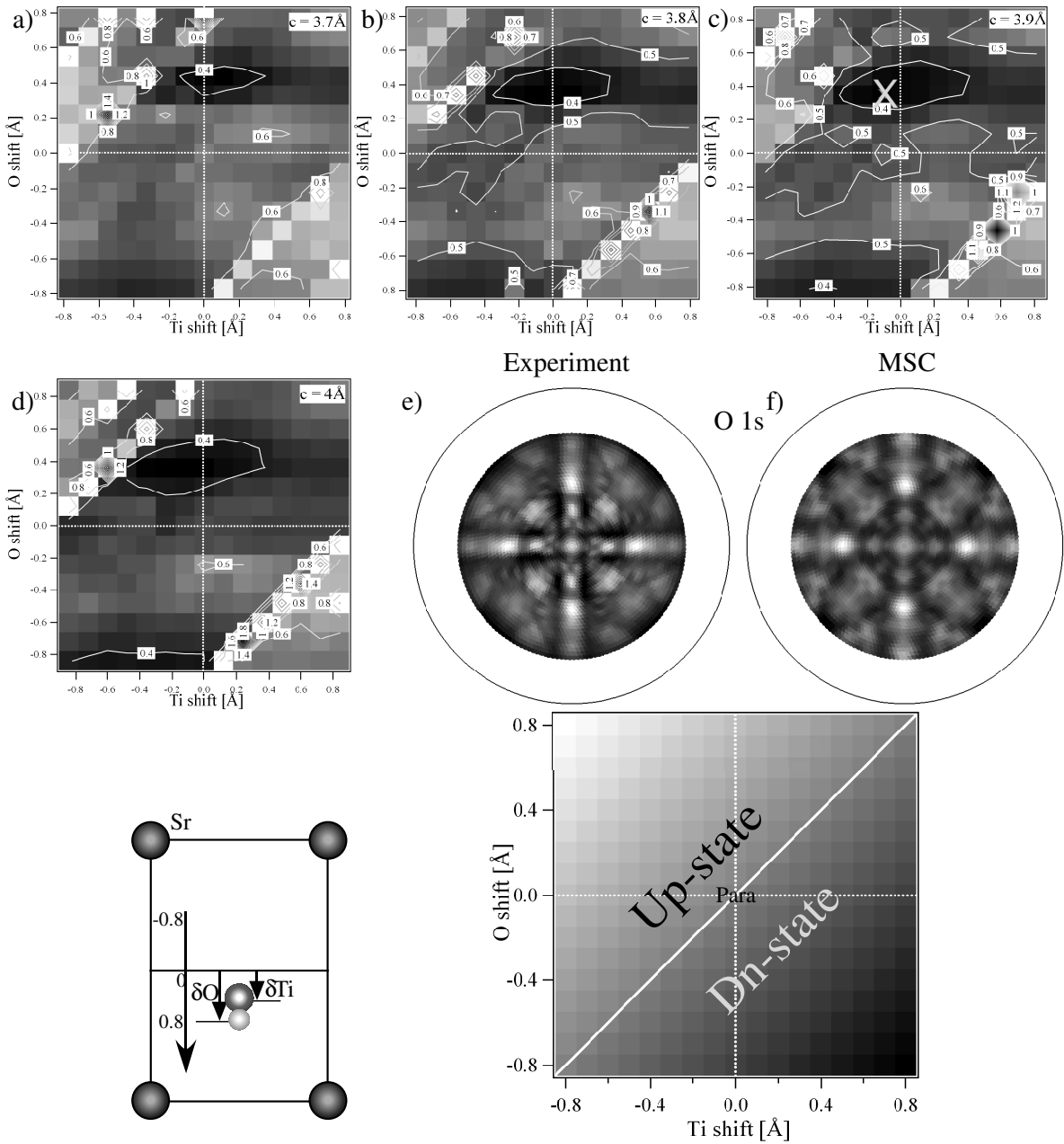


Figure 4.2: (a)-(d) R-factor grids for different  $c$ -axis parameters. Each figure shows the R-factor variation when O and Ti atoms are shifted along the  $c$ -axis from  $-0.8 \text{ \AA}$  to  $0.8 \text{ \AA}$  relative to their centro-symmetric position. The negative value of the O and Ti shifts corresponds to the down-state while positive value corresponds to the up-state. The measured diffractogram is shown in (e) together with the MSC calculation corresponding to the best R-factor in (f). The best R-factor is founded in grid (c) and is represented with a gray x. The dotted white lines correspond to the centro-symmetric position.

insulator sapphire plate, permitting to heat the sample at high temperatures in UHV without degassing all the sample holder for a long time.

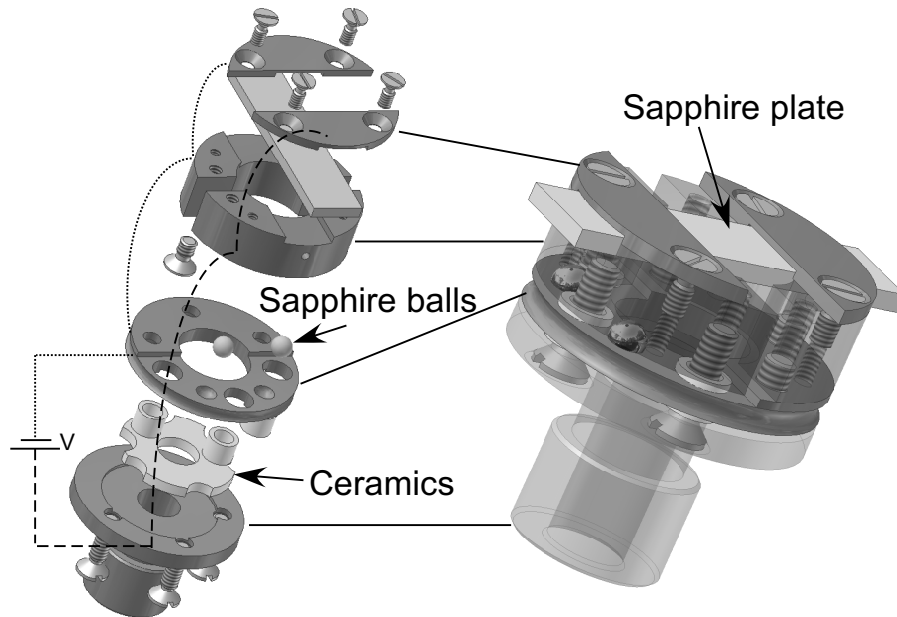


Figure 4.3: Sample holder which permits to heat different size samples (in UHV, plasma or gaz atmosphere) using direct current. With the small thermic exchange surface between the sample and the sample holder, the degassing time is reduced.

Two different cleaning procedures have been applied to a Nb-STO bare substrate to obtain a  $(1 \times 1)$  surface. In the first case, which will be called the "plasma" recipe, the STO has been annealed up to  $400^\circ\text{C}$  for 10min and then flashed at  $1000^\circ\text{C}$  in UHV. At this stage, the LEED shows a  $c(2 \times 2)$  surface reconstruction<sup>b</sup> (Fig. 4.4a). Then an O-plasma (50W, 0.02mbar, 1min) has been applied to this surface reconstruction. The corresponding LEED measurement is shown in Fig. 4.4b) and revealed a  $(1 \times 1)$  surface.

In the second case, another cleaning procedure has been applied [4], which will be called the "standard" recipe. The sample has been annealed at  $830^\circ\text{C}$  for 60min in vacuum and for 10min in  $10^{-5}$ mbar of O<sub>2</sub>. The LEED of the surface obtained using this cleaning procedure is shown in Fig. 4.4c. The same  $(1 \times 1)$  surface has been obtained as in the first case after the plasma exposure.

So both treatments give the same LEED, but XPS measurements performed at the different stages of cleaning reveal drastic modifications of the surface chemistry, as shown in Fig. 4.4d. The O1s emission line measured on the exposed-to-air raw sample (continuous line) is composed of two visible structures due to oxygen atoms in different environments. The more intense peak

<sup>b</sup>Note that other preparation procedures can be applied to obtain a  $c(2 \times 2)$  surface reconstruction. For instance, if a low current ( $\approx 0.15\text{Amps}$ , which corresponds here to less than  $100^\circ\text{C}$ ) passes through the sample during enough time, such surface reconstruction can be created, according to results obtained by accident by C. Monney.

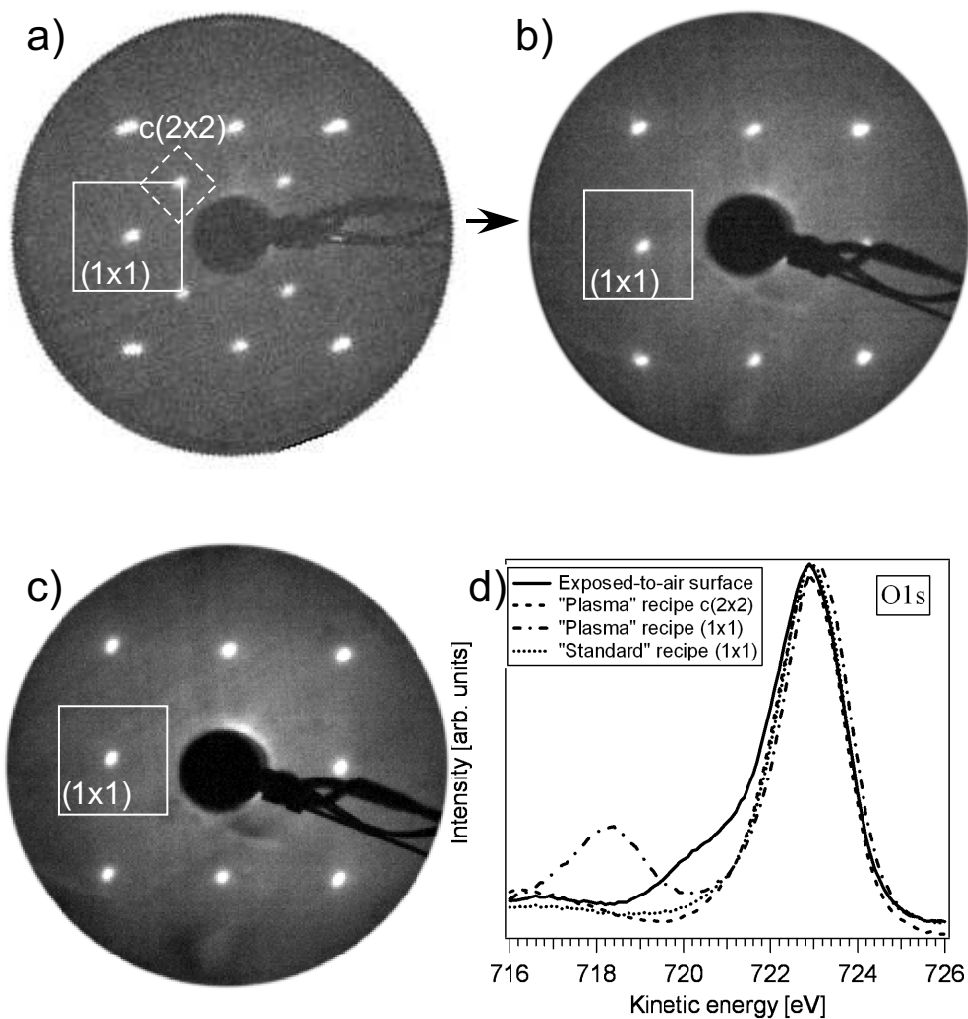


Figure 4.4: Different LEED measurements at 68.7eV. (a)  $c(2 \times 2)$  surface reconstruction after the annealing up to 400°C during 10min and the flash at 1000°C of the Nb-STO sample. (b) The application of an O-plasma on the (a) induces a  $(1 \times 1)$  surface. (c)  $(1 \times 1)$  surface obtained after the standard preparation procedure [4]. (d) O 1s spectra measured on the different surfaces: the exposed-to-air, the  $c(2 \times 2)$  and the  $(1 \times 1)$  after the "plasma" and the "standard" recipes (MgK $\alpha$ ).

(larger kinetic energy) corresponds to the O from the Nb-STO while the shoulder (at smaller kinetic energy) originates from contaminants at the surface.

The three other spectra correspond to the surface of the  $c(2 \times 2)$  reconstruction (dashed line), the  $(1 \times 1)$  surface after the plasma (dashed-dotted line) and the  $(1 \times 1)$  surface after the standard recipe (dotted line). In all cases, the shoulder visible for the raw sample has disappeared, indicating that this kind of surface contaminant has been removed. The XPS measurements corresponding to the  $c(2 \times 2)$  reconstruction and the  $(1 \times 1)$  surface after the standard recipe are very similar even if the atoms at the surface are arranged in a different manner. However, the XPS measurements corresponding apparently to the same  $(1 \times 1)$  surface (Fig. 4.4b and c) are completely different. In the spectrum corresponding to the  $(1 \times 1)$  surface after the plasma recipe, a new peak appears at  $E_{kin} \approx 718\text{eV}$ , contrary to the XPS measurement at the surface obtained using the standard recipe. According to Knipe, this new peak consists of electrically-isolated clusters of OH/H<sub>2</sub>O [11]. We thus suppose that when the  $c(2 \times 2)$  reconstruction is destroyed by the plasma and revealed the  $(1 \times 1)$  surface, an inhomogeneous distribution of ad-atoms at the surface creates the OH/H<sub>2</sub>O clusters while, in the second case, the  $(1 \times 1)$  is directly obtained after the annealing procedure.

These results show that a different LEED pattern does not necessarily imply a different chemical state but also that a similar LEED pattern does not necessarily imply a similar chemical state. Finally, note that the  $(1 \times 1)$  surface reconstruction is the easiest to obtain and also the most stable one. Indeed, it is difficult to completely destroy the  $(1 \times 1)$  without using an Ar<sup>+</sup>-sputtering. This is an important point in order to use the STO as substrate. However, as reported above, the surface chemistry is not inevitably correlated to the surface reconstruction and should be analysed before the growth process to have a complete control of the substrate preparation.

## References for chapter 4

- [1] Q. Jiang, J. Zegenhagen,  $c(6 \times 2)$  and  $c(4 \times 2)$  reconstruction of SrTiO<sub>3</sub>(001), Surf. Sci. **425** (1999) 343–354.
- [2] J. E.T. Andersen, P. J. Moller, Impurity-induced 900°C(2x2) surface reconstruction of SrTiO<sub>3</sub>(100), Appl. Phys. Lett. **56** (1990) 1847.
- [3] A. Gunhold, K. Gömann, L. Beuermann, V. Kempter, G. Borchardt, W. Maus-Friedrichs, Changes in the surface topography and electronic structure of SrTiO<sub>3</sub>(110) single crystals heated under oxidizing and reducing conditions, Surf. Sci. **566-568** (2004) 105–110.
- [4] N. Erdman, L. Marks, SrTiO<sub>3</sub>(001) surface structures under oxidizing conditions, Surf. Sci. **526** (2003) 107–114.
- [5] F. Botton, F. Finocchi, C. Noguera, Stability and electronic structure of the (1x1) SrTiO<sub>3</sub>(110) polar surfaces by first-principles calculations, Phys. Rev. B **68** (2003) 035418.
- [6] T. Higuchi, T. Tasukamoto, N. Sata, M. Ishigame, Y. Tezuka, S. Shin, Electronic structure of *p*-type SrTiO<sub>3</sub> by photoemission spectroscopy, Phys. Rev. B **57** (1998) 6978.

- [7] R. Reihl, J. Bednorz, K. Müller, Y. Jugnet, G. Landgren, J. Morar, Electronic structure of strontium titanate, *Phys. Rev. B* **30** (1984) 803.
- [8] T. Higuchi, S. Nozawa, T. Tosukamoto, Unoccupied electronic structure in the surface state of lightly doped SrTiO<sub>3</sub> by resonant inverse photoemission spectroscopy, *Phy. Rev. B* **66** (2002) 153105.
- [9] V. Henrich, G. Dresselhaus, H. Zeiger, Surface defects and the electronic structure of SrTiO<sub>3</sub> surfaces, *Phys. Rev. B* **17** (1978) 4908.
- [10] R. J. Nelmes and W. F. Kuhs, *Solid State Commun.* **54**, 721 (1985).
- [11] S. Knipe, J. Mycroft, A. Pratt, H. Nesbitt and G. Bancroft, X-ray photoelectron spectroscopic study of water adsorption on iron sulphide minerals, *Geochimica et Cosmochimica Acta* **59** (1995) 1079–1090.

# Chapter 5

## Structural and spectroscopic investigation of $\text{PbTiO}_3$ films

### 5.1 General remarks

Advanced techniques are required to probe ferroelectricity in thin films and nanostructures. Scanning probe characterization based on piezoelectric microscopy has allowed a ferroelectric ground state to be identified down to 40 Å in thin  $\text{Pb}(\text{Zr}_{0.2}\text{Ti}_{0.8})\text{O}_3$  films [1], and x-ray studies on PTO films suggested that 28 Å films are ferroelectric [2]. Ferroelectricity has been identified in polymer films down to 10 Å (two unit cells) using dielectric and pyroelectric response measurements [3]. Ultrahigh vacuum scanning probe characterization based on electrostatic force microscopy was used to study ferroelectricity in  $\text{BaTiO}_3$  nanowires with diameters as small as 10 nm [4]. Using x-ray diffraction, lateral periodicity has been observed in a 12 Å -thick PTO film deposited on an insulating substrate and has been attributed to alternately polarized domains [5,6]. Nevertheless, in all these studies, properties are averaged over the complete ferroelectric structure and no local information on the atomic displacements is obtained.

In contrast, the XPD presents two interesting characteristics: it is naturally surface sensitive, due to an electron escape depth of approximately 20 Å (at the energy used here) ; and atomic displacements within the unit cell can be directly probed. These characteristics allow the non-centro-symmetric and tetragonal nature of the crystal lattice to be directly demonstrated. This turns out to be crucial for studying ultrathin films and for discriminating the behavior of the surface from that of the body of the film.

The chapter is organized as follows. In Section 5.2, a comparison between experiment and theory allows us to identify a preferential ferroelectric polarization state in a 60 Å -thick PTO film. In Section 5.3, we characterize the ferroelectric distortion of a 20Å -thick  $\text{PbTiO}_3$  film and contrast it to the natural atomic relaxation appearing at surface and interface. We also show the tetragonality measurements as a function of film thickness down to 4 Å and that if the film is reduced to one or two unit cells, both non-centro-symmetry and tetragonality are governed by surface effects. In Section 5.4, we investigate the evolution of the photoelectron kinetic energy in  $\text{PbTiO}_3$  thin films as a function of thickness together with the film tetragonality.

We then change the PTO film dielectric environment by modifying the substrate ( $\text{La}_{0.67}\text{Sr}_{0.33}\text{MnO}_3$  or  $\text{SrRuO}_3$ ), the surface using a plasma, or even both studying briefly the PTO in a superlattice configuration, as seen in Section 5.5. And finally, in Section 5.6, MSC calculations coupled to an R-factor analysis have been performed to check whether the XPD measurements are sensitive to a  $c(2\times 2)$  antiferrodistortive reconstruction.

### References for section 5.1

- [1] T. Tybell, C. H. Ahn, and J.-M. Triscone, *Appl. Phys. Lett.* **75**, 856 (1999).
- [2] C. Lichtensteiger, J.-M. Triscone, J. Junquera and P. Ghosez, *Phys. Rev. Lett.* **94**, 047603 (2005).
- [3] A. Bune, V.M. Fridkin, S. Ducharme, L.M. Blinov, S.P. Palto, A.V. Sorokin, S.G. Yudin and A. Zlatkin, *Nature (London)* **391**, 874 (1998).
- [4] W. S. Yun, J. J. Urban, Q. Gu, and H. Park, *Nano Letters* **2**, 447 (2002).
- [5] S. K. Streiffer, J. A. Eastman, D. D. Fong, C. Thompson, A. Munkholm, M. V. Ramana Murty, O. Auciello, G.R. Bai and G.B. Stephenson, *Phys. Rev. Lett.* **89**, 067601 (2002).
- [6] D. D. Fong, G. B. Stephenson, S. K. Streiffer, J. A. Eastman, O. Auciello, P. H. Fuoss and C. Thompson, *Science* **304**, 1650 (2004).

## 5.2 X-ray photoelectron diffraction study of ultrathin PbTiO<sub>3</sub> films

L. Despont,<sup>1</sup> C. Lichtensteiger,<sup>2</sup> F. Clerc,<sup>1</sup> M. G. Garnier,<sup>1</sup> F. J. Garcia de Abajo,<sup>3</sup> M. A. Van Hove,<sup>4</sup> J.-M. Triscone,<sup>2</sup> P. Aebi,<sup>1</sup>

<sup>1</sup> *Institut de Physique, Université de Neuchâtel, Rue A.-L. Breguet 1, CH-2000 Neuchâtel, Switzerland*

<sup>2</sup> *DPMC, Université de Genève, 24 Quai Ernest-Ansermet, CH-1211 Genève, Switzerland*

<sup>3</sup> *Centro Mixto CSIC-UPV/EHU, 20080 San Sebastián, Spain*

<sup>4</sup> *Materials Sciences Division and Advanced Light Source, Lawrence Berkeley National Laboratory, Berkeley, CA 94720, and Department of Physics, University of California, Davis, CA 95616.*

Published in Eur. Phys. J. B **49**, 141-146 (2006)

Full hemispherical X-ray photoelectron diffraction (XPD) experiments have been performed to investigate at the atomic level ultrathin epitaxial c-axis oriented PbTiO<sub>3</sub> (PTO) films grown on Nb-doped SrTiO<sub>3</sub> substrates. Comparison between experiment and theory allows us to identify a preferential ferroelectric polarization state in a 60 Å -thick PTO film. Multiple scattering theory based on a cluster-model (Phys. Rev. B **63**, 075404 (2001)) is used to simulate the experiments.

### 5.2.1 Introduction

Ferroelectric oxides display a variety of interesting physical properties including piezoelectricity, pyroelectricity, and a non-volatile switchable electric polarization. This functionality makes them attractive candidates for numerous applications such as actuators, high frequency filters, infrared detectors, or high density non-volatile memories [1–3].

Recently, progress on the material side and new techniques have allowed ferroelectricity to be studied at nanoscale [4]. In particular, scanning probe microscopy has emerged as one interesting technique allowing local manipulations of domain structure in thin films and studies of ferroelectricity on nanometer scales [3, 5, 6]. Combining this technique with epitaxial Pb(Zr<sub>0.2</sub>Ti<sub>0.8</sub>)O<sub>3</sub> thin films, ferroelectricity was demonstrated down to 40 Å [5]. X-ray synchrotron was also used to study epitaxial PbTiO<sub>3</sub> thin films grown on insulating SrTiO<sub>3</sub> substrates and revealed periodic 180° stripe domains in films from 420 down to 12 Å thickness [7, 8]. Very recently, a synchrotron x-ray micro-diffraction technique was developed to probe domain growth and switching in ferroelectric devices with submicrometer spatial resolution [9].

All the techniques described above are probing an average (throughout the depth of the films) response of the material. To get a more detailed microscopic information on ferroelectricity and to be able to directly probe the ferroelectric polar distortion, an atomic scale sensitive technique is needed. In this paper we show that X-ray photoelectron diffraction (XPD), already known as an important tool for crystal structure analysis might be a possible route

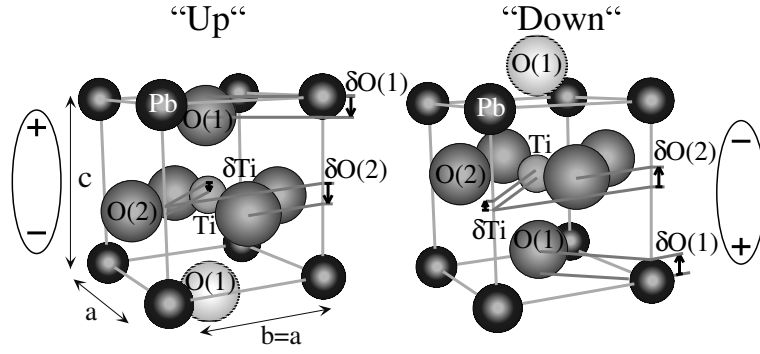


Figure 5.1: Tetragonal PTO unit cell with the ferroelectric bulk lattice parameters  $a=b=3.902$  Å and  $c=4.156$  Å. The displacements, in fractional units, from cubic phase sites are  $\delta\text{Ti}=0.0377$  for titanium,  $\delta\text{O}(1)=0.1118$  for the first oxygen type (alternating along the  $c$  axis with the titanium) and  $\delta\text{O}(2)=0.1174$  for the second oxygen type (in the vertical Pb plane) [11]. The electric dipoles resulting from the ionic displacements are schematically shown.

to address the problem of ferroelectricity in ultrathin films. In particular, this technique is applied to  $\text{PbTiO}_3$  (PTO), a ferroelectric perovskite with a tetragonal structure below the critical temperature  $T_c$ , characterized by two oppositely polarized ground states along the (polar) tetragonal  $c$ -axis [10–12]. These two “up” and “down” equivalent and electrically switchable states are characterized by the corresponding displacements of the Ti and O atoms in the unit cell delimited with Pb atoms, see Fig. 5.1. For the data analysis and simulation of the experiment, the cluster-model approach of the EDAC code [13] is used.

## 5.2.2 Experimental and computational details

Here we study epitaxial  $c$ -axis oriented  $\text{PbTiO}_3$  perovskite films grown using off-axis magnetron sputtering onto metallic (001)  $\text{Nb-SrTiO}_3$  substrates. Topographic measurements using atomic force microscopy showed that these films are essentially atomically smooth. X-ray diffraction measurements allowed us to precisely determine the thickness of the films and the  $c$ -axis lattice parameter value, and to confirm epitaxial growth [14, 15].

The samples were exposed to air during transfer from the growth chamber to the XPD experiment. No surface cleaning procedure was applied, and the measurements were performed at room temperature. Despite the presence of surface contamination, we obtain well-defined diffraction patterns. Via X-ray photoelectron spectroscopy (XPS), Fig. 5.2, we detect small amounts of C. In addition, the O 1s emission line is doubled due to oxygen atoms in chemically different environments (see inset of Fig. 5.2). One emission line has its origin from O within the PTO and the other from contaminants at the surface. The distinction is possible since the XPD pattern of the O 1s emission from the contamination layer, as well as from the C 1s emission does not show anisotropy whereas it does for O 1s emission from oxygen within the PTO. This also demonstrates that the contamination layer is disordered. The shift between both O lines is roughly 3 eV and allows a clear separation of the PTO oxygen from the one at

the surface. The photoelectrons emitted from O contained in the substrate can not be detected as the thickness of the measured film, 60 Å is larger than their inelastic mean free path. that the polarization determination by selecting the O emission signal is limited to film thicknesses down to approximately 20 Å due to the presence of O in the substrate (also for the Ti emission). This limitation is also a function of the photoelectron kinetic energy which defines the distance after which the signal becomes negligibly small depending on the inelastic mean free path.

The XPD measurements were done in a modified Vacuum Generators ESCALAB Mk II X-ray photoelectron spectrometer equipped with a fixed hemispherical electron energy analyzer, and a three-channeltron detection system, operated with a base pressure in the lower  $10^{-11}$  mbar region. X-ray photons are provided with a  $MgK\alpha$  ( $h\nu=1253.6$  eV) and  $SiK\alpha$  ( $h\nu=1740$  eV) twin anode. The samples are fixed on a computer-controlled two-axis goniometer capable of scanning the emission angle over the full hemisphere above the surface [16, 17].

A  $2\pi$  emission-angle intensity scan of a given X-ray photoemission line permits the determination of the local geometry around the selected atom [18–21]. The angular dependence of the collected electron intensity originates from the interference of the directly emitted photoelectron wave and the scattered electron waves. XPD being sensitive at an atomic scale, [22, 23] it can be used to analyze crystal structures down to the monolayer and, in particular, to study ultrathin films of PTO. The knowledge of the crystal structure, then, allows us to discriminate between paraelectric and ferroelectric states.

The analysis of diffraction patterns is facilitated due to the so-called “forward focusing” effect occurring if the photoemitted electron has a kinetic energy above approximately 0.5 keV. Single scattering model calculations predict strong enhancement of the emission intensity in direction of near neighbours and more generally along densely packed rows of atoms which correspond to low-index crystallographic directions [24]. When compared to experimental results, the “forward focusing” intensity is overemphasized in single scattering calculations. This implies the necessity to use multiple scattering calculations(MSC). Furthermore, in the above-mentioned energy range the photoelectron inelastic mean free path ( $\lambda$ ) is large. Thus the number of elastic scattering events is also large and therefore the use of MSC calculations becomes essential. In fact, scattering at the first few atoms along a row of atoms focuses the emission in the emitter-scatterer direction. Then, subsequent atoms tend to defocus the signal [25]. The defocusing is linked to the development of the conventional Kikuchi bands which become more intense when the forward-scattering peak intensity diminishes [25, 26]. Therefore, MSC provides a solution to increase the accuracy in peak and band intensities as well as in structural details.

To simulate the XPD experiment, we use the cluster-model approach of the EDAC code [13] based on the muffin-tin potential approximation [27]. We employ the Haydock recursion method to calculate an iterative solution of the MSC series [13]. The chosen atomic positions in the clusters are taken from the bulk structure in Ref. [11]. The computation time needed to determine the scattered wave function is proportional to  $nN^2(l_{max} + 1)^3$ , where  $n$  is the scattering order,  $N$  the number of atoms used in the cluster and  $l_{max}$  the maximum angular momentum quantum number. This last parameter permits an approximation of the outgoing photoelectron wave function using a combination of  $l_{max}$  spherical harmonics. The number of spherical harmonics is approximately given by  $l_{max} \approx kr_{mt}$  [27] where  $k$  is the photoelectron

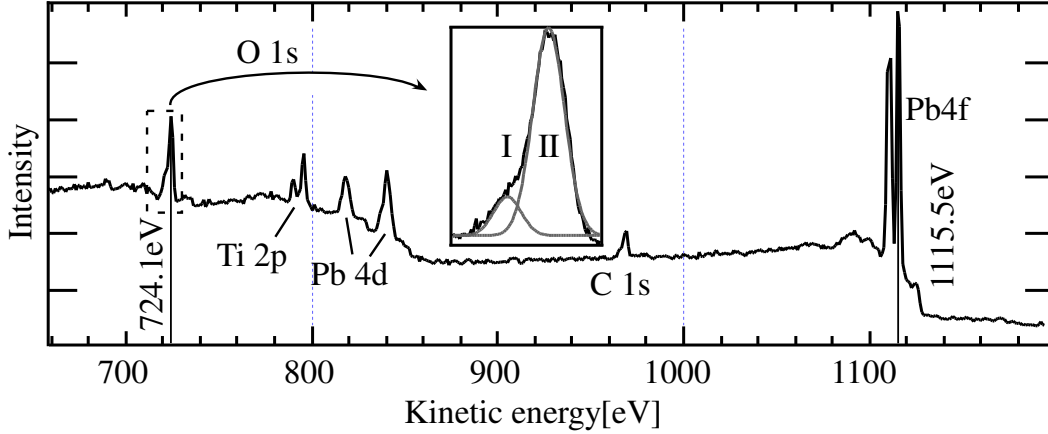


Figure 5.2: (a) XPS spectrum for PTO (60 Å thick film), obtained with  $\text{MgK}\alpha$  radiation. O 1s (I) is the emission from the contamination layer while O 1s (II) has its origin within the PTO.

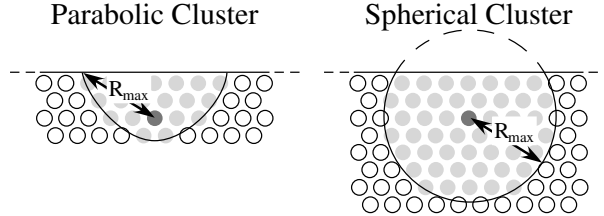


Figure 5.3: Two different cluster shapes with the scattering volumes defined by  $R_{max}$ . The light and dark gray disks correspond to scatterers and to the emitter, respectively.

momentum and  $r_{mt}$  the muffin-tin radius. By assuming an average nearest-neighbor distance and selecting a photoelectron kinetic energy  $E_{kin}$ , we can roughly deduce the  $l_{max}$  parameter.

The number  $N$  of scattering atoms in the cluster is defined using the parameter  $R_{max}$ . In Fig. 5.3 we show how  $R_{max}$  defines the scattering volume using the emitter, in the first case, as the focus of a parabola or, in the second case, as a sphere centre. Sufficiently large  $R_{max}$  have been used in the calculations to insure the convergence on the cluster size. To increase the contribution of scattering on atoms between the emitters and the surface, the parabolic shape is selected in the present study. In our case, the scattering volume contains approximately 150-250 atoms ( $R_{max}=16 \text{ \AA}-22 \text{ \AA}$ ). We can deduce the electron inelastic mean free path  $\lambda$  by taking into account the universal relationship between energy and inelastic mean free path [28, 29]. For each layer located within  $\lambda$  from the surface we take one of every inequivalent atom as emitter. For PTO, with  $\lambda=10 \text{ \AA}$  for O 1s ( $E_{kin}=724.1 \text{ eV}$ ,  $\text{MgK}\alpha$ ), seven (for the “up” state) and eight (“down” state) emitters are chosen over three unit cells while, with  $\lambda=17 \text{ \AA}$  for Pb  $4f_{7/2}$  photoelectrons ( $E_{kin}=1115.5 \text{ eV}$ ,  $\text{MgK}\alpha$ ), five emitters (for “up” and “down” states) are selected over five unit cells.

The introduction of an inner potential  $V_o$  permits to consider refraction effects of the photoelectron wave at the surface-potential step. A value of 10.5 eV is chosen [30]. Thermal

vibrations are introduced by means of a Debye temperature ( $\theta_D$ ), and the  $\theta_D$  have been introduced separately for each type of atom. We have taken values of  $\theta_D=105$  K, 420 K and 80 K for Pb, Ti and O atoms respectively [31]. The calculations were performed for a temperature  $T=300$  K.

Two different surface terminations are possible, but using XPD it is not possible to extract the surface termination in the case of PTO films. The reason is that in this system the contribution due to scattering of electrons from deeper layers at the top most layer is negligible compared to the direct emission from deeper layers. This behaviour originates from the small distance between the strong-scatterer layers (containing Pb). However, the calculations are performed with a Pb-O terminated surface. Indeed, Meyer et al. [32] suggest that only the Pb-O surface termination is thermodynamically stable in PTO.

### 5.2.3 Results and Discussion

Analysis of the XPS spectrum presented in Fig. 5.2 shows that the most intense signals come from the core levels of Pb and O. The signal for Ti emission is smaller. In addition, for both, the "up" and "down"-states, the displacement of the Pb atoms relative to the Ti atoms is smaller than the displacement of Pb atoms relative to the O atoms [11]. This signifies that the difference between the "up"- and the "down"-state "forward focusing" peak positions is smaller for the Ti emission than for the O emission. Moreover the polarization signature is located in the (110)-plane if Ti emitters are selected. This means that the Ti-Pb distance is larger than the O-Pb distance (in the (100)-plane), suggesting a smaller "forward focusing" peak intensity (exponential signal decrease along the photoelectron path due to the inelastic mean free path). Therefore, in the following we chose to analyze in details the Pb and O XPD patterns.

In Fig. 5.4a the major low-index directions and crystal planes of the perovskite structure are plotted in stereographic projection. Calculated diffractograms for the Pb  $4f_{7/2}$  core level are displayed in Figs. 5.4b and 5.4c for the "up" and the "down" state cases, respectively, according to the structure of Ref. [11]. The experimental diffractogram for a 60 Å thick film is displayed in Fig. 5.4d. All the diffractograms are plotted in stereographic projection. A background has been subtracted to all experimental data in the following manner: the total intensity was recorded at the kinetic energy corresponding to the maximum of the relevant peak ( $I_{peak}$ ) and at its high-energy footpoint ( $I_{high}$ ). The background-corrected intensity was then calculated by subtracting  $I_{high}$  from  $I_{peak}$ . The patterns have been azimuthally averaged exploiting the four-fold symmetry of the PTO and normalized to a smooth polar angle dependent background. As the calculations do not contain the secondary electron background, only the final normalization has been applied to the simulations.

The main "forward focusing" peaks, labelled  $A_1$  ( $\langle 111 \rangle$  directions),  $B_1$  ( $\langle 101 \rangle$  directions) and  $C_1$  (normal emission,  $[001]$ ) are at the same positions for both the simulations and the experiment, with similar intensities and widths. These peaks correspond to scattering by Pb atoms. The intensity modulations  $D_1$  (between  $[001]$  and  $\langle 101 \rangle$  directions),  $E_1$  (between  $[001]$  and  $\langle 111 \rangle$  directions) and  $F_1$  (between  $\langle 101 \rangle$  and  $\langle 100 \rangle$  directions) have also the same behaviour for "up", "down" and the experiment. The intensity enhancements,  $G_1$ , on the  $\{101\}$  Kikuchi bands, near  $\langle 121 \rangle$  directions are also comparable for the three different

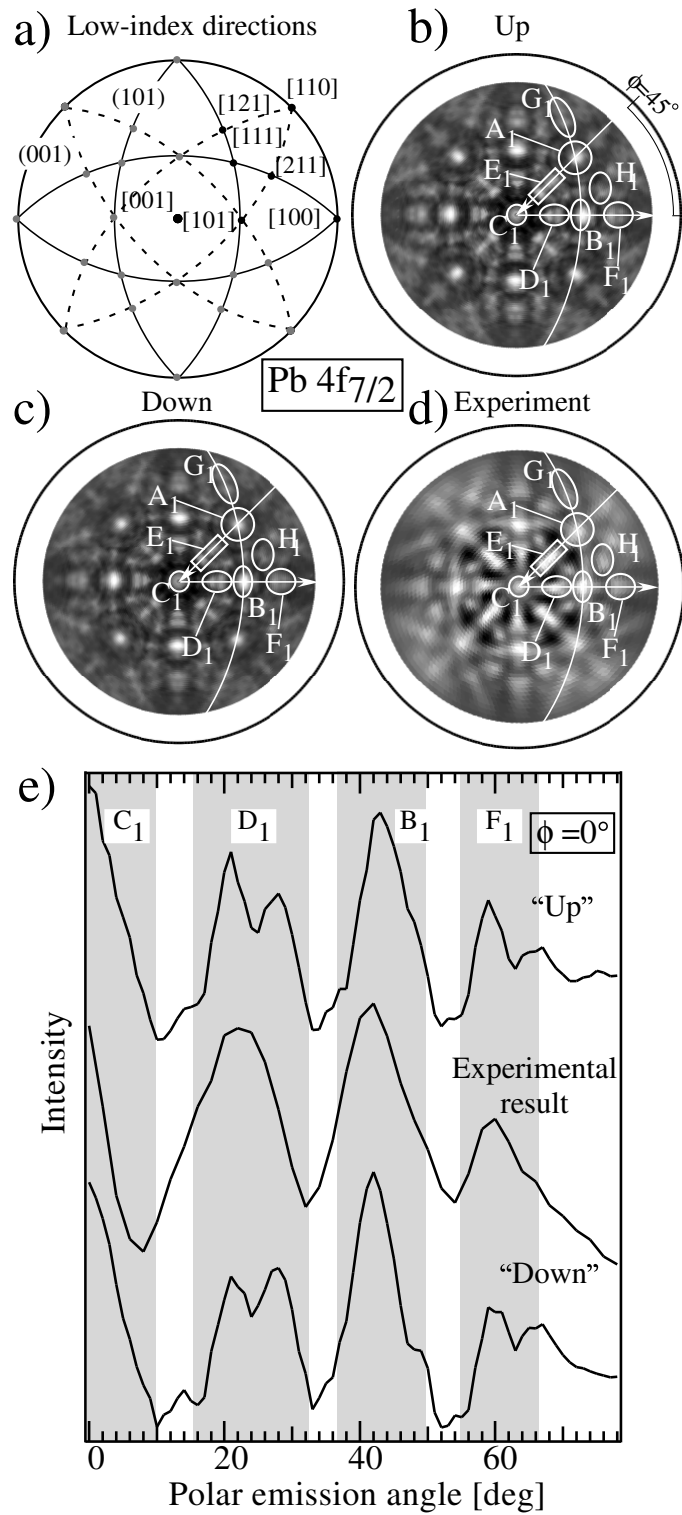


Figure 5.4:  $\text{MgK}\alpha$  excited  $\text{Pb } 4f_{7/2}$  photoelectrons at  $E_{kin}=1115.5$  eV. (a) Stereographic projection of major directions (dots) and low-index planes (continuous lines correspond to dominant high-density planes  $\{101\}$ , dashed lines correspond to minor high-density planes  $\{\bar{1}11\}$ ). Simulated diffractograms for PTO (b) "up" and (c) "down" cases. (d) Experimental result for a c-axis oriented PTO 60 Å-thin film. (e) Polar cuts at  $\phi = 0^\circ$  for the two simulated states and the experimental case.

diffractograms. This is also true for the  $H_1$  modulations. Polar cuts at  $\phi = 0^\circ$  are performed from the normal emission direction up to  $\theta = 78^\circ$  polar angle, in Fig. 5.4e. The differences between both simulations are not large enough to distinguish between both polarization states.

Therefore, at this point, it is not possible to differentiate between the two different polarization states. The diffractograms are completely dominated by the scattering on the heavy Pb atoms. This is due to the larger Pb scattering cross section compared to Ti or O. As Pb is the main scatterer in this material, the attention has to be focused on the Pb atom displacement relative to others kinds of atoms. By selecting O atoms as emitters, therefore, we change the reference system from which the photoelectrons are ejected. Instead of looking at the displacement of the light atom sublattice relative to Pb, we expect to see the corresponding shifts of Ti and Pb atoms relative to O atoms.

The results displayed in Fig. 5.5 show diffractograms obtained with the O 1s core level ( $E_{kin}=724.1$  eV). In Fig. 5.5a we see the major low-index crystallographic directions and dominant high-density planes. In Figs. 5.5b and 5.5c, we show the calculated diffractograms for PTO “up” and “down” state structures. Figure 5.5d displays the experimental result for the 60 Å thin film. To bring into evidence the region of large differences between the two different structures, polar cuts are presented at  $\phi = 0^\circ$  starting at normal emission [001] up to  $\theta = 78^\circ$  polar angle, plotted together with the experimental result along the same direction. The main difference comes from the scattering of O 1s photoelectrons on nearest neighbor Pb atoms (label A in Fig. 5.5), as expected from the previous result obtained with Pb emission. Near  $\langle 101 \rangle$  directions we observe easily the corresponding principal “forward focusing” direction which appears to be the same in Figs. 5.5b and 5.5d, namely for the “up” state structure.

In the Pb emission case, the dominant Kikuchi bands are the  $\{101\}$  and the main “forward focusing” peaks (label  $A_1$  and  $B_1$ ) are aligned on these bands, while for O emission the dominant Kikuchi bands are the  $\{\bar{1}11\}$  and the main peaks (label A) are shifted from the aligned position. This behaviour indicates that, in the first case, the dominant high-density planes are constituted by Pb atoms, and trivially, the peaks representing the scattering by Pb are along the bands. In the O emitter case, the diffraction on the crystal planes formed by O atoms is dominant. Then the main “forward focusing”, O-Pb directions, are not aligned anymore with the bands. This behaviour is well observed where, for the “up” structure simulation and the experimental result (Figs. 5.5b and d), the peaks (label A) are inside the Kikuchi bands delimited zone, while they are outside of the same region for the “down” structure simulation (Fig. 5.5c). The information extracted from this region of the diffractogram is strongly influenced by the small distance between emitters and scatterers.

Furthermore we observe intensity enhancements (B) on  $\{\bar{1}11\}$  Kikuchi bands. The length and the width of this modulation agrees well between the experiment and the “up” state calculation. Similar features (C) appear close to  $\langle 211 \rangle$  directions, but differences between “up” and “down” in this case are not significant enough to identify the different states. The center peaks (label D) originate from the scattering by O atoms, just above the selected emitters. As this configuration is exactly the same for “up” and “down” states, no information about the structure differences is revealed. The origin of the peak (label E), between [001] and the  $\langle 101 \rangle$  directions, could not be extracted in a direct way and thus is linked to multiple scattering effects. As displayed in Fig. 5.5e, this peak is not exactly reproduced in the “up” structure case but

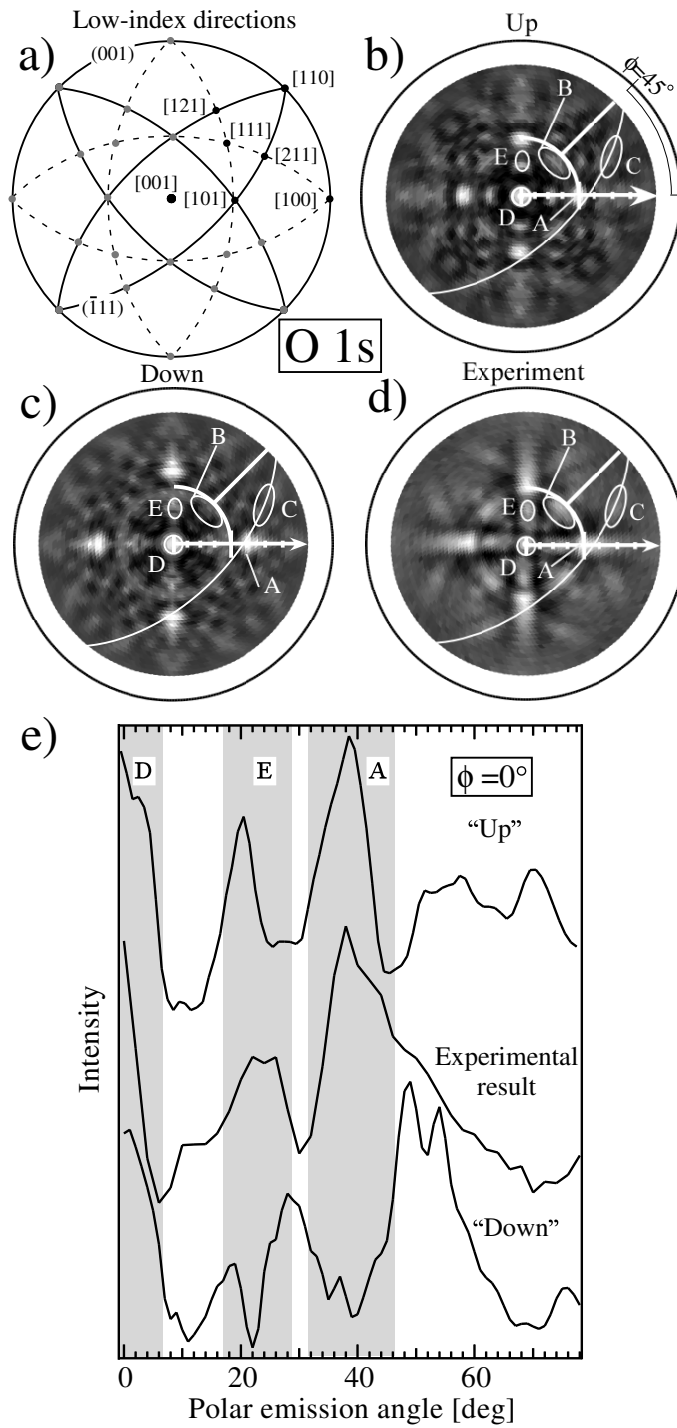


Figure 5.5:  $\text{MgK}\alpha$  excited O 1s photoelectrons at  $E_{kin}=724.1$  eV. (a) Stereographic projection of major directions (dots) and low-index planes (continuous lines correspond to dominant high-density planes  $\{111\}$ , dashed lines correspond to minor high-density planes  $\{101\}$ ). (b) Simulated diffractogram for PTO “up” state plotted in stereographic projection. (c) The same calculation as in (b) but for the “down” state. (d) Experimental result for a c-axis oriented PTO 60 Å thin film. (e) Polar cuts at  $\phi = 0^\circ$  for the two simulated states and the experimental case.

shows more similarity with the experimental result than in the “down” case, where there is a lack of intensity in the concerned region.

As seen from Fig. 5.5, the agreement of the calculation with experiment is good but not perfect. The reason may be found in the fact that we use structural parameters taken from the bulk [11]. In reality, surface relaxation may take place and a detailed optimization and a R-factor analysis of structural parameters will be required. Furthermore, PTO contains three highly different atomic types and the exact relative scattering strength and vibration parameters are difficult to determine. Correct relative scattering strengths are necessary to obtain accordance on relative intensities of interference features.

The intention here is to establish the basic principle for the use of XPD to investigate ultrathin ferroelectric films. We are able to make a clear distinction between the “up” and “down” state for a bulk-terminated surface, and subsequently we are able to characterize the sample as “up” polarized, according to angular positions, e.g. features A-E in Fig. 5.5. In particular, the O-Pb first order near neighbour “forward focusing” direction (feature A) is practically given by geometrical consideration. Since Pb is the dominant scatterer (cf. Fig. 5.4, results for the Pb emission), the analysis concerning the large difference coming from peak A is therefore giving very robust information.

## 5.2.4 Conclusion

Calculations taking into account multiple scattering prove to be necessary to accurately simulate XPD diffractograms. Diffraction patterns are dominated by the “forward focusing” peaks along low-index crystallographic directions. Kikuchi bands appear with the same width and intensity as in the experiment. Regarding PTO, differences between “up” and “down” simulations are sufficiently large to be distinguishable when selecting the O 1s core level. Globally the agreement between experiment and calculation is good and allows us to identify our 60 Å film as “up” polarized.

## Acknowledgements

Skillful technical assistance was provided by the Neuchâtel workshop and electric engineering team. This project has been supported by the Swiss National Science Foundation through the National Center of Competence in Research “Materials with Novel Electronic Properties-MaNEP”, and in part by the Office of Science, Materials Sciences Division, of the U.S. Department of Energy under Contract No. DE-AC03-76SF00098.

## References for section 5.2

- [1] T. Tybell, C. H. Ahn, J.-M. Triscone, *Appl. Phys. Lett.* **72** (1998) 1454–1456.
- [2] J. F. Scott, C. A. P. de Araujo, *Science* **246** (1989) 1400.
- [3] P. Paruch, T. Tybell, J.-M. Triscone, *Appl. Phys. Lett.* **79** (2001) 530.

- [4] C. H. Ahn, K. Rabe, J.-M. Triscone, *Science* **303** (2004) 488.
- [5] T. Tybell, C. H. Ahn, J.-M. Triscone, *Appl. Phys. Lett.* **75** (1999) 856–858.
- [6] P. Paruch, T. Giamarchi, J.-M. Triscone, *Phys. Rev. Lett.* **94** (2005) 197601.
- [7] S.K. Streiffer, J.A. Eastman, D.D. Fong, C. Thompson, A. Munkholm, M.V. Ramana Murty, O. Auciello, G.R. Bai, G.B. Stephenson, *Phys. Rev. Lett.* **89** (2002) 067601.
- [8] Dillon D. Fong, G. Brian Stephenson, Stephen K. Streiffer, Jeffrey A. Eastman, Orlando Auciello, Paul H. Fuoss, Carol Thompson, *Science* **304** (2004) 1650–1653.
- [9] Dal-Hyun D, Paul G. Evans, Eric D. Isaacs, Dong Min Kim, Chang Beom Eom, Eric M. Dufresne, *Nature Materials* **3** (2004) 365–369.
- [10] T. Tybell, P. Paruch, T. Giamarchi, J.-M. Triscone, *Phys. Rev. Lett.* **89** (2002) 097601–1–4.
- [11] R. J. Nelmes, W. F. Kuhs, *Solid State Commun.* **54** (1985) 721–723.
- [12] F. Jona, G. Shirane, *Ferroelectrics Crystals* (Dover Publication, New York 1997).
- [13] F. J. Garcia de Abajo, M. A. Van Hove, C. S. Fadley, *Phys. Rev. B* **63** (2001) 075404–1–16.
- [14] C. Lichtensteiger, J.-M. Triscone, J. Junquera, P. Ghosez, *Phys. Rev. Lett.* **94** (2005) 047603.
- [15] C. Lichtensteiger, J.-M. Triscone, *Int. Ferroelectrics* **61** (2004) 143–148.
- [16] J. Osterwalder, T. Greber, A. Stuck, L. Schlapbach, *Phys. Rev. B* **44** (1991) 13764–13767.
- [17] D. Naumović, A. Stuck, T. Greber, J. Osterwalder, L. Schlapbach, *Phys. Rev. B* **47** (1993) 7462–7479.
- [18] R. Fasel, P. Aebi, J. Osterwalder, L. Schlapbach, *Surf. Sci.* **331–333** (1995) 80–87.
- [19] J. Osterwalder, P. Aebi, R. Fasel, D. Naumović, P. Schwaller, T. Kreutz, L. Schlapbach, T. Abukawa, S. Kono, *Surf. Sci.* **331–333** (1995) 1002–1014.
- [20] D. Naumović, J. Osterwalder, A. Stuck, P. Aebi, L. Schlapbach, *Surf. Sci.* **287–288** (1993) 950–954.
- [21] T. Greber, J. Osterwalder, D. Naumović, A. Stuck, S. Hufner, L. Schlapbach, *Phys. Rev. Lett.* **69** (1992) 1947–1950.
- [22] R. Fasel, P. Aebi, R. G. Agostino, D. Naumović, J. Osterwalder, A. Santaniello, L. Schlapbach, *Phys. Rev. Lett.* **76** (1996) 4733–4736.
- [23] P. Aebi, R. Fasel, D. Naumović, J. Hayoz, T. Pillo, M. Bovet, R. G. Agostino, L. Patthey, L. Schlapbach, F. P. Gil, H. Berger, T. Kreutz, J. Osterwalder, *Surf. Sci.* **402** (1998) 614–622.

- [24] C. S. Fadley, *Synchrotron Radiation Research: Advances in Surface Science* (Plenum, New York 1990).
- [25] W. F. Egelhoff Jr., *Critical Reviews in Solid State and Materials Sciences* **16** (1990) 213–235.
- [26] H. A. Aebischer, T. Greber, J. Osterwalder, A. P. Kaduwela, D. J. Friedman, G. S. Herman, C. S. Fadley, *Surf. Sci.* **239** (1990) 261–264.
- [27] J. B. Pendry, *Low Energy Electron Diffraction* (Academic Press, London 1974).
- [28] R. E. Ballard, *J. Electron Spectrosc. Relat. Phenom.* **25** (1982) 75–78.
- [29] M. P. Seah, W. A. Dench, *Surf. Interface Anal.* **1** (1979) 2–11.
- [30] At high electron kinetic energies, the effect of refraction (or  $V_o$ ) is not very important.
- [31] From the Integral Scientist Periodic Table of the Elements (ISPT) available on <http://www.qivx.com>
- [32] B. Meyer, J. Padilla, D. Vanderbilt, *Faraday Discuss.* **114** (1999) 395–405.



## 5.3 Direct evidence for ferroelectric polar distortion in ultrathin lead titanate perovskite films

L. Despont,<sup>1</sup> C. Lichtensteiger,<sup>2</sup> C. Koitzsch,<sup>1</sup> F. Clerc,<sup>1</sup> M. G. Garnier,<sup>1</sup> E. Bousquet,<sup>3</sup> Ph. Ghosez,<sup>3</sup> F. J. Garcia de Abajo,<sup>4</sup> J.-M. Triscone,<sup>2</sup> P. Aebi,<sup>1</sup>

<sup>1</sup> *Institut de Physique, Université de Neuchâtel, Rue A.-L. Breguet 1, CH-2000 Neuchâtel, Switzerland*

<sup>2</sup> *DPMC, Université de Genève, 24 Quai Ernest-Ansermet, CH-1211 Genève, Switzerland*

<sup>3</sup> *Département de Physique, Université de Liège, B-4000 Sart-Tilman, Belgium*

<sup>4</sup> *Centro Mixto CSIC-UPV/EHU, 20080 San Sebastián, Spain*

Published in Phys. Rev. B **73**, 094110 (2006)

X-ray photoelectron diffraction is used to directly probe the intra-cell polar atomic distortion and tetragonality associated with ferroelectricity in ultrathin epitaxial  $\text{PbTiO}_3$  films. Our measurements, combined with *ab-initio* calculations, unambiguously demonstrate non-centro-symmetry in films a few unit cells thick, imply that films as thin as 3 unit cells still preserve a ferroelectric polar distortion, and also show that there is no thick paraelectric dead layer at the surface.

### 5.3.1 Introduction

Theoretical developments and novel experiments in the area of ferroelectrics have rapidly evolved over the last ten years, allowing further progress in the understanding of this remarkable phenomenon. In particular, “nanoscale” ferroelectrics have attracted considerable attention [1–5]. The question of the existence of a critical thickness, in other words whether or not ferroelectricity can be maintained at reduced dimensions, is amongst the most exciting topics of the field today, with very active experimental [6–9] and theoretical efforts [10–13].

Probing ferroelectricity in thin films and nanostructures is a difficult task, which requires advanced techniques. Among these, scanning probe characterization based on piezoelectric microscopy has allowed a ferroelectric ground state to be identified down to 40 Å in thin  $\text{Pb}(\text{Zr}_{0.2}\text{Ti}_{0.8})\text{O}_3$  films [6], and x-ray studies on  $\text{PbTiO}_3$  films suggested that 28 Å films are ferroelectric [9]. Dielectric and pyroelectric response measurements have allowed ferroelectricity to be identified in polymer films down to 10 Å (two unit cells) [14]. More recently, ultrahigh vacuum scanning probe characterization based on electrostatic force microscopy was used to study ferroelectricity in barium titanate nanowires with diameters as small as 10 nm [15]. On insulating substrates, lateral periodicity was observed via x-ray diffraction in thin  $\text{PbTiO}_3$  films down to 12 Å and attributed to alternately polarized domains [7,8]. In all these studies, however, properties *averaged* over the complete ferroelectric structure were measured and no *local* information on the atomic displacements was obtained.

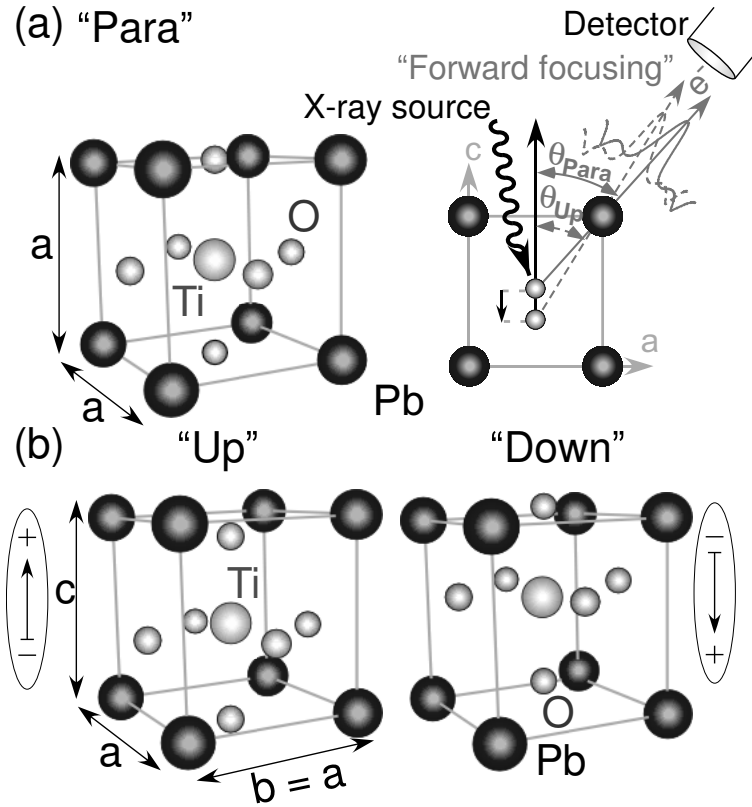


Figure 5.6: (Color online) (a) Schematic of the measurement setup. Core electrons have well-defined binding energies, and their photoemission spectra exhibit characteristic emission lines. By selecting a particular emission line, photoelectrons from a given emitter can be chosen, thus probing the local real-space environment of the emitter. The interpretation is facilitated by forward focusing of electron flux along the emitter-scatterer direction. The difference between two “forward focusing” peak positions is directly related to a modified emitter-scatterer direction, illustrated here by the “para”- toward “up”-state- O shift. Above  $490^{\circ}\text{C}$ , bulk  $\text{PbTiO}_3$  has a cubic unit cell, with the O and Ti atoms centered in the Pb cage (“para”-state). (b) Below  $490^{\circ}\text{C}$ , bulk  $\text{PbTiO}_3$  has a tetragonal unit cell: two equivalent ferroelectric configurations corresponding to two opposite polarizations, “up”-state and “down”-state. The displacements (in fractional units) from cubic phase sites are 0.111 and 0.037 for O and Ti, respectively [16].

In contrast, the photoemission based photoelectron diffraction (XPD) used in our study presents two interesting characteristics: it is naturally surface sensitive, due to an electron escape depth of approximately  $20 \text{ \AA}$  (at the energy used here) ; and atomic displacements within the unit cell can be directly probed, allowing the non-centro-symmetric and tetragonal nature of the crystal lattice to be directly demonstrated. This turns out to be crucial for studying ultrathin films, and for discriminating the behavior of the surface from that of the body of the film.

The paper is organized as follows. In Section II, we characterize the ferroelectric distortion of  $\text{PbTiO}_3$  and contrast it to the natural atomic relaxation appearing at surface and interface.

In Sec. III A, we discuss aspects of the measurement methods while, in Sec. III B we show the non-centro-symmetry of a 20 Å thick film using XPD. The Sec. III C is dedicated to the tetragonality measurements as a function of film thickness with XPD using Pb as emitter, down to 4 Å (one unit cell). We summarize and conclude in Sec. IV.

### 5.3.2 Ferroelectric distortion versus surface relaxation

The studies were carried out on *c*-axis oriented perovskite  $\text{PbTiO}_3$  ultrathin films epitaxially grown on conducting  $\text{Nb-SrTiO}_3$  substrates. Above 490°C, bulk  $\text{PbTiO}_3$  is a paraelectric insulator and a simple cubic perovskite structure with a lattice parameter of 3.96 Å (“para”-state, see Fig. 5.6a). In this structure, the Ti and O atoms are in perfectly centro-symmetric positions with respect to the surrounding Pb cage. At lower temperature, the material becomes tetragonal and ferroelectric with *a*- and *c*-axis parameters of 3.90 Å and 4.17 Å, respectively [16,17], as illustrated in Fig. 5.6b. The ferroelectric phase is characterized by a non-centro-symmetric structure where the O and Ti atoms are unequally shifted with respect to Pb. In a unit cell with the polar *c*-axis along the *z*-direction, O and Ti move either upwards or downwards (with a larger O displacement) resulting respectively in a “down”- and “up”-polarized state, as drawn in Fig. 5.6b.

In the surface region (five top unit cells) that is probed by the XPD technique, the evidence of such a polar atomic distortion could be the signature of a ferroelectric “up”- or “down”-state but may also arise from the natural atomic relaxation at the film surface and interface already present in the paraelectric phase. A proper interpretation of our data therefore requires independent quantification of both effects. To that end, a *reference* configuration (“para-unrelaxed”) is defined in Fig. 5.7a: it corresponds to the truncated bulk paraelectric structure of  $\text{PbTiO}_3$  with the in-plane lattice constant constrained to that of  $\text{SrTiO}_3$  ( $a_{STO} = 3.90$  Å) and a consequent tetragonality  $c_0/a_{STO} = 1.03$  [9]. Fig. 5.7b (“ferro-unrelaxed”) shows the atomic distortion of the “up”-state as determined for bulk tetragonal  $\text{PbTiO}_3$  by Nelmes and Kuhs in Ref. [16] with  $c = 4.17$  Å. In order to quantify the surface relaxation, density functional theory calculations [18] were performed within the local density approximation (LDA) using the ABINIT [19] package. Two different supercells were considered : a thick  $\text{PbTiO}_3$  slab in vacuum (Fig. 5.7(c)) and a  $\text{SrTiO}_3$ /(one unit cell)  $\text{PbTiO}_3$ /vacuum stack [20](Fig. 5.7d). Insulating  $\text{SrTiO}_3$  was considered in our simulations since Nb doping is not presently affordable at the first-principles level [21]. To reproduce the substrate clamping effect, the in-plane lattice constant was fixed to the relaxed *a*-axis value of bulk  $\text{SrTiO}_3$  [22]. The atomic positions were then relaxed until the maximum residual atomic force was smaller than 40 meV/Å. Our calculations were restricted to (1×1) surface periodicity and did not allow for an eventual antiferrodistortive (AFD)  $c(2\times 2)$  reconstruction [23–25]. The latter is not excluded but, as discussed later, was not evidenced on our films at room temperature. The distortions in the upper half of each supercell are reported in Fig. 5.7c, d (“para-relaxed” state). For easy comparison with the experiment, because of the typical LDA underestimate of the lattice constant [22], the values are given as a percentage of  $c_0$ . The magnitudes of the ferroelectric and surface relaxation effects can now be compared. First, the cation-oxygen displacements due to ferroelectricity (11.6% - 8.3% of  $c_0$ , Fig. 5.7b) are significantly larger than the displacements due to surface relaxation/rumpling (3.4% - 1.4% of  $c_0$ , Fig. 5.7 (c) and 3.3% - 1.5% of  $c_0$ , Fig. 5.7d). Second, the mean layer

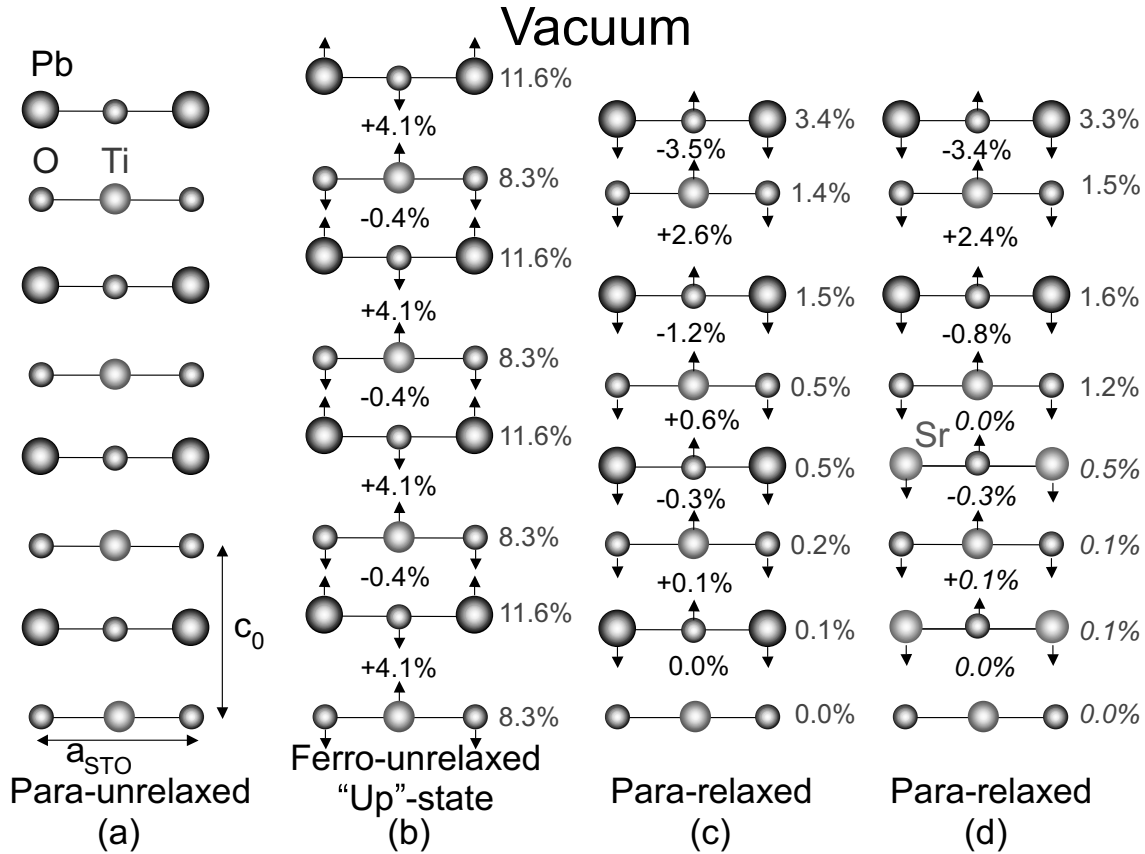


Figure 5.7: (Color online) Schematic view of the atomic displacements resulting from ferroelectric distortion and from surface/interface relaxation in the uppermost layers of a  $\text{PbTiO}_3$  film epitaxially grown on  $\text{SrTiO}_3$ . In bulk  $\text{PbTiO}_3$ , epitaxial strain produces a tetragonality at zero polarization that can be estimated from the macroscopic elasticity theory as  $c_0/a_{\text{STO}} = 1.03$ . The ionic configuration resulting from the truncation of such a strained bulk paraelectric state (a) is considered as the reference structure. Freezing the bulk ferroelectric distortion (as reported in Ref. [16]) into this reference structure results in the “up”-state shown in (b). Additionally, the natural ionic relaxation at the surface in the paraelectric state has been computed from first-principles (see text) both for a thick  $\text{PbTiO}_3$  slab in vacuum (c) and a  $\text{SrTiO}_3$ /(one unit cell)  $\text{PbTiO}_3$ /vacuum stack (d). Numbers in black correspond to the change of interlayer distances. Numbers in gray (blue) corresponds to the atomic rumpling in each layer (cation-oxygen distance). All the values are in % of  $c_0$ , except those in italic that concern  $\text{SrTiO}_3$  and are in % of  $a_{\text{STO}}$ .

displacement for the “up”-state (Fig. 5.7b) and for the surface relaxation (Figs. 5.7, c and d) are opposite. Third, the surface relaxation and rumpling effects are globally unaffected by the film thickness (Figs. 5.7, c and d) and their amplitude decays very quickly in the interior of the film : they are already negligible two unit cells below the surface. This implies that the XPD measurements will be probing both the narrow relaxed surface region and a few unit cells below, essentially not affected by the surface relaxation.

### 5.3.3 Experimental results and discussion

#### 5.3.3.1 Experimental details

The samples used in this study are epitaxial, *c*-axis oriented PbTiO<sub>3</sub> thin films grown on conducting (001) Nb-SrTiO<sub>3</sub> substrates using off-axis radio-frequency magnetron sputtering [26, 27]. Topographic measurements using atomic force microscopy (AFM) showed that these films are essentially atomically smooth, with a root-mean-square roughness between 2 and 6 Å over a 10 × 10 μm<sup>2</sup> area. Room temperature x-ray diffraction measurements, for films with thickness ≥ 28 Å allowed us to precisely determine the thickness and the *c*-axis parameter of the films, and to confirm their epitaxial “cube-on-cube” growth.

After growth and characterization, the films were transferred *ex-situ* to a modified Vacuum Generators ESCALAB Mk II photoelectron spectrometer. The XPD measurement system comprises a hemispherical electron energy analyzer with a three-channel detector, an x-ray photon source with two possible energies ( $h\nu = 1253.6$  eV and 1740 eV for MgK $\alpha$  and SiK $\alpha$  radiation, respectively), and a computer-controlled two-axis goniometer capable of rotating the photoelectron emission angle over the full hemisphere above the surface [28, 29].

The local geometry around a selected atom can be probed by performing an intensity versus emission-angle scan of a chosen photoemission line. Because of the chemical sensitivity of photoemission, a given atom type is then chosen by selecting one of its core levels. The outgoing photoemitted electrons exhibit a strongly anisotropic angular intensity distribution. This angular distribution is due to the interference of the directly emitted photoelectron wave with the scattered electron waves. The analysis of the interference (or diffraction) patterns is facilitated by the so-called “forward focusing” effect taking place for photoelectron kinetic energies greater than  $\approx 0.5$  keV. When considering a row of atoms, scattering at the first few atoms along this row focuses the electron flux in the emitter-scatterer direction (for a review see Ref. [30, 31]). This enhancement of the intensity in the emitter-scatterer direction is schematically illustrated by the gray (green) curve in Fig. 5.6a (right part) for the centro-symmetric “para”-state (continuous line) and the “up”-state (dotted line). The forward focusing effect is further amplified for electron scattering by heavy atoms. In a semi-classical picture this can be understood as the focusing of the electron wave by the high number of protons in high atomic number atoms [30]. Note that, despite the forward focusing effect, the experimentally measured angles are sensitive to multiple interferences, refraction and possible anisotropic atom vibrations at the surface. In the present case of PbTiO<sub>3</sub>, Pb scattering is highly dominant compared to the scattering by other elements [32]. As a first step, in order to probe the non-centro-symmetry, O was chosen as emitter-atom (O 1s core level,  $E_{kin} = 724.1$  eV), since it has the largest displacement [16] and has Pb scatterers as nearest neighbors (see Fig. 5.8). However, the O contribution from the Nb-SrTiO<sub>3</sub> substrate becomes non-negligible for films thinner than the photoelectron inelastic mean free path, making the study of films thinner than 20 Å more difficult. As a second step, in order to probe the tetragonality of the films, i. e., the *c/a* ratio of the Pb lattice (related to the polarization via the polarization-strain coupling as discussed below and in details in Ref. [9]), Pb was chosen as emitter-atom (Pb 4f<sub>7/2</sub> core level,  $E_{kin} = 1115.5$  eV), and Pb-Pb forward focusing directions were used. Since Pb atoms are absent from the substrate, this study can be done down to a monolayer of ferroelectric material.

### 5.3.3.2 Non-centro-symmetric position of oxygen atoms

First, considering oxygen as the emitter atom, fully automated computer code for calculating electron diffraction in atomic clusters (EDAC) via multiple scattering [33], based on the muffin-tin potential approximation [34] was used to calculate the XPD pattern. Fig. 5.8a shows four O 1s core level emission ( $E_{kin} = 724.1$  eV) interference patterns. One is the measurement made on a 20 Å thin film while the three others are multiple scattering EDAC calculations of the “up”-, “down”- and “para”-state. Intensities are plotted in a stereographic projection with the center corresponding to normal emission (polar angle  $\theta = 0^\circ$ ) and the outer border corresponding to grazing emission ( $\theta = 70^\circ$ ). The strongest intensities (surrounded by white ellipses) correspond to the scattering of O 1s photoelectrons by Pb nearest neighbours (see Fig. 5.8b). The white circle is a guide to the eye indicating the polar angle of maximum intensity for the measured interference pattern. It is evident that the polar angle position of this peak, which is directly linked to the O-Pb directions, is perfectly reproduced by the “up”-state calculation while the “para”- and the “down”-state simulations predict a different position. The “up”-state (down-shifted O position) corresponds to a smaller polar emission angle ( $\theta_{up}$  in Fig. 5.8b) appearing closer to normal emission (center of the interference pattern in Fig. 5.8a). Such measurements have also been performed on films with thicknesses of  $\sim 500, 200, 100, 60, 44$  and  $28$  Å, and all perfectly reflect the characteristics of the “up”-state <sup>a</sup>.

These conclusions, drawn from visual inspection of the interference patterns locally around the intensity maximum (Fig. 5.8a), are confirmed by a global matching approach using a reliability R-factor to evaluate the quality of the fit between the complete experimental interference pattern data and theory (Fig. 5.8b). The c-axis lattice constant value and the O and Ti shifts are the adjustable structural parameters. A cut in the (100) plane, containing Pb and O atoms, is shown to facilitate the discussion. In the calculation, O and Ti atoms are moved together and the dipole is continuously changed from the “down”-state to the “up”-state, crossing over the “para”-state. The best fit corresponds to the minimal R-factor value, which is reached when O and Ti atoms are shifted below the centro-symmetric position (parameters used for the “up”-state simulation in Fig. 5.8a), with an R-factor value of  $\approx 0.34$ . In comparison, for the same c-axis parameter but the opposite O and Ti atom shifts (parameters used for the “down”-state simulation in Fig. 5.8a), the calculation gives a much higher R-factor of  $\approx 0.47$ . In between (zero O shift), in the centro-symmetric “para”-state, the R-factor is  $\approx 0.45$  (parameters used for the “para”-state simulation in Fig. 5.8a).

It is important to note that surface relaxation and rumpling, neglected here, cannot weaken our conclusions; indeed they would give a picture resembling a “down”-state, the corresponding O-Pb atoms being shifted in the opposite direction than what is observed (see Fig. 5.7c). Also, the possibility of a surface AFD reconstruction was explored without finding evidence for it in our room temperature experiments.

This R-factor analysis therefore quantitatively confirms the observations made in Fig. 5.8a, namely that the measured interference pattern is best simulated with the “up”- state. This

---

<sup>a</sup>The presence of alternating  $180^\circ$  domains in our films can be ruled out from the XPD measurement because the two characteristic “up” and “down”-state “forward focusing” peaks are not observed simultaneously in the experimental diffractogram, Fig. 5.8a. This contrasts with the results of Fong et al. [8] on a insulating substrates.

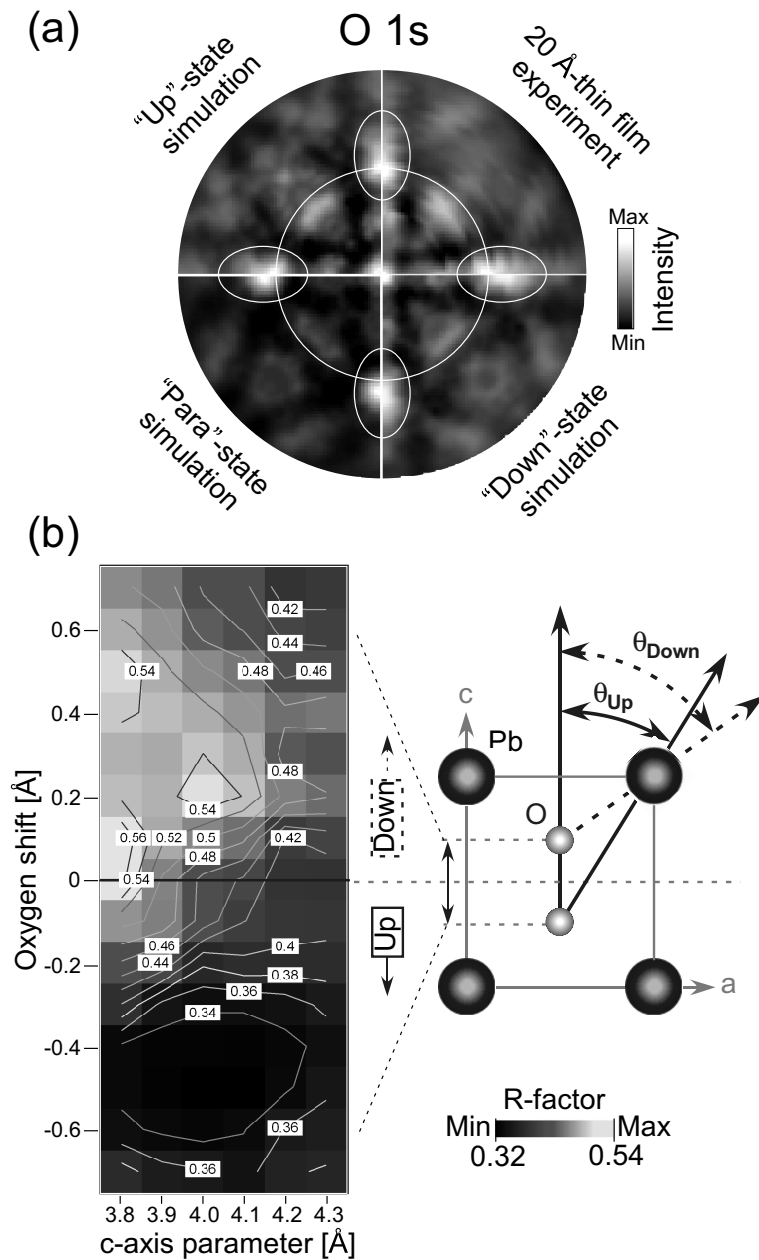


Figure 5.8: (Color online) (a) Stereographic projection of experimental and theoretical O 1s emission line intensities on quarter hemispheres for four different cases: experimental data for a 20 Å thin film and theoretical simulations taking into account “up”-, “para”- and “down”-state structures. Normal emission corresponds to the center of the plot and grazing emission ( $\theta = 70^\circ$ ) to the outer border. (b) R-factor calculation to quantify the agreement between experiment and simulations for different structures, where a low R-factor corresponds to good agreement. A cut in the (100)-plane containing Pb and O atoms is shown to facilitate the discussion. A downward shift of Pb and O atoms optimizes the fit.

demonstrates unambiguously that, for a film as thin as 20 Å the O atoms have a non-centrosymmetric position in the Pb cage corresponding to a non-vanishing spontaneous polarization, which is in agreement with the polar monodomain state observed in ultrathin PbTiO<sub>3</sub> films with synchrotron x-ray scattering by Fong and coworkers [35].

Let us emphasize that piezoelectric AFM measurements performed after the XPD experiments on the thickest films ( $\sim 500$  Å) confirmed the uniform “up”-state polarization while a uniform “down”-state polarization had been initially found for the same films just after growth. This confirms the *monodomain* character of the as grown sample and also indicates that the films are uniformly switched from “down” to “up”-state by exposure to our conventional x-ray source, attesting for the switchable character of the polarization. The details behind the switching are presently not known, but we believe that it occurs at the initial stage of the experiment while the measurement itself is essentially done in zero field. In fact, our results do not depend on the x-ray intensity, proving that the films are in equilibrium state during the measurements<sup>b</sup>. As discussed below, the agreement between the tetragonality deduced from x-ray diffraction and XPD also suggests that the measurements are performed in similar conditions.

#### 5.3.3.3 Tetragonality via lead emission

In a second step, considering Pb as the emitter atom, XPD was used to determine the tetragonality. As demonstrated in Ref. [9], below 200 Å the tetragonality decreases as the film thickness decreases. This decrease is a consequence of the strong polarization-strain coupling in PbTiO<sub>3</sub> and a signature of a reduced polarization in thin films. In Ref. [9], this polarization reduction was attributed to imperfect screening of the depolarizing field [12]. With XPD, using Pb as emitter, the tetragonality was measured down to the unit cell level as shown in Fig. 5.9. The absolute values of  $c/a$ , deduced from the forward focusing angles, are particularly large. This might reflect a strong enhancement of the polarization in the probed surface region (of the order of 80% for  $c/a = 1.15$ , from the PbTiO<sub>3</sub> polarization-strain coupling), even larger than in the theoretical prediction of Ref. [10]. However, as previously stated, we are not necessarily measuring the precise atom-atom directions and the anomalously large forward focusing  $c/a$  might also be related to other effects (anisotropic atom vibrations at the surface, refraction and multiple scattering interferences). Therefore a comparison with x-ray diffraction (XRD) [9] must be done at the relative level (Fig. 5.9, left and right scale).

To study the evolution of the tetragonality as a function of the film thickness, the measured XPD values are compared to the  $c/a$  values obtained by XRD. The XPD measurement on Fig. 5.9 confirms the evolution of  $c/a$  obtained from x-ray measurements in Ref. [9] and agrees with the theoretical prediction (dashed curve) relying on the suppression of polarization due to imperfect screening of the depolarizing field [9]. The similar thickness dependence for the XPD (very surface sensitive) and the x-ray measurements (average on the whole film) implies that the polarization evolves at the surface in the same way as at the interior of the film and that there is no thick paraelectric dead layer at the surface. In addition, the XPD tetragonality measurement shows a continuous decrease of tetragonality down to the thickness of one unit

<sup>b</sup>The influence of the x-ray intensity on the tetragonality was measured by investigating different x-ray powers. A modification of the tetragonality would have indicated, via the polarization-strain coupling, a variation of the spontaneous polarization. However no such modification was found.

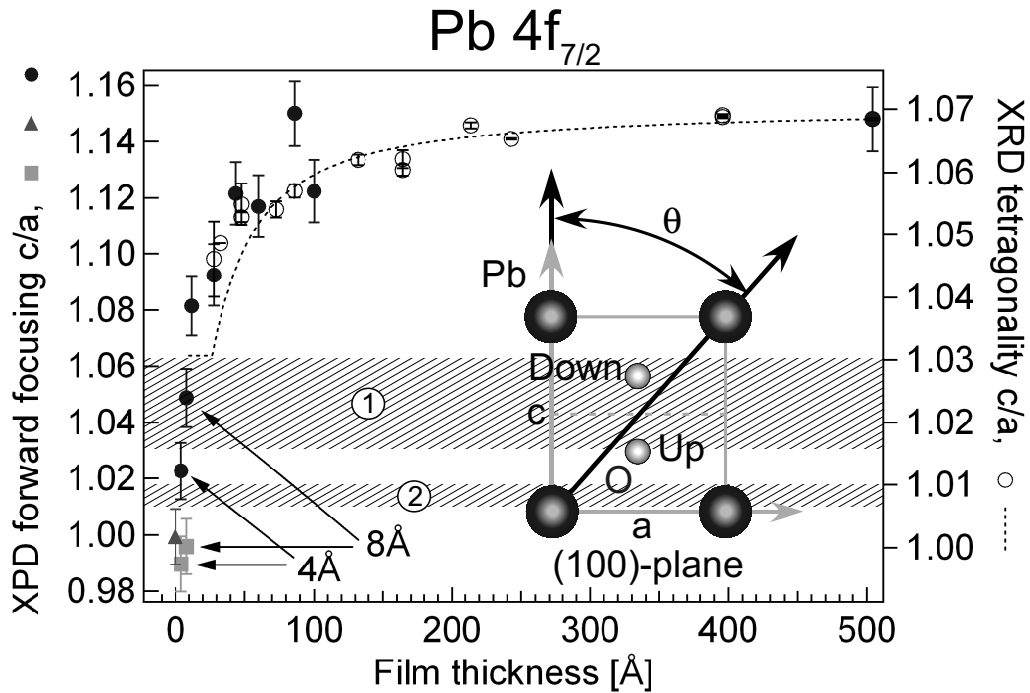


Figure 5.9: (Color online) Tetragonality ( $c/a$  ratio) as a function of film thickness for  $\text{PbTiO}_3$  films (blue) circles, for the  $\text{Nb-SrTiO}_3$  substrate through  $\text{PbTiO}_3$  films of one and two unit cells (green) squares and the  $\text{Nb-SrTiO}_3$  substrate surface (red) triangle. Black open circles are x-ray diffraction data and the black dotted curve is the result from model Hamiltonian calculations from Ref. [9]. Ribbons, labeled 1 and 2, indicate regions as discussed in the text. The left scale indicates the  $c/a$  values extracted from the XPD experiment forward focusing directions using  $\theta$ . The inset shows the crystallographic plane used to extract the  $c/a$  ratio. Pb-Pb scattering dominates compared to Pb-O scattering allowing  $\theta$  to be determined via Pb-Pb forward focusing.

cell [20]. Two ribbons are drawn in Fig. 5.9, labeled with 1 and 2. They indicate the regions within which  $c/a$  values of 1.03 and 1.01 are crossed with respect to both  $c/a$  scales. For film thicknesses above two unit cells, the  $c/a$  values are larger than 1.03, the value expected at the bulk level for the paraelectric phase (resulting from the mechanical constraint imposed by the substrate, see also Fig. 5.7a). This observation directly implies, via the polarization-strain coupling, that the films still have a finite -although progressively reduced- spontaneous polarization. At thicknesses of one or two unit cells, as can be seen on Fig. 5.9,  $c/a$  drops even more, reaching a value close to 1.01 for the one unit cell thick film [20]. This further decrease highlights that macroscopic elasticity no longer applies at such thicknesses where the interlayer atomic distances are affected by surface relaxation and rumpling as shown by the *ab-initio* calculations (Fig. 5.7d). The measured tetragonality agrees with the computed value of 1.01 for the one unit-cell thick relaxed paraelectric film suggesting the absence of any additional ferroelectric distortion at this thickness.

### 5.3.4 Conclusion

This study thus directly demonstrates non-centro-symmetry, unambiguously a result of ferroelectricity in  $\text{PbTiO}_3$  thin films down to 20 Å. The measurements of the tetragonality, with a continuous decrease down to the bare substrate, show that even extremely thin films (3 unit cells) have a  $c/a$  value larger than 1.03, attesting for the presence of a non-vanishing spontaneous polarization at this thickness scale. As the film thickness is reduced to a single unit cell, the experiments, together with calculations, strongly suggest that both non-centro-symmetry and tetragonality are governed by surface effects, giving rise for our geometry to a polar relaxed structure but without switchable ferroelectric distortion.

### Acknowledgements

We would like to thank M. A. Van Hove and C. Battaglia for helpful discussions, P. Paruch for careful reading of the manuscript, and the whole Neuchâtel workshop and electric engineering team for efficient technical support. This project has been supported by the Swiss National Science Foundation through the National Center of Competence in Research “Materials with Novel Electronic Properties-MaNEP”, the European Network of Excellence FAME and the VolkswagenStiftung.

### References for section 5.3

- [1] C. H. Ahn, K. M. Rabe, and J.-M. Triscone, *Science* **303**, 488 (2004).
- [2] H. N. Lee, H. M. Christen, M. F. Chisholm, C. M. Rouleau and D. H. Lowndes, *Nature* **433**, 395 (2005).
- [3] R. Waser and A. Rüdiger, *Nature Materials* **3**, 81 (2004).
- [4] M.-W. Chu, I. Szafraniak, R. Scholtz, C. Harnagea, D. Hesse, M. Alexe and U. Gösele, *Nature Materials* **3**, 87 (2004).
- [5] L. B. I. I. Naumov and H. Fu, *Nature (London)* **432**, 737 (2004).
- [6] T. Tybell, C. H. Ahn, and J.-M. Triscone, *Appl. Phys. Lett.* **75**, 856 (1999).
- [7] S. K. Streiffer, J. A. Eastman, D. D. Fong, C. Thompson, A. Munkholm, M. V. Ramana Murty, O. Auciello, G.R. Bai and G.B. Stephenson, *Phys. Rev. Lett.* **89**, 067601 (2002).
- [8] D. D. Fong, G. B. Stephenson, S. K. Streiffer, J. A. Eastman, O. Auciello, P. H. Fuoss and C. Thompson, *Science* **304**, 1650 (2004).
- [9] C. Lichtensteiger, J.-M. Triscone, J. Junquera and P. Ghosez, *Phys. Rev. Lett.* **94**, 047603 (2005).
- [10] P. Ghosez and K. M. Rabe, *Appl. Phys. Lett.* **76**, 2767 (2000).

- [11] B. Meyer and D. Vanderbilt, *Phys. Rev. B* **63**, 205426 (2001).
- [12] J. Junquera and P. Ghosez, *Nature* **422**, 506 (2003).
- [13] N. Sai, A. M. Kolpak and A. M. Rappe, *Phys. Rev. B* **72**, 020101(R) (2005).
- [14] A. Bune, V.M. Fridkin, S. Ducharme, L.M. Blinov, S.P. Palto, A.V. Sorokin, S.G. Yudin and A. Zlatkin, *Nature (London)* **391**, 874 (1998).
- [15] W. S. Yun, J. J. Urban, Q. Gu, and H. Park, *Nano Letters* **2**, 447 (2002).
- [16] R. J. Nelmes and W. F. Kuhs, *Solid State Commun.* **54**, 721 (1985).
- [17] F. Jona and G. Shirane, *Ferroelectrics Crystals* (Dover Publication, New York, 1997).
- [18] Tetrahedron conserving pseudopotentials were used with Pb (5d, 6s, 6p), Sr (4s, 4p, 5s), Ti (3s, 3p, 3d, 4s) and O (2s, 2p) treated as valence states, a plane-wave energy cutoff of 35 Ha and 6x6x1 k-point sampling of the Brillouin zone.
- [19] X. Gonze, J.-M. Beuken, R. Caracas, F. Detraux, M. Fuchs, G.-M. Rignanese, L. Sindic, M. Verstraete, G. Zerah, F. Jollet, M. Torrent, A. Roy, M. Mikami, Ph. Ghosez, J.-Y. Raty and D.C. Allan, *Computational Materials Science* **25**, 478 (2002).
- [20] Note that a film with thickness of one unit cell corresponds to two Pb-O and one Ti-O layers.
- [21] The Nb doping should have a minor effect on the relaxation at the paraelectric level except for ultrathin films for which the metallic character of the surface could allow a larger polar relaxation of the  $\text{PbTiO}_3$  surface.
- [22] At the bulk level, the calculations provide very similar theoretical in-plane lattice constant for cubic paraelectric  $\text{SrTiO}_3$  ( $a = 3.85\text{\AA}$ ) and tetragonal ferroelectric  $\text{PbTiO}_3$  ( $a = 3.86\text{\AA}$ ,  $c = 3.98\text{\AA}$ ) in spite of a global underestimate of the experimental value ( $a = 3.90\text{\AA}$ ) typical of the LDA.
- [23] C. Bungaro and K. M. Rabe, *Phys. Rev. B* **71**, 035420 (2005).
- [24] M. Sepliarsky, M. Stachiotti, and R. L. Migoni, *Cond. Mat* 0503524 (2005).
- [25] A. Munkholm, S. K. Streiffer, M. V. Ramana Murty, J. A. Eastman, C. Thompson, O. Auciello, L. Thompson, J. F. Moore and G. B. Stephenson, *Phys. Rev. Lett.* **88**, 016101 (2002).
- [26] C. B. Eom, J. Z. Sun, B. M. Lairson, S. K. Streiffer, A. F. Marshall, K. Yamamoto, S. M. Anlage, J. C. Bravman, T. H. Geballe, S. S. Laderman, R. C. Taber and R. D. Jacowitz, *Physica C* **171**, 354 (1990).
- [27] C. Lichtensteiger and J.-M. Triscone, *Int. Ferroelectrics* **61**, 143 (2004).
- [28] J. Osterwalder, T. Greber, A. Stuck, and L. Schlapbach, *Phys. Rev. B* **44**, 13764 (1991).

### 5.3 Direct evidence for ferroelectric polar distortion in ultrathin lead titanate perovskite films

- [29] D. Naumović, A. Stuck, T. Greber, J. Osterwalder and L. Schlapbach, *Phys. Rev. B* **47**, 7462 (1993).
- [30] W. F. Egelhoff Jr., *Critical Reviews in Solid State and Materials Sciences* **16**, 213 (1990).
- [31] C. S. Fadley, *Synchrotron Radiation Research: Advances in Surface Science* (Plenum, New York, 1990).
- [32] L. Despont, F. Clerc, M.G. Garnier, H. Berger, L. Forr and P. Aebi, Multiple scattering investigation of the 1T-TaS<sub>2</sub> surface termination, *Eur. Phys. J. B* **52**, 421 (2006).
- [33] F. J. Garcia de Abajo, M. A. Van Hove, and C. S. Fadley, *Phys. Rev. B* **63**, 075404 (2001).
- [34] J. B. Pendry, *Low Energy Electron Diffraction* (Academic Press, London, 1974).
- [35] D. D. Fong, C. Cionca, Y. Yacoby, G. B. Stephenson, J. A. Eastman, P. H. Fuoss, S. K. Streiffer, C. Thompson, R. Clarke, R. Pindak and E. A. Stern, *Phys. Rev. B* **71**, 144112 (2005).

## 5.4 Investigation of effective screening length in ferroelectrics by photoemission

### 5.4.1 Introduction

The question of a ferroelectric critical thickness, i.e., whether or not ferroelectricity can be maintained at reduced dimensions, is currently a highly active research topic, both experimentally [1–7] and theoretically [8–11]. In particular, it has been shown from first principles that for ultrathin films in the case of perfect screening of the depolarization field perovskite slabs can sustain a polarization perpendicular to the surface down to a thickness of 3 unit cells [8]. However the ferroelectric properties can be drastically modified by an incomplete screening of the depolarization field resulting from a non-zero screening length of the metal electrode [10–14]. The majority of these studies illustrates the predominant role of electrostatic boundary conditions, i.e., of the electrodes, making the knowledge of their screening capacity crucial in order to control/stabilize the ferroelectric polarization in ultrathin films.

A related issue is that of the dead layer in very thin capacitors (either ferroelectric or non-ferroelectric), which can often have an extrinsic origin connected with film fabrication issues or defects such as oxygen vacancies [15–19], but in otherwise ideal samples is eventually determined by the effective screening length of the electrodes [20–25]. Experimentally, the evaluation of this “dead layer” capacitance is obtained by measuring the in-series capacitance of a series of films of decreasing thickness. Such a measurement only gives information about the macroscopic quantities, and is not useful for separating the contributions of the top and bottom electrodes to the screening capability of the system. It is thus of interest to use an experimental method sensitive on the atomic scale which can probe the effective screening length  $\lambda_{eff}$ .

Here, we demonstrate that using photoemission based x-ray photoelectron spectroscopy (XPS) to study the potential drop across the ferroelectric film and x-ray photoelectron diffraction (XPD) to simultaneously probe the tetragonality (and therefore the polarization via the polarization-strain coupling), we can model the effective screening lengths of ferroelectric thin films that have the substrate as a bottom electrode and the exposed-to-air surface as the top electrode. Experimentally the system and therefore the modelled screening length can be modified by a controlled plasma treatment of the surface.

### 5.4.2 Experiments

The materials studied in this paper are epitaxial c-axis oriented  $\text{PbTiO}_3$  (PTO) perovskite films grown using off-axis magnetron sputtering onto metallic (001)  $\text{Nb-SrTiO}_3$  substrates [27]. Topographic measurements using atomic force microscopy showed that these films are essentially atomically smooth. X-ray diffraction (XRD) measurements allowed us to precisely determine the thickness and tetragonality of the films and to confirm epitaxial growth. XPS and XPD measurements are performed at room temperature in a modified Vacuum Generators ESCALAB Mark II X-ray photoelectron spectrometer equipped with a fixed hemispherical electron energy analyzer, a three channeltron detection system, an x-ray photon source ( $h\nu=1253.6$

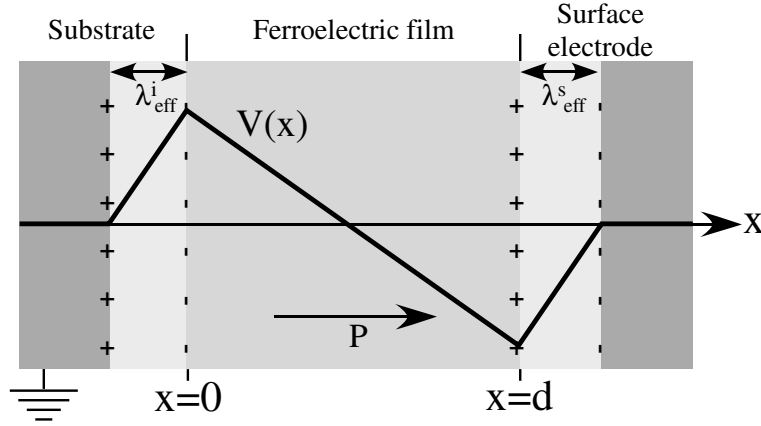


Figure 5.10: Schematic representation of the potential drop across a ferroelectric film. Note that dimensions are not to scale, *i.e.*,  $\lambda_{eff}$  is much smaller than the thickness of the electrodes or the film.

eV (MgK $\alpha$ )), and a computer-controlled two-axis goniometer capable of scanning the electron emission angle over the full hemisphere above the surface [28, 29], operating with a base pressure in the  $10^{-11}$  mbar region. The XPS and XPD methods are used with the same setup and thus the same surface region is probed in each experiment. More details about XPS and XPD, which is capable to extract local, real space information around a selected type of atom close to the surface, are given in Ref. [6]. Note that the samples were exposed to air during the transfer to the x-ray spectrometer therefore creating a randomly distributed layer of different oxide species such as OH, CO and H<sub>2</sub>O on top of the PTO films. In this paper we treat this layer as a top electrode, characterized by an effective screening length. The properties of this layer may be modified by an O plasma cleaning procedure, which reduces the quantity of these oxide compounds. The obtained results are interpreted in terms of a potential drop across the ferroelectric film, as shown in Fig. 5.10.

In a ferroelectric thin film a uniform polarization can only be stabilized if charges are provided that compensate the bound charges related to the termination of the ferroelectric polarization. In the case of real electrodes, the compensation charges are not located “exactly” at the location of the ferroelectric polarization charges, but they are distributed over a finite length. One way of mathematically dealing with this problem is the so called air-gap approach in which one considers a sheet of charge separated by a finite distance, the effective screening length  $\lambda_{eff}$ , from the physical ferroelectric-electrode interface (Fig. 5.10). The  $\lambda_{eff}$  length depends on the capacity of the electrode to screen the polarization charges inside the ferroelectric film and may be different at the interface with the substrate ( $\lambda_{eff}^i$ ) and at the surface ( $\lambda_{eff}^s$ ). The existence of a non-zero  $\lambda_{eff}$  is at the origin of an incomplete screening of the polarization charges. This incomplete screening generates a residual depolarization field and the corresponding potential drop  $V(x)$  (Fig. 5.10, continuous line) across the ferroelectric film. Under short-circuit boundary conditions, the potential maxima at the substrate-ferroelectric film interface is  $V(x = 0) \simeq \frac{\lambda_{eff}^i P}{\epsilon_0}$ , and at the ferroelectric film-surface electrode interface  $V(x = d) \simeq -\frac{\lambda_{eff}^s P}{\epsilon_0}$  [11, 30].

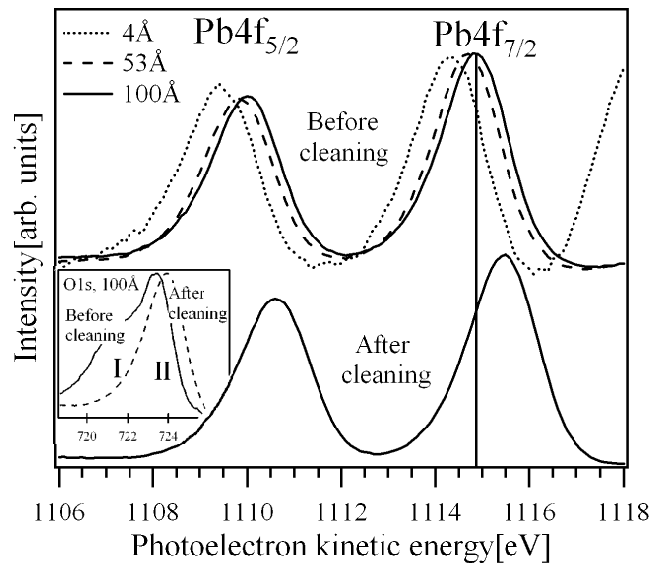


Figure 5.11: Pb  $4f_{7/2}$  XPS spectra (obtained with  $\text{MgK}\alpha$  radiation) for different PTO film thicknesses, before and after the cleaning procedure. The inset illustrates the effect of the cleaning procedure on the O 1s emission line. O 1s (I) is the emission from the contamination layer while O 1s (II) originates from the PTO.

### 5.4.3 Results and discussion

Figure 5.11 (top) shows the main difference observed between photoemission spectra of samples with different thicknesses, namely a shift of some photoemission lines towards decreasing  $E_{kin}$  for decreasing thickness. This shift is of the same magnitude for Pb and Ti lines but not for the C line, which is contained in the contamination layer. An interpretation of these shifts as simple sample charging can thus be ruled out since not all the peak shifts are identical. Also, the fact that Pb and Ti lines are shifted by the same amount indicates that it is not due to a chemical effect. The behavior of the O line cannot be described so easily, as it comprises both a sample and a contamination layer contribution (inset of Fig.5.11).

In Fig. 5.12 the relative positions of the  $\text{Pb}4f_{7/2}$  line and the tetragonality ( $c/a$ ) are superimposed for samples with different thicknesses ( $c/a$  is the ratio of the out-of-plane and in-plane lattice constants). The similarity of these two curves suggests that these results are correlated. Indeed, the polarization gives rise to a strain (polarization-strain coupling) which is measured as an increase in the tetragonality. The polarization also produces a surface potential drop  $V(x)$  which affects the photoelectron kinetic energy  $E_{kin}$ . The polarization in Fig. 5.12 (inset) is calculated using  $(c/a) - (c/a)_0 = \alpha P^2$ . The  $(c/a)_0 = 1.03$  value corresponds to the paraelectric phase [4] and  $\alpha = 0.0574 \frac{\text{m}^4}{\text{C}^2}$  is the polarization-strain coupling parameter obtained by Ghosez [32]. In order to consider the bulk polarization of the films, the  $c/a$  values obtained by the XPD measurements, which are sensitive only to the surface, have been rescaled to correspond to the bulk sensitive XRD values as described in detail in Ref. [6].

For a quantitative comparison, the description of the potential drop has to be complemented to deal with photoemission as follows. The electron inelastic mean free path (imfp) has to be

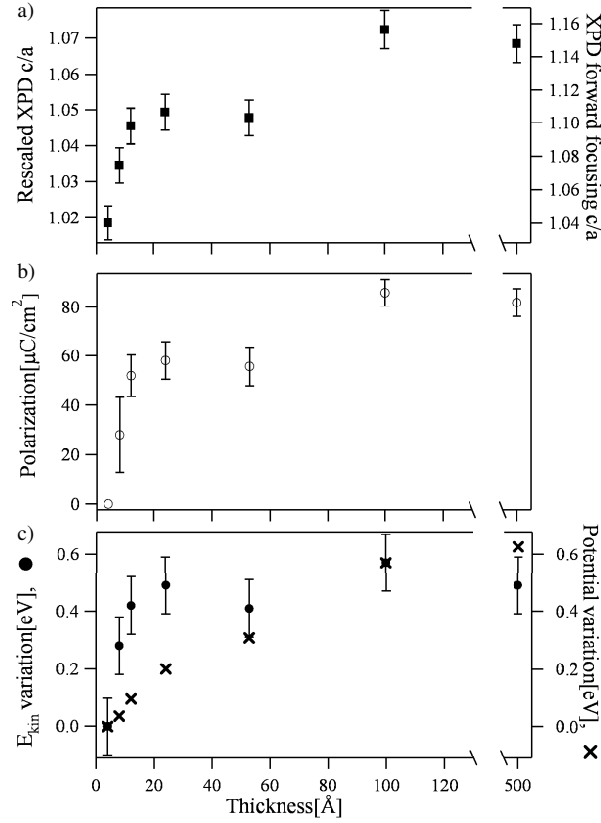


Figure 5.12: (a) Tetragonality ( $c/a$  ratio) as a function of film thickness for PbTiO<sub>3</sub> films. The right scale indicates the  $c/a$  values extracted from the XPD experiment while the left scale corresponds to the rescaled value using XRD results. (b) Polarization calculated using the rescaled tetragonality. (c) Pb 4f<sub>7/2</sub> emission line position shifts (black circles) as a function of film thickness and potential variation  $\bar{V}$  (crosses) calculated separately for each thickness.

included to allow for the finite escape depth of photoelectrons in order to calculate the mean potential drop  $\bar{V} = \frac{\int_0^d dx e^{-(d-x)/\text{imfp}} V(x)}{\int_0^d dx e^{-(d-x)/\text{imfp}}}$  probed by the photoelectrons. A value of 8 Å has been used for imfp. In other words, for a photoemission line that is due to photoelectrons emitted from different depths in the film, one can estimate an average potential drop (shift),  $\bar{V}$ , by considering the potential drop at each depth, weighted by the imfp. Because of the exponential attenuation of electrons coming from deeper layers, the  $\bar{V}$  is thus mainly determined by the potential drop at the surface  $V(x=d) \simeq -\frac{\lambda_{eff}^s P}{\epsilon_0}$ , as shown above.

Thus, taking the potential drop from XPS and estimating the polarization from XPD, it is possible to access the surface  $\lambda_{eff}^s$ . Therefore, with a fixed  $\lambda_{eff}^s$  and  $P$  extracted from  $c/a$  (see above) for every thickness  $d$  (inset of Fig. 5.12),  $\bar{V}$  can be computed and compared to the measured variation of  $E_{kin}$ . The procedure can be repeated for different  $\lambda_{eff}^s$  in order to optimize agreement. The best agreement is obtained with  $\lambda_{eff}^s = 0.07 \text{ \AA}$ , a value comparable to the one found in Ref. [4], which gives the potential variation plotted in Fig. 5.12.

In comparison to the determination of the screening length from XRD alone [4] this method

has an advantage in that one level of modeling is removed from the process. Although it is still necessary to infer the polarization from structural information through the use of the strain-polarization coupling, the potential drop that results from the depolarization field is now measured directly, whereas previously a model hamiltonian was used to extract the value of the depolarization field, from which the screening length could then be estimated.

To confirm that the screening at the top of the sample is due to surface adsorbates, we show that the surface  $\lambda_{eff}^s$  can be modified using a soft oxygen plasma cleaning procedure together with a sample annealing. In this process, the sample temperature is first increased up to  $\sim 500^\circ\text{C}$  in vacuum during several hours. No modification of the PTO compound stoichiometry can be observed after this annealing. Following this, an O plasma (0.05 mbar of  $\text{O}_2$ ) is produced near the surface for few minutes. After the plasma treatment, the sample is left hot for a few minutes.

The effect of this procedure, applied to the different films thicker than  $28\text{\AA}$ , is clearly seen on the XPS spectrum, as shown in Fig. 5.11 for the O1s and Pb4f emission lines of a  $100\text{\AA}$  thick film. The C emission (not shown here) and the O emission lines of the surface contamination layer are drastically reduced and a low energy electron diffraction pattern can be obtained, indicating that the surface contamination layer has mostly been removed. In parallel, an additional shift of  $\sim 0.4\text{-}0.6$  eV for the PTO peaks is observed.

As the tetragonality ( $c/a$  measured by XPD) remains unchanged after the sample cleaning, it suggests that the  $E_{kin}$  increase observed upon cleaning is not correlated to a ferroelectric polarization enhancement, but rather to an increase of the surface  $\lambda_{eff}^s$ . The invariance of the tetragonality suggests that the bottom electrode has a significantly worse screening capacity than the top electrode and that small changes in the top electrode screening do not result in large changes in the polarization. The additional shift of  $0.4\text{-}0.6$  eV corresponds to an increase of the surface  $\lambda_{eff}^s$  of  $\approx 0.05\text{-}0.07\text{\AA}$ . This suggests that as the surface contamination layer is removed with the plasma, its capacity to screen the macroscopic field generated by the polarization charges inside the ferroelectric thin film is also reduced and thus  $\lambda_{eff}^s$  increases.

#### 5.4.4 Conclusion

In conclusion, we have shown that the effective screening length  $\lambda_{eff}^s$  of surface layers can be modelled with an approach combining XPS and XPD measurements, together with a simple description of the potential drop across the ferroelectric film. Here,  $\lambda_{eff}^s$  values have been obtained for exposed-to-air and O plasma cleaned surfaces therefore demonstrating the tuning of the effective screening length by controlled modification of the surface. The method could be applied to determine the screening properties of a wide range of atomic or molecular surface coverages. In turn, the understanding of how the different species contribute to the screening may enable some novel applications, from optimizing the surface conditions to allow ferroelectricity in increasingly thin films, to utilizing the response of the ferroelectric to surface contaminants as a detection method.

## Acknowledgements

Acknowledgements: We would like to thank N. Stucki for helpful discussions, and the whole Neuchâtel workshop and electric engineering team for efficient technical support. This project has been supported by the Swiss National Science Foundation through the National Center of Competence in Research “Materials with Novel Electronic Properties-MaNEP”, and Division II.

## References for 5.4

- [1] T. Tybell, C. H. Ahn and J.-M. Triscone, *Appl. Phys. Lett.* **75**, 856 (1999).
- [2] S. K. Streiffer, J. A. Eastman, D. D. Fong, C. Thompson, A. Munkholm, M. V. R. Murty, O. Auciello, G. Bai and G. Stephenson, *Phys. Rev. Lett.* **89**, 067601 (2002).
- [3] D. D. Fong, G. B. Stephenson, S. K. Streiffer, J. A. Eastman, O. Auciello, P. H. Fuoss and C. Thompson, *Science* **304**, 1650 (2004).
- [4] C. Lichtensteiger, J.-M. Triscone, J. Junquera and P. Ghosez, *Phys. Rev. Lett.* **94**, 047603 (2005).
- [5] M. Dawber, C. Lichtensteiger, M. Cantoni, M. Veithen, P. Ghosez, K. Johnston, K. M. Rabe and J.-M. Triscone, *Phys. Rev. Lett.* **95**, 177601 (2005).
- [6] L. Despont, C. Lichtensteiger, C. Koitzsch, F. Clerc, M. G. Garnier, F. J. Garcia de Abajo, E. Bousquet, P. Ghosez, J.-M. Triscone, and P. Aebi, *Phys. Rev. B* **73**, 094110 (2006).
- [7] V. Nagarajan, J. Junquera, J. Q. He, C. L. Jia, R. Waser, K. Lee, Y. K. Kim, S. Baik, T. Zhao, R. Ramesh, Ph. Ghosez and K. M. Rabe, *J. Appl. Phys.* **100**, 051609 (2006).
- [8] P. Ghosez and K. M. Rabe, *Appl. Phys. Lett.* **76**, 2767 (2000).
- [9] B. Meyer and D. Vanderbilt, *Phys. Rev. B* **63**, 205426 (2001).
- [10] J. Junquera and P. Ghosez, *Nature* **422**, 506 (2003).
- [11] M. Dawber, P. Chandra, P.B. Littlewood and J.F. Scott, *J. Phys. C.* **15** L393 (2003).
- [12] I. P. Batra and B. D. Silverman, *Solid. Stat. Comm.* **11**, 291 (1972).
- [13] I. P. Batra, P. Wurfel and B. D. Silverman, *J. Vac. Sci. Technol.* **10**, 687 (1973).
- [14] R. R. Mehta, B. D. Silverman, and J. T. Jacobs, *J. Appl. Phys.* **44**, 3379 (1973).
- [15] W. Känzig, *Phys. Rev.* **98**, 549 (1955).
- [16] P. K. Larsen, G. J. M. Dormans, D. J. Taylor, and P. J. van Veldhoven, *J. Appl. Phys.* **76**, 2405 (1994).
- [17] A. K. Tagantsev, M. Landivar, E. Colla, and N. Setter, *J. Appl. Phys.* **78**, 2623 (1995).

- [18] M. Dawber and J. F. Scott, *Appl. Phys. Lett.* **76**, 1060 (2000).
- [19] M.M. Saad, P. Baxter, R.M. Bowman, J.M. Gregg, F.D. Morrison and J.F. Scott, *J. Phys.: Condens. Matter* **16**, L451 (2004).
- [20] C. A. Mead, *Phys. Rev. Lett.* **6**, 545 (1961).
- [21] H. Y. Ku and F. G. Ullman, *J. Appl. Phys.* **35**, 265 (1964).
- [22] J. G. Simmons, *Appl. Phys. Lett.* **6**, 54 (1965).
- [23] C.T. Black and J.J. Welser, *IEEE Trans. Electron Devices* **46**, 776 (1999).
- [24] M. Dawber and J.F. Scott, *Jpn. J. Appl. Phys.* **41**, 6848 (2002).
- [25] M. Stengel and N. A. Spaldin, *Nature* **443**, 679 (2006).
- [26] D.D. Fong et al., *Phys. Rev. Lett.* **96**, 127601 (2006).
- [27] C. Lichtensteiger and J.-M. Triscone, *Int. Ferroelectrics* **61**, 143(2004).
- [28] J. Osterwalder, T. Greber, A. Stuck and L. Schlapbach, *Phys. Rev. B* **44**, 13764 (1991).
- [29] D. Naumović, A. Stuck, T. Greber, J. Osterwalder and L. Schlapbach, *Phys. Rev. B* **47**, 7462 (1993).
- [30] Ph. Ghosez and J. Junquera, *Handbook of theoretical and computational nanotechnology*, vol. 9, Chapter 134 (American Scientific Publishers, Stevenson Ranch, USA, 2006).
- [31] M. D. Fontana, H. Idrissi, G. E. Kugel and K. Wojcik, *J. Phys.: Condens. Matter* **3**, 8695 (1991).
- [32] P. Ghosez, Private communication (2007).



## 5.5 Influence of the boundary conditions

### 5.5.1 Local structure investigation of $\text{SrTiO}_3/\text{PbTiO}_3$ superlattices

In the preceding chapter, the effect on the ferroelectricity of a reduced film thickness has been probed. We have shown that when the film thickness is reduced to one or two unit cells, both non-centro-symmetry and tetragonality are governed by surface effects. Now what happens for the case of a superlattice configuration made of alternated layers of PTO and STO, implying a completely different dielectric environment for the PTO?

Dawber *et al.* have shown that the polarization is reduced in PTO/STO superlattices as the PTO thickness is decreased but also that a surprising recovery of the ferroelectricity occurs for PTO/STO ratios smaller than 1 [1]. In parallel, Tenne *et al.* have demonstrated that one unit cell thick  $\text{BaTiO}_3$  (BTO) in BTO/STO superlattices is not only ferroelectric but also polarizes the paraelectric STO layers adjacent to it [2]. These behaviors, intimately related to boundary conditions, are observed by averaging measurements (XRD) [1] or by using an indirect method (ultraviolet Raman spectroscopy) [2].

By using XPD, it is possible to obtain independently the STO and PTO surface tetragonality of a PTO/STO superlattice owing to the chemical sensitivity of the method. Moreover, in some specific cases it is possible to determine the PTO tetragonality below few STO cells and the STO tetragonality below few PTO cells. But a *cubic* STO topmost layer can influence the signal coming from a deeper tetragonal PTO layer and thus modify the measurement of the bulk tetragonality. Indeed if the signal coming from a tetragonal PTO cell passes through a cubic STO layer, the effective tetragonality is artificially reduced. MSC calculations are performed for PTO/STO superlattices to quantify such behaviors. Based on these results, we propose a correction table to extract the real bulk tetragonality from the measured tetragonality.

The chemical sensitivity of the XPD permits to extract independently the Sr and Pb signals of a PTO/STO superlattice if the topmost layer, either STO or PTO, is thin enough (one or two unit cells). Here we will focus our attention on this case, PTO below one or two STO cubic layers.

The Fig. 5.13a illustrates how the measured bulk tetragonality can be affected by different parameters. First we calculate the tetragonality correction to apply to PTO films, without STO topmost layers, in the paraelectric or ferroelectric up-state, labeled with open rhombus and triangles respectively. The tetragonality correction is obtained by (i) calculating the diffraction pattern (with the EDAC code) of the given cluster, (ii) fitting the forward focusing peak corresponding to the  $\langle 101 \rangle$  direction (see Section 5.2), (iii) calculating the difference between the obtained value and the geometrical ( $c/a$ ) used to create the cluster.

The Fig. 5.13a illustrates how the measured bulk tetragonality can be affected by different parameters. First we calculate the tetragonality correction to apply to pure PTO films (without STO topmost layers) in the paraelectric or ferroelectric up-state, labeled with open rhombus and triangles respectively. The tetragonality correction is obtained by (i) calculating the diffraction pattern (with the EDAC code) of the given cluster, (ii) fitting the forward focusing peak corresponding to the  $\langle 101 \rangle$  directions (see Section 5.2), (iii) calculating the difference between

the obtained value and the geometrical ( $c/a$ ) used to create the cluster.

For the paraelectric  $c/a = 1$  case, only the effect of the surface potential step  $V_o$  affects the tetragonality, acting like a negligible artificial compression of 0.1%. This influence is tiny compared to others like the tetragonality, the polar distortion or the presence of one or two cubic STO topmost layers. For the paraelectric  $c/a > 1$  case, the bulk tetragonality is artificially enhanced by more than 0.5% of  $c/a$ , certainly due to the anisotropy increase related to the cubic-tetragonal transition. If a polar up-state distortion is induced in the PTO film, the artificial enhancement of the  $c/a$  of the paraelectric case is rather uniformly compensated and the measured tetragonality is similar to the real bulk tetragonality.

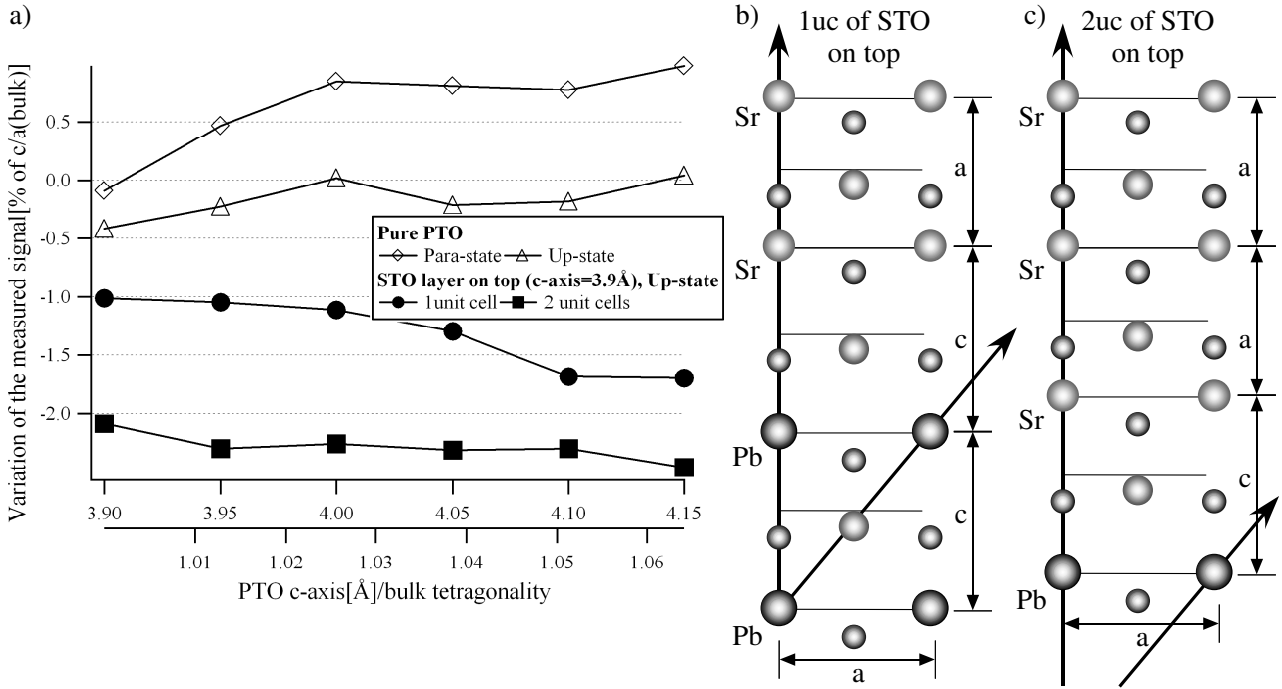


Figure 5.13: (a) Correction table to apply to the measured tetragonality to obtain the real bulk tetragonality for different cases. The two cases with a STO topmost layer are sketched in (b) and (c) for a one and two unit cell thick STO layer respectively. The labels  $a$  and  $c$  correspond to the in-plane and out-of-plane axis parameters.

Then if one or two STO cubic cells are added on the ferroelectric up-state PTO film, as seen in Fig. 5.13b and c, the variation of the apparent PTO bulk tetragonality becomes larger (black disks and squares in Fig. 5.13a). Note that because of the large electrostatic cost of having different polarizations in each layer, the up-state distortion has also been included in the STO layers, according to Ref. [2]. For a one unit cell thick layer of STO, the measured tetragonality appears to be reduced by  $\approx 1$  to 1.7% compared to the real bulk tetragonality. For a two unit cells thick layer of STO, the artificial tetragonality reduction becomes even larger, from  $\approx 2.1$  to 2.5% of the bulk tetragonality.

These corrections are essential in order to extract the real PTO bulk tetragonality. Here only cubic STO cells are used but in reality, STO with  $c/a > 1$  could also exist. Obviously,

when PTO and STO  $c/a$  values are very close to each other, the STO topmost layer affects less the measurement of the PTO bulk tetragonality. This effect is visible in Fig. 5.13a where the  $c/a$  correction increases for increasing bulk tetragonality in both cases with cubic STO on top of PTO. Thus the use of a STO topmost layer with  $c/a = 1$  represents the case where the variation of the tetragonality is the largest compared to the conventional bulk PTO tetragonality ( $c/a \approx 1.06$ ) and provides the maximal correction bound.

### 5.5.2 $\text{PbTiO}_3$ on $\text{La}_{0.67}\text{Sr}_{0.33}\text{MnO}_3$

Two PTO films (27 and 250 Å -thick ) deposited on  $\text{La}_{0.67}\text{Sr}_{0.33}\text{MnO}_3$  (LSMO) have been measured by means of XPD in order to determine their tetragonality. The LSMO substrates have been grown by J. B. Yau and J. Hoffman in the group of C. Ahn at Yale University, using off-axis magnetron sputtering. Then, PTO films have been grown on LSMO at the University of Geneva.

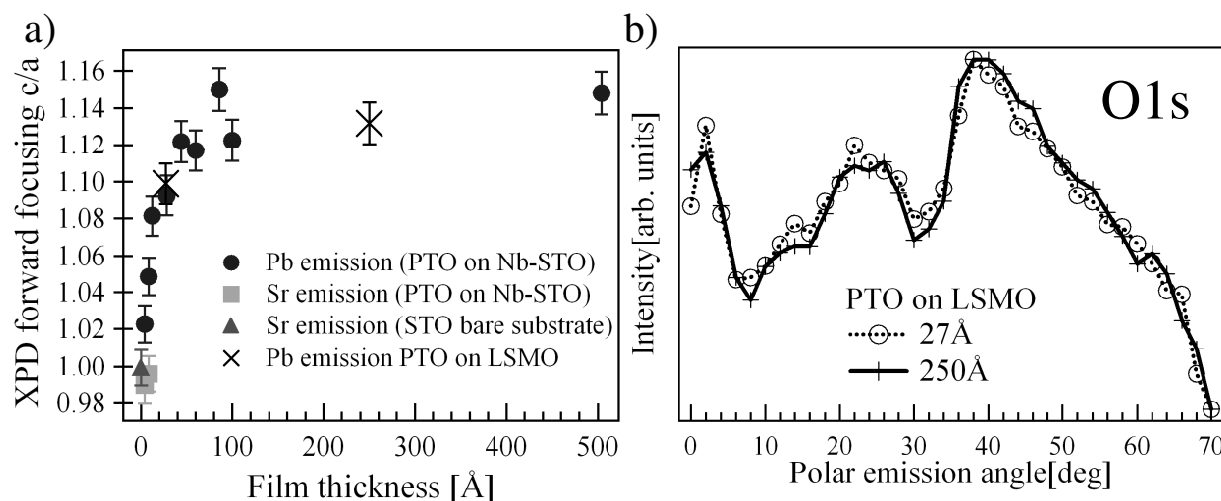


Figure 5.14: (a) Tetragonality ( $c/a$  ratio) as a function of film thickness for PTO films deposited on Nb-STO (black circles), for Nb-STO substrate measured through PTO films (gray squares), for the Nb-STO substrate surface (gray triangle) and for PTO films deposited on LSMO (black crosses). (b) Polar cuts along the  $\langle 100 \rangle$  directions for the two different PTO film thicknesses deposited on LSMO .

XRD has been performed on these films and has revealed that, contrary to the PTO on Nb-STO case, the tetragonality shows a decrease with decreasing thickness, followed by a recovery [3], which can be explained by the switching from a monodomain to a polydomain (with up- and down-state) configuration. This behavior has been studied by Nagarajan for  $\text{SrRuO}_3/\text{PbZr}_{0.2}\text{Ti}_{0.8}/\text{SrRuO}_3/\text{SrTiO}_3$  heterostructures in Ref. [4], where one sees that the polydomain configuration reduces the depolarization field responsible of the film tetragonality decrease.

Nevertheless, contrary to results obtained by XRD, the tetragonality obtained using XPD

is similar to the result for PTO deposited on Nb-STO, as shown in Fig. 5.14a. This would indicate that in our measuring conditions the samples are monodomain, and in an up-state configuration. Indeed, no drastic difference is visible between the O emission polar scans taken along the  $\langle 100 \rangle$  directions for the two PTO film thicknesses, as seen in Fig. 5.14b.

### 5.5.3 Ferroelectric polarization switching using XPD

XRD measurements performed after the XPD analysis of the PTO/LSMO samples reveal a polydomain configuration for the  $27\text{\AA}$ -thick film. It appears thus that during the XPD measurement, the samples are forced to be in a monodomain configuration with a concomitant increase of the depolarization. This effect tends to reduce the polarization and thus the tetragonality for very thin films. The sample returns in its more stable polydomain state when the XPD measurement is over.

In other cases, the sample can stay in the configuration induced during the XPD measurements. This has been checked using the piezoresponse mode of the atomic force microscopy (PFM) on a  $500\text{\AA}$ -thick PTO film deposited on Nb-STO. Alternate voltages are applied between a metallic tip and the film to polarize parallel stripes and the piezoresponse (piezoelectric deformation) is then measured by applying an AC voltage lower than the coercive voltage. When it is possible to write up- or down-state stripes, one can deduce the down- or up-state background polarization respectively, as writing stripes with the same polarization as the background has no effect.

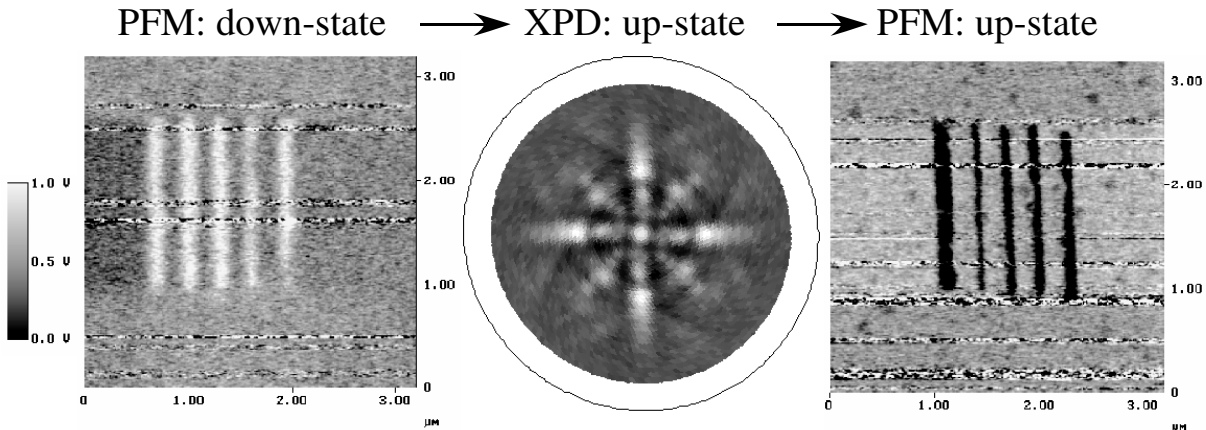


Figure 5.15: Effect of the XPD method on the ferroelectric polarization. AFM measurements have been performed in Geneva by C. Lichtensteiger.

As illustrated in Fig. 5.15, the first PFM measurement performed on an as grown  $500\text{\AA}$ -thick PTO film deposited onto Nb-STO reveals a down-state monodomain configuration. Then the XPD O<sub>1s</sub> emission diffraction pattern performed on the same sample shows an up-state polarization. After the XPD measurement, a PFM measurement has again been done and confirms that the ferroelectric polarization has been switched during the XPD measurement and stays in its up-state configuration.

It is worth noting that in the case of PTO/LSMO, the electrostatic energy cost needed to remain polydomain for very thin films can be paid when the XPD measurement is running but turns out to be insufficient to stabilize this configuration afterwards while, in the case of PTO/STO, the substrate allows the up-state polarization to persist after the end of the XPD measurement. This observation is thus a direct indication of the importance of the substrate on the ferroelectric instability. We could thus imagine the case of a substrate which will be able to stabilize the down-state or the polydomain configuration during or even after the XPD measurements <sup>c</sup>.

Interestingly, both XRD and XPD use x-rays (several keV) for the sample analysis but only the XPD method appears to be able to act on the ferroelectric polarization. The main difference between both methods is that the sample environment is drastically different, either the air or the vacuum. The vacuum allows the electrons generated during the x-ray creation (x-ray window) to reach the sample surface while they are stopped by the air in the case of the XRD method. This electron shower could play a major role in the ferroelectric polarization switching. Indeed, in the same manner as the as grown down-state configuration observed on PTO/Nb-STO films could be due to the  $\text{Ar}^+$  ions created in the O-Ar plasma atmosphere during the sample growth, the  $e^-$  shower can certainly affect the ferroelectric polarization and induce an up-state.

To check whether the electron shower generated by the x-ray creation is the right explanation for the down-state to the up-state film switching for PTO/Nb-STO and the apparently forced monodomain configuration during the measurements of PTO/LSMO films, an x-ray source without  $e^-$  creation is needed, for instance synchrotron radiation.

#### 5.5.4 Reversible $\text{PbTiO}_3$ surface states, applying O and H plasma

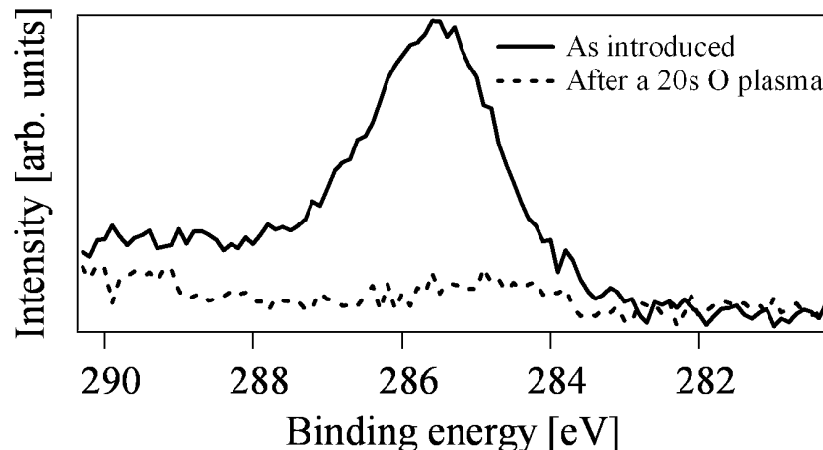


Figure 5.16:  $\text{C}1s$  XPS spectrum of a thin PTO film measured at a grazing emission angle, before and after a 20 seconds O plasma exposure.

<sup>c</sup>This point will be discussed in more details in the sub Section 5.5.5.

The first step of the PTO sample treatment consists in removing the C contaminant located at its surface. It is unfortunately not possible to completely remove C contaminant from the PTO surface using conventional annealing. However, using an O plasma, C can be entirely removed without destroying the sample or modifying its stoichiometry. The result of such an O plasma cleaning is shown in Fig. 5.16 for the C 1s peak. Note that the spectrum has been collected at a grazing emission angle to enhance the surface sensitivity.

Moreover, the O1s spectrum of the freshly introduced film is not affected by this 20 seconds O plasma and is similar to the spectrum taken after the O plasma shown in Fig. 5.17a. It consists of three oxide compounds: the peak at lower binding energy corresponds to PbO oxide, the middle peak to  $TiO_x$  oxide, while the O peak at high binding energy stems from  $H_2O$ .

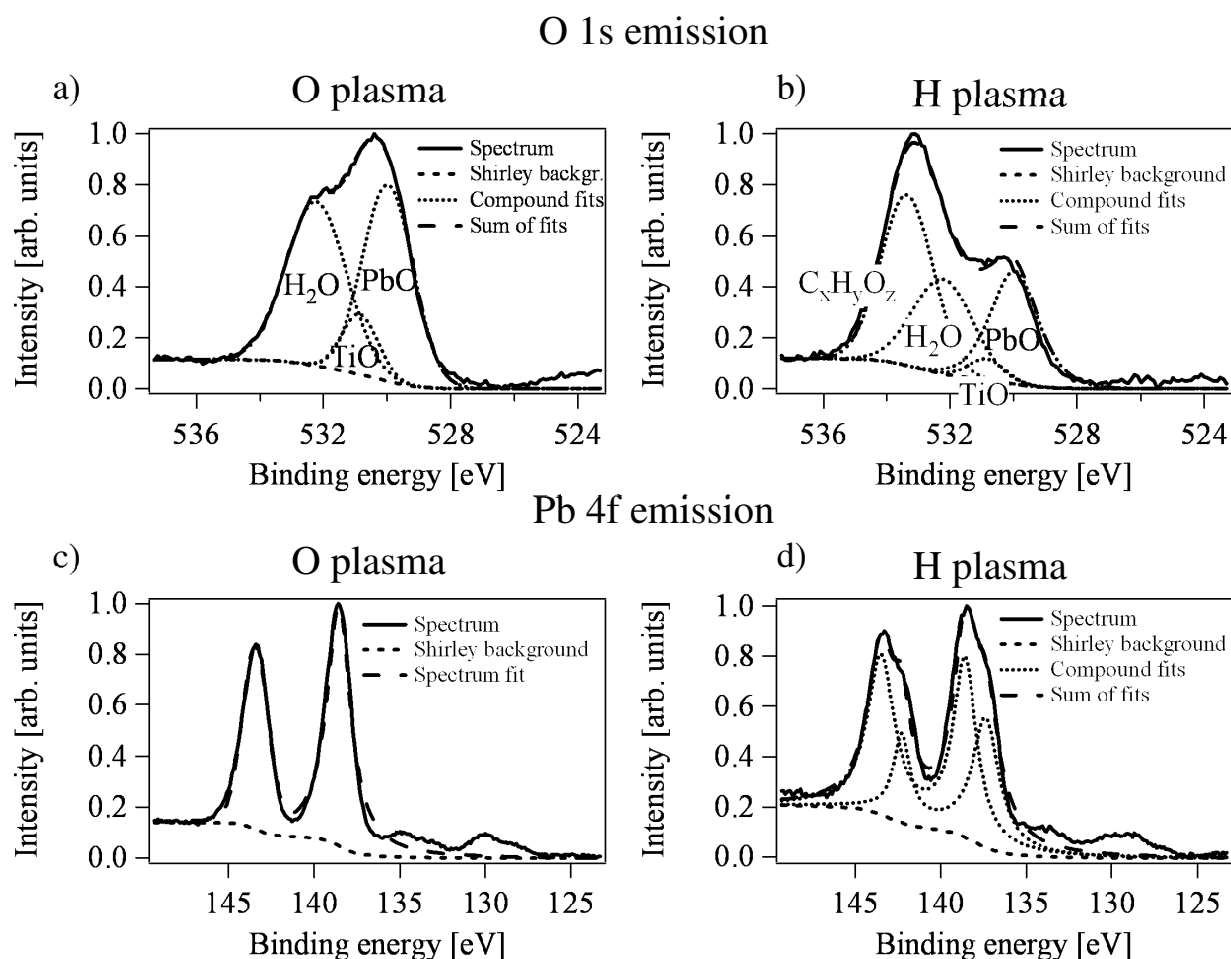


Figure 5.17: O 1s spectra of a PTO film after (a) an O plasma and (b) a H plasma. Pb 4f spectra of a PTO film after (c) an O plasma and (d) a H plasma.

The sample surface has then been further exposed to an H plasma ( 40 seconds). The corresponding O 1s and Pb 4f spectra are shown in Fig. 5.17b and d, respectively. The three above-mentioned O lines still exist after the H plasma but a new O species appears together with a new Pb species. The new O species has a binding energy similar to  $C_x-H_y-O_z$

compounds<sup>d</sup> [6]. The grazing angle measurements combined with the fact that the  $\text{C}_x\text{-H}_y\text{-O}_z$  compound is logically located at the sample surface (see below) permits to enhance the  $\text{C}_x\text{-H}_y\text{-O}_z$  contribution, creating a large photoelectron peak using a small quantity of O transferred from the first three O lines ( $\text{PbO}$ ,  $\text{TiO}_x$  and  $\text{H}_2\text{O}$ ).

The photoelectrons originating from the new Pb species are collected at a lower binding energy and correspond to less or unoxidized Pb (the O is maybe used in the  $\text{C}_x\text{-H}_y\text{-O}_z$  compounds). More surprisingly, if the sample is exposed again to an O plasma, both new O and Pb species disappear. The  $\text{C}_x\text{-H}_y\text{-O}_z$  compound reacts with the O plasma which in parallel reoxidizes the Pb. In fact, these *surface states* are reversible and can be easily switched many times using either O or H plasma without destroying the surface.

To confirm that these reactions take place only at the sample surface, Pb  $4f_{7/2}$  spectra are measured as a function of the polar angle along the (100)-plane, and plotted in Fig. 5.18a. The intensity variation of both Pb components as a function of the polar angle is reported in Fig. 5.18b<sup>e</sup>. It illustrates how the Pb  $4f_{7/2}$  peak intensity of the new Pb species increases with increasing the polar angle  $\theta$  while the opposite behavior happens for the Pb associated to the PTO. This behavior trivially indicates that the new Pb species is located at the surface of the PTO film. The very same behavior is observed for the new O species. Moreover, the new species Pb  $4f_{7/2}$  peak intensity does not reveal the presence of any forward focusing peaks along the (100)-plane, indicating a disordered environment.

### 5.5.5 Monodomain to polydomain transition in ferroelectric $\text{PbTiO}_3$ thin films on $\text{SrRuO}_3$ substrates.

The important role played by the effective screening length has been demonstrated in Section 5.4, in which the  $\lambda_{eff}$  values of exposed-to-air and O plasma cleaned surfaces have been obtained using an electrostatic model combining XPS and XPD measurements. XRD results found in Ref [5] suggest an SRO effective screening length  $\lambda_{eff}$  equal to  $0.23\text{\AA}$ , which is larger than for the Nb-STO ( $0.12\text{\AA}$ ), therefore leading to a poorer screening. What is the effect of this lower screening capacity on the PTO tetragonality or its core level position?

Here, we show measurements performed on a series of epitaxial c-axis oriented  $\text{PbTiO}_3$  perovskite films ( $246\text{\AA}$  to  $4\text{\AA}$  thick) grown onto metallic (001)  $\text{SrRuO}_3$  substrates, showing the evolution of the tetragonality and the PTO core level positions as a function of the film thickness, but also the PTO core levels positions as a function of the x-ray exposure time.

The value determined by means of XPD measurements performed on these samples are shown in Fig. 5.19. For the three thicker films, the appearance of a shoulder in the polar scan performed along the (100)-plane complicates the interpretation of the main forward focusing peak and tends to artificially reduce the  $(c/a)$ . This behavior has already been seen in some thick PTO films on Nb-STO and could stem from a relaxed cubic topmost layer. This interpretation is compatible with some multiple scattering results obtained using a cluster made of tetragonal

<sup>d</sup>Owing to its very small absorption cross section, a residual quantity of C could persist at the sample surface without a visible signature on the spectrum.

<sup>e</sup>The double peak is fitted using two gaussians to extract each individual contribution.

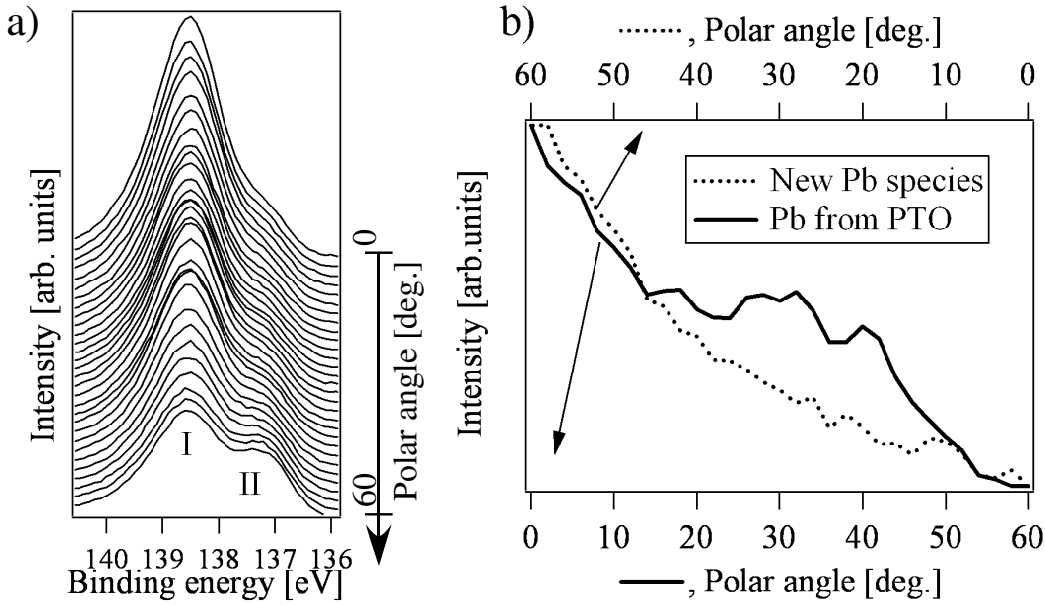


Figure 5.18: (a) Pb 4f<sub>7/2</sub> line spectra taken at different polar angles from 0 to 60° along the (100) crystallographic plane. The peaks labeled with I and II correspond to the Pb of the PTO and the new species respectively. (b) Intensity variation as a function of the polar angle for both Pb species contributions.

structures terminated by one or two cubic layers<sup>f</sup>.

For the thinner films, no such effect is observed and the tetragonality reduction with decreasing film thickness is comparable to the result found for the PTO on Nb-STO. However, the tetragonality obtained for the 4, 8, 13 and 29 Å thick films are always larger than expected. More surprisingly, the tetragonality of the 4 Å thick film, which is expected to be paraelectric, is much higher than the 1.02 value obtained for the PTO on Nb-STO.

In order to understand this behavior, an XPS investigation has been performed. In Fig. 5.20a, we show that the photoelectron kinetic energies change with the x-ray exposure time for a 77 Å thick film and that a stabilized regime is achieved after few hours. As seen in Fig. 5.20b, showing different spectra taken at grazing angle on a 29 Å thick film, the evolution of the core level position seems to be linked to a modification of the top electrode, which is *a priori* made of a randomly distributed layer of different oxide species such as OH, CO and H<sub>2</sub>O, labeled with I. We have observed that the oxide contamination layer is not affected by the vacuum environment, but by the x-ray exposure which acts like a smooth surface cleaning.

The Pb4f<sub>7/2</sub> and Ti2p<sub>3/2</sub> photoelectron kinetic energies have been reported as a function of the film thickness in Fig. 5.21a for the "freshly measured" case and after the saturation<sup>g</sup>. A drastic modification of the PTO photoelectron kinetic energies is observed after saturation indicating that the modification of the surface electrode can strongly modify the whole system.

<sup>f</sup>In the series used in Section 5.3 no similar shoulder has been observed.

<sup>g</sup>Note that the tetragonality has been measured in the saturated regime.

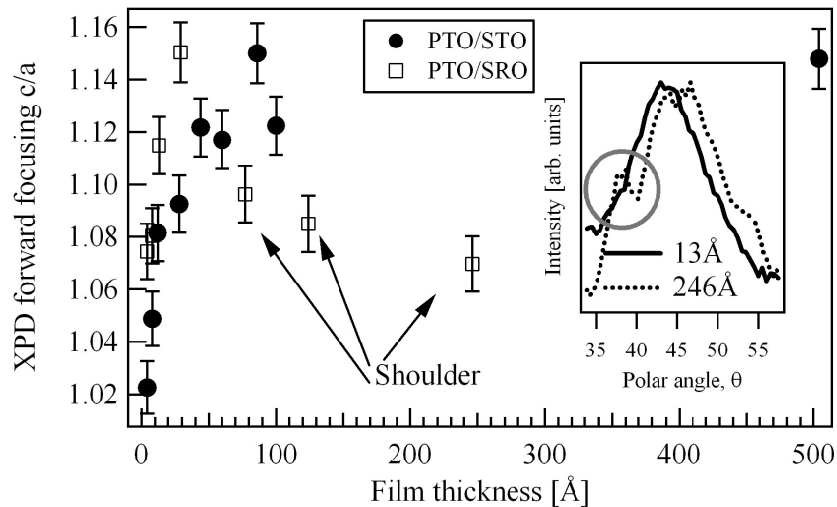


Figure 5.19: Tetragonality ( $c/a$  ratio) as a function of film thickness of  $\text{PbTiO}_3$  films grown on the  $\text{Nb-SrTiO}_3$  substrate (black disks) and the  $\text{SrRuO}_3$  substrate (open squares). Inset: Comparison of the main forward focusing along the (100)-plane for two film thicknesses.

In the case of the "freshly measured" photoelectron kinetic energies, the behavior of the  $E_{kin}$  is similar to the case of PTO on Nb-STO discussed in Section 5.4. However, after the soft cleaning performed by the x-ray exposure, the system exhibits the characteristics of a polydomain configuration.

Indeed, as discussed in Section 5.4, the surface cleaning can increase the effective screening length  $\lambda_{eff}$  (corresponding to a surface electrode screening capacity decrease) and can thus lead to an increase of the depolarizing field ( $E_{dep} \sim \lambda_{eff}$ ). In the case of insufficient screening, the system could undergo a monodomain to a polydomain transition in order to reduce the depolarizing field. This behavior has already been observed in ultrathin epitaxial  $\text{SrRuO}_3/\text{PbZr}_{0.2}\text{Ti}_{0.8}\text{O}_3/\text{SrRuO}_3/\text{SrTiO}_3$  heterostructures and is summarized in Fig. 5.21b [4].

For this heterostructure system, the polarization undergoes a transition from the bulk polarization value down to zero with decreasing thickness and, at the same time, the tetragonality remains very high for thin films. We observe the same behavior on the PTO/SRO sample series studied after few hours of x-ray exposure.

First, unusual high tetragonality values have been obtained for the thinner films compared to the previous results obtained for PTO/STO.

Second, for the saturated case, the photoelectron kinetic energy reduction, which can be associated to the polarization thanks to the electrostatic model exposed in Section 5.4, exhibit an unconventional behavior which could be divided into three parts. First, thick films (label 1 in Fig. 5.21) consist of a stable monodomain configuration perhaps insensitive to the x-ray induced cleaning. Note that a small reduction of the oxide contamination layer has also been measured in this case. For thinner films (label 2), the photoelectron kinetic energy is slightly reduced. The system is affected by the surface modification and the polarization decreases in response to the increasing depolarizing field. For the thinnest films (label 3), the system undergoes a mono- to

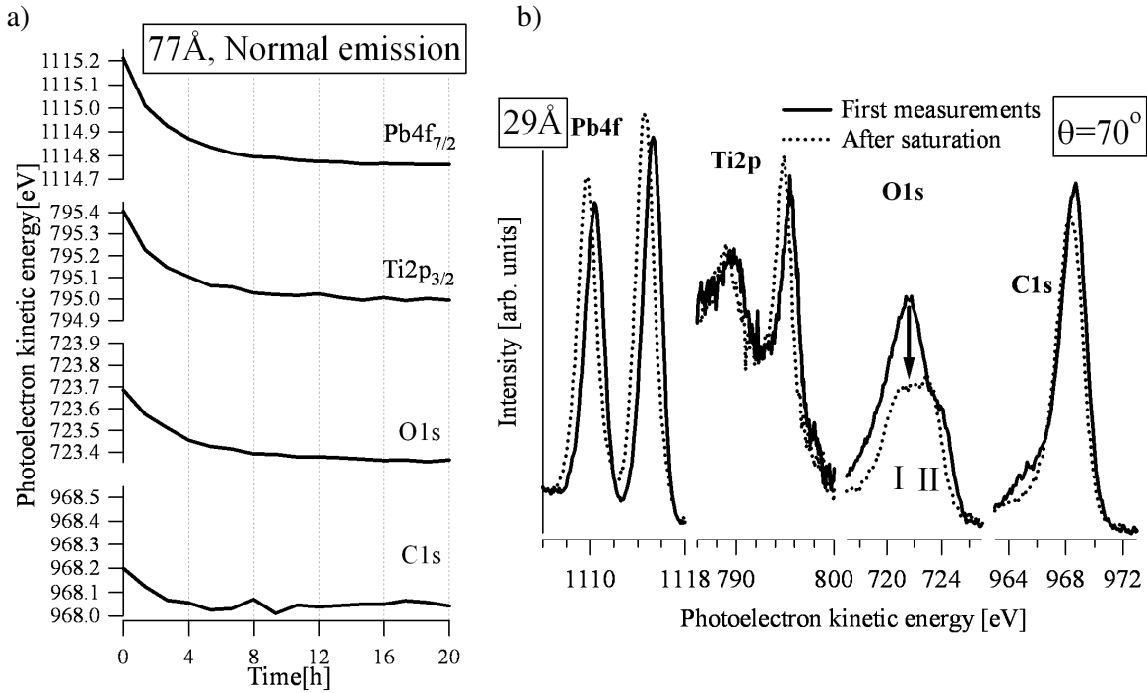


Figure 5.20: (a) Photoelectron kinetic energies as a function of the x-ray exposure time. The same scaling has been used for the different elements. (b) XPS spectra for a 29 Å thick film taken at a grazing angle, revealing a reduction of the O contained in the contamination layer (I). O emission from the PTO sample is labeled with II.

polydomain transition in order to reduce the depolarizing field and consequently the average polarization tends to zero. The reference value corresponding to a zero average polarization is given by the photoelectron kinetic energy of the freshly measured 4 Å thick film. All these similitudes suggest that the thinnest PTO/SRO films, after few hours of x-ray exposure, are in a polydomain configuration.

As all surfaces have been identically exposed-to-air, the only parameter which has changed between the PTO/STO and the PTO/SRO series is the substrate. However, the obtained results are drastically different. Indeed in the case of the PTO/STO, no such effect (cleaning with the x-ray exposure and a concomitant mono- to polydomain transition) has been observed, indicating that the substrate modification (variation of the interface effective screening length) has permitted to modify the film properties. It suggests also that we could be able to tune the film sensitivity to surface electrode modifications by modifying its interface  $\lambda_{eff}$  electrode. This can be done by either change the electrode material or perhaps by injecting additional charges (number of charge carriers).

### 5.5.6 How to obtain LEED patterns of PbTiO<sub>3</sub> surfaces?

As discussed in Chapter 4, it is possible to obtain LEED patterns on STO surfaces cleaned following various processes. However, cleaning PTO in order to obtain a LEED pattern is a

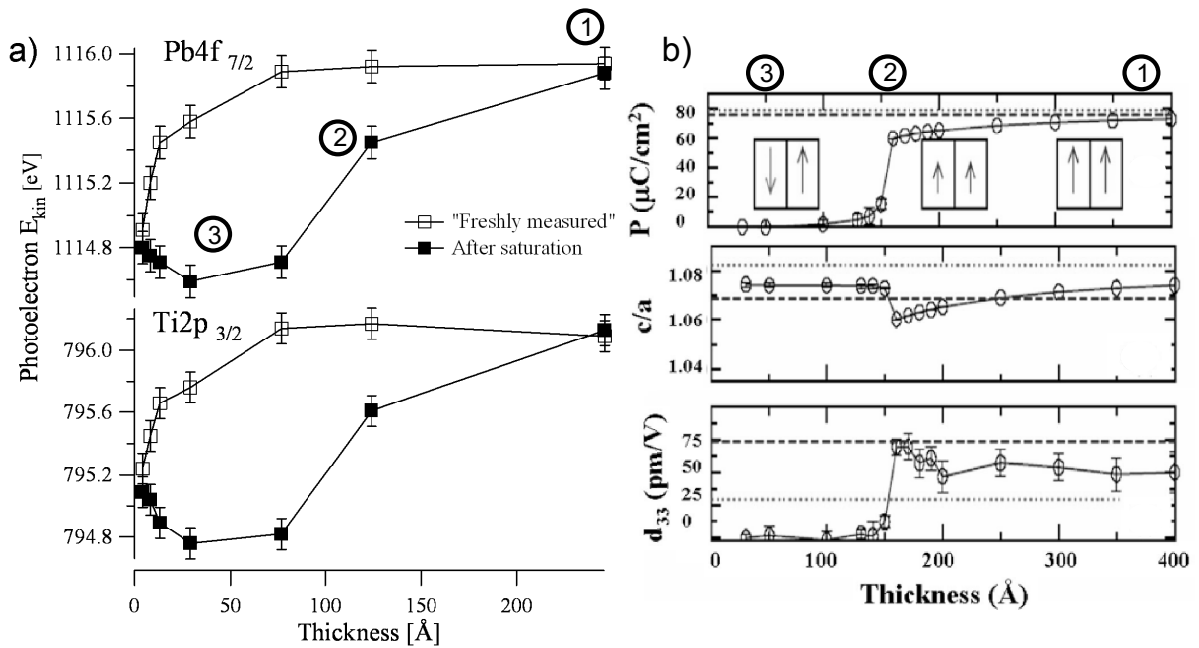


Figure 5.21: (a) Evolution of the  $\text{Pb}4f_{7/2}$  and  $\text{Ti}2p_{3/2}$  photoelectron kinetic energies as a function of the film thickness for freshly introduced samples (open squares) or after many hours of x-ray exposure (black squares). (b) Thickness dependence of the normal average polarization  $O$ , the tetragonality ( $c/a$ ), and the out-of-plane piezoelectric constant  $d_{33}$  at room temperature in ultrathin epitaxial  $\text{SrRuO}_3/\text{PbZr}_{0.2}\text{Ti}_{0.8}\text{O}_3/\text{SrRuO}_3/\text{SrTiO}_3$  heterostructures. The evolution of the domain structure from monodomain to polydomain is represented in the inset. This Figure was published in Ref. [4]. The unconventional behavior of the photoelectron kinetic energy could be divided into three parts as discussed in the text (labeled with (1), (2), (3)).

much more complex task. First of all, an O plasma is required to remove C contaminant from the PTO surface. Nevertheless, the surface O contaminant is still present after the O plasma which prevents the measurement of a LEED pattern.

A way to remove O surface contaminants is to heat the sample at a sufficiently high temperature which should stay lower than the Pb evaporation temperature. This heating process permits to remove O contaminants, but in parallel C is deposited onto the sample surface presumably owing to the degazing of the sample and its neighborhood. The application of O plasma/heating cycles is not sufficient to completely clean the surface.

However, the simultaneous application of an O plasma and heating permits to remove O and C contaminants at the same time<sup>h</sup>. The PTO XPS spectra before and after this treatment are shown in Fig. 5.22. The C atoms are entirely removed together with the O surface contaminant. After this surface cleaning, the sample is heated a few moments to get a LEED, as seen in Fig. 5.22e.

<sup>h</sup>Note that both direct (using the sample holder described in Section 4.3) and indirect (using a button-heater sample holder) heating can be used.

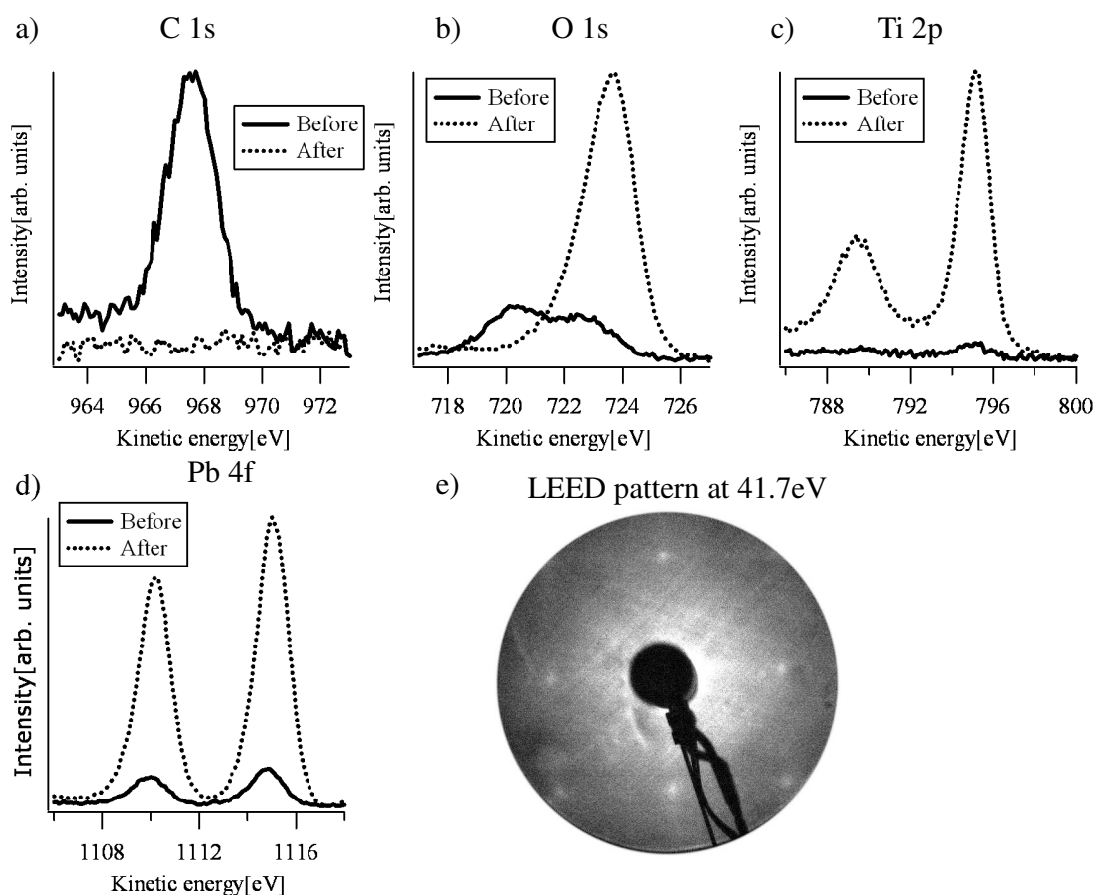


Figure 5.22: XPS spectra for (a) the C 1s, (b) O 1s, (c) Ti 2p and (d) Pb 4f emission lines together with the LEED pattern obtained after the cleaning procedure (e).

### References for section 5.5

- [1] M. Dawber, C. Lichtensteiger, M. Cantoni, M. Veithen, P. Ghosez, K. Johnston, K. M. Rabe and J.-M. Triscone, *Phys. Rev. Lett.* **95**, 177601 (2005).
- [2] D. A. Tenne, A. Bruchhausen, N. D. Lanzillotti-Kimura, A. Fainstein, R. S. Katiyar, A. Cantarero, A. Soukiassian, V. Vaithyanathan, J. H. Haeni, W. Tian, D. G. Schlom, K. J. Choi, D. M. Kim, C. B. Eom, H. P. Sun, X. Q. Pan, Y. L. Li, L. Q. Chen, Q. X. Jia, S. M. Nakhmanson, K. M. Rabe and X. X. Xi, *Science* **313**, 614 (2006).
- [3] C. Lichtensteiger, M. Dawber, N. Stucki, J. B. Yau, J. Hoffman, L. Despont, P. Aebi, C. Ahn and J.-M. Triscone, *Appl. Phys. Lett.* **90**, 052907 (2007).
- [4] V. Nagarajan, J. Junquera, J. Q. He, C. L. Jia, R. Waser, K. Lee, Y. Kim, S. Baik, T. Zhao, R. Ramesh, Ph. Ghosez and K. M. Rabe, *J. Appl. Phys.* **100**, 051609 (2006)
- [5] C. Lichtensteiger, PhD thesis, 2006

[6] <http://www.lasurface.com>



## 5.6 Antiferrodistortive distortion at the (001) PbTiO<sub>3</sub> surface

### 5.6.1 Basic notions

The antiferrodistortive (AFD) instability consists of an in-plane rotation of the O octahedral cage surrounding the Ti atom. In the previous XPD studies presented in Section 5.2 and 5.3, the calculations were performed using only out-of-plane (along the  $z$ -axis) ferroelectric distortions but a variety of reconstructed surfaces have been observed under different growth conditions. For example, using grazing incidence x-ray scattering, Munkholm *et al.* have shown that a  $c(2\times 2)$  AFD reconstruction can be obtained at the (001) PTO surface by an annealing at 875 to 1025K under most of the PbO partial pressures while a  $(1\times 6)$  surface occurs for low PbO partial pressures. They also found, a  $10^\circ$  in-plane rotation of the O cage surrounding the Ti atoms [2].

AFD does not occur in bulk PTO as it is suppressed by the out-of-plane polar distortion. However, *ab-initio* calculations performed by Bungaro and Rabe show that near a PbO-terminated surface, the ferroelectric distortion does not prevent the AFD distortion [1].

Here MSC calculations coupled to an R-factor analysis have been performed to check whether the XPD measurements are sensitive to such an  $c(2\times 2)$  AFD reconstruction.

### 5.6.2 MSC analysis

The possible presence of an AFD distortion in the 20Å thick PTO film has been investigated including in-plane and out-of-plane O atom shifts in the optimized MSC calculation parameter set obtained in Sec. 5.3.

The Fig. 5.23a and b show two R-factor grids which quantify the agreement between the O1s emission of a 20Å thick PTO film and different MSC calculations with various AFD distortions. The AFD is simply included in the calculation via the modification of the O atom positions within the cluster. To obtain an as complete as possible study of the AFD distortion influence on XPD patterns, not only the in-plane ( horizontal O shift) but also the out-of-plane ( vertical O shift) AFD distortion is considered, as shown in Fig. 5.23c. In Fig. 5.23a, all O atoms of the vertical PbO plane (marked with a cross in Fig. 5.23d) contained in the cluster are shifted relative to their initial (0, 0) centro-symmetric position while in Fig. 5.23b, only the topmost layer encounters an AFD<sup>i</sup>. The region below (above) the horizontal dotted white line in R-factor grids corresponds to O up-state (down-state) distortions.

In both cases, a minimum is clearly obtained for O atoms shifted down (up-state distortion), which is equivalent to the result obtained in Section 5.3 without AFD distortion. Nevertheless, R-factor values are globally smaller in the case of a unique AFD distorted topmost layer (Fig. 5.23b). In this latter case, the calculations are compatible with the presence of an horizontal O

---

<sup>i</sup>Munkholm *et al.* have found, using *in situ* x-ray scattering measurements of PTO in equilibrium with PbO vapor, that only the first topmost layer experiences an AFD distortion [2]

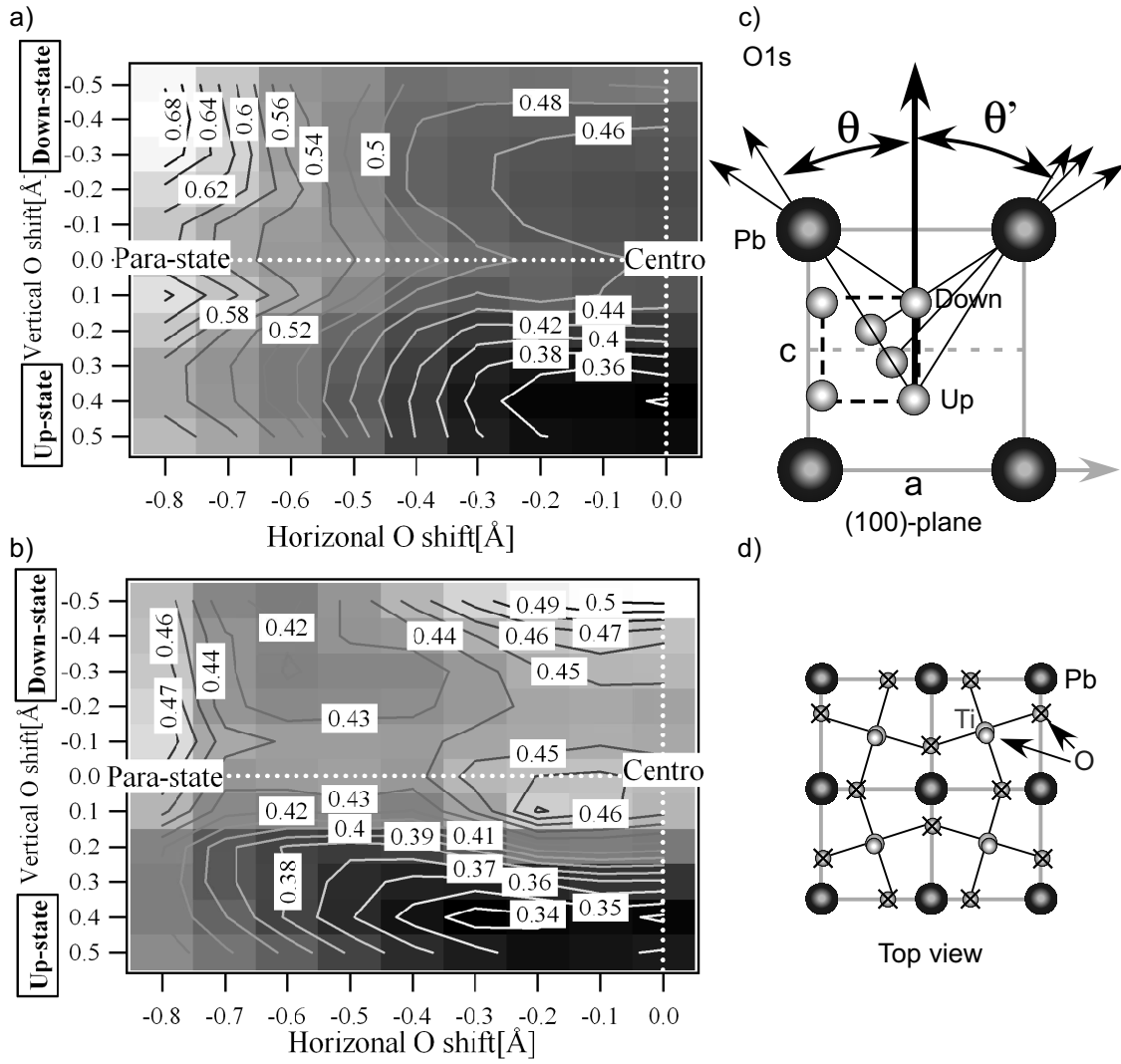


Figure 5.23: Two different R-factor grids calculated for a 20 Å -thick PTO film and different MSC calculations obtained by varying the position of (a) all O atoms of vertical PbO (100) planes contained in the cluster, and (b) O atoms of the topmost layer only. The other atoms remain fixed. (c) Side view: cut along the (100) plane. (d) Top view: only the first PbO and TiO layers are shown. Only O atoms marked with a cross are moved. O atoms on top of Ti remain fixed.

shift up to  $\approx 0.3\text{Å}$ , similar to the result obtained by Munkholm who has found an horizontal O shift of  $\approx 0.35\text{Å}$  using *in situ* x-ray scattering measurements. Moreover, the horizontal O atom shift is coupled to a progressively small reduction of the vertical O shift corresponding to a reduction of the out-of-plane ferroelectric polar distortion as seen in Fig. 5.23b.

The same low R-factor values ( $\approx 0.34$ ) are obtained for both the case with and without AFD. It is thus not possible to insure the presence of an AFD in the studied 20 Å thick PTO film. As both cases are compatible with our XPD measurements, it shows the limitation of the XPD measurements to reveal such distortions.

**References for section 5.6**

- [1] C. Bungaro and K. M. Rabe, Phys. Rev. B **71**, 035420 (2005).
- [2] A. Munkholm, S. K. Streiffer, M. V. Ramana Murty, J. A. Eastman, C. Thompson, O. Auciello, L. Thompson, J. F. Moore and G. B. Stephenson, Phys. Rev. Lett. **88**, 016101-1 (2002).
- [3] M. Sepiarsky, M. Stachiotti, and R. L. Migoni, Phys. Rev. B **72**, 014110 (2005).



# Chapter 6

## Conclusions and future perspectives

### Conclusions

The main goal of this work was to investigate the ferroelectricity in very thin films. We show how different parameters, such as the film thickness or the electric boundary conditions, can influence the properties of ferroelectric materials.

First of all the Nb-SrTiO<sub>3</sub> substrate has been studied by means of XPD measurements together with a MSC analysis, showing that its surface exhibits an unexpected polar distortion. Then, different cleaning approaches have been used to obtain a (1×1) surface reconstruction. Using XPS measurements, we show that the surface chemical state may be completely different even with the same atomic surface reconstruction (measured by LEED). As the surface chemistry is not inevitably correlated to the surface reconstruction, it should be analysed before the growth process to have a complete control of the substrate preparation.

XPD measurements performed on PbTiO<sub>3</sub> films show that films of only three unit cells thick are still ferroelectric and that atomic relaxation and rumpling are paramount for thinner films. The asymmetry makes the films polar but probably not switchable. Instead of a sharp ferroelectric-paraelectric transition, a gradual change of the ferroelectric polar distortion was measured as the film thickness was decreased.

We have then presented our XPD and XPS results obtained on PbTiO<sub>3</sub> epitaxial films with different electrical boundary conditions, using XPD and XPS. A key parameter for understanding ferroelectricity in thin films, the effective screening length, has been probed by means of photoemission, permitting the experimental determination of the screening properties of the top electrode. We have also demonstrated a change of the effective screening length upon cleaning of the thin film surface.

The decrease of the tetragonality was also measured in thin PbTiO<sub>3</sub> films grown on La<sub>0.67</sub>Sr<sub>0.33</sub>MnO<sub>3</sub> or SrRuO<sub>3</sub>. However, in the latter case, the measured values of  $c/a$  were surprisingly higher than expected for the thinner films. This result together with XPS measurements have suggested the transition of a monodomain to a polydomain configuration when the film thickness is reduced.

We have also shown that a surface treatment combining an oxygen plasma together with an annealing leads to a LEED pattern on a  $\text{PbTiO}_3$  surface. Then by exposing the surface to an oxygen/hydrogen plasma, we have been able to reoxidize/desoxidize the Pb surface species and at the same time to remove/create new O surface compounds, in a reversible way.

Finally, in order to validate some results found in XPD investigations, simulations of the photoelectron diffraction process have been used. In this work, the EDAC code, adopting a cluster approach, has been studied, tested and used for many systems, including different crystal symmetries, kinds of atoms or photoelectron kinetic energies. Despite some limitations, the EDAC code furnishes much more satisfying results than the standard SSC approach but to the detriment of the computation time, making this approach essential but highly time-consuming.

### Future perspectives

Based on the results and the observations done during this work, different measurements on perovskite oxides could certainly contribute to increase the knowledge on ferroelectric materials.

First, as the PTO cleaning procedure becomes well controlled, we can easily imagine to perform a state-of-the-art ARPES investigation which could furnish interesting information.

Second, the discussed effect of the electron shower, which seems to play a major role in the ferroelectric polarization switching, could be confirmed by performing the measurements using an x-ray source without  $e^-$  creation, for instance synchrotron radiation.

Third, in order to stabilize and measure a initial down state configuration, we can try either to reduce the atom mobility by measuring at low temperature, or to employ other substrates.

Fourth, as it has been shown, the effective screening length of the PTO/SRO surface electrode is modified by a simple x-ray exposure which seems to act, in this case, like a very smooth cleaning. This cleaning, which has affected the surface electrode, has drastically changed the core level positions of the ferroelectric film emitters. We could thus optimize the surface conditions to allow ferroelectricity in increasingly thin films, by depositing very thin metallic electrodes or polar electrodes made of water for instance. In addition, we can imagine to utilize the response of the ferroelectric film to surface contaminants as a detection method.

# Appendix A

## MSC shell script example

Here is a simplified input file used for the optimization procedure described in Section 3.2. In this example, only the  $R_{max}$ ,  $l_{max}$ , Debye temperature and inelastic mean free path values are changed in order to get the best R-factor value. Obviously, as already discussed, other parameters as  $d_{max}$ , the number of emitters or even the atom position can also be varied using the same structure described in this input file. Different existing or new programs are used within this input file. Moreover, additional inputs are required. The Table A.1 shows how these programs are related.

Program	Required input files	Output files
<b>edac_2geo_Td.exe</b>	edac-input.txt Cluster.in	edac-ouput.txt
<b>interpolation.exe</b>	polardirections.in edac-ouput.txt	edac-map.txt
<b>rfactor.exe</b>	experiment.itp edac-map.txt(tpi) LinCombSSCs.in	rfactor.txt
<b>RfactMinLoc.exe</b>	rfactor.txt stuff.txt	Status-check.out

Table A.1: Programs and files created and/or required during the optimization procedure.

```
#Initialization of the R-factor matrix and Status files
echo "Rmax Lmax DebyeTemp Imfp Rfactor" > R-factor.out
echo "STATUS CHECK" > Status-check.out
calc-nbr=0
index=0
level=0

# This defines the range of imfp to be analyzed.
for ((m=4 ; m<=15; m++ ))
do
```

```

# This defines the range of Debye temperatures to be analyzed: 25+$k*25
for ((k=0 ; k<=7; k++ ))
do
# This defines the range of Rmax to be analyzed.
for ((i=19 ; i<=22; i++ ))
do
#This defines the range of Lmax to be analyzed.
for ((j=7 ; j<=14 ; j++ ))
do
if [ $level -eq 0 ]
then
if [ $index -eq 0 ]
then
echo "Level 0 (Rmax and Lmax)" >> Status-check.out
echo "Ncal Rm-min Lm-min Rfactor-min " >> Status-check.out
index=1
fi
Rm='echo $i | bc'    Scan Rmax values
Lm='echo $j | bc'    Scan lmax values
DT-Cu=50    Fix the Debye temperature
Imfp=11    Fix the inelastic mean free path
fi
if [ $level -eq 1 ]
then
if [ $index -eq 1 ]
then
echo "Level 1 (Debye temperature for Cu)" >> Status-check.out
echo "Ncal DT-Cu-min Rfactor-min" >> Status-check.out
index=2
fi
Rm=$Rm-min    Fix the Rmax and lmax using the values obtained for the minimal
R-factor value. This (Rmax,Lmax)min set is found using ./RfactMinLoc.exe
Lm=$Lm-min
DT-Cu='echo 25 + $k 25 | bc'    Scan Debye temperatures
Imfp=11    Fix the inelastic mean free path
fi

if [ $level -eq 2 ]
then
if [ $index -eq 2 ]
then
echo "Level 2 (Inelastic mean free path)" >> Status-check.out
echo "Ncal Imfp-min Rfactor-min" >> Status-check.out
index=3
fi

```

```

Rm= $Rm-min
Lm=$Lm-min
DT-Cu=$TD-Cu-min
Imfp='echo $m | bc'   Scan the inelastic mean free path
fi

#This counts the number of calculations.
calc-nbr='echo $calc-nbr + 1 | bc'
#This prepares the input file using an existing cluster Cluster.in.
echo "verbose off" > edac-input.txt
echo "clear cluster" >> edac-input.txt
echo "cluster surface on" >> edac-input.txt
echo "cluster reference-point l(A) 0 0 0" >> edac-input.txt
echo "cluster Rmax l(A) $Rm" >> edac-input.txt
echo "cluster input Cluster.in" >> edac-input.txt
echo "cluster natoms 16504" >> edac-input.txt
echo "dmax l(A) 15" >> edac-input.txt
echo "emitters 9 l(A) 0 0 0 Cu 0.738 1.278 -2.087 Cu 1.476 0 -4.174 Cu 0 0 -6.261 Cu 0.738
1.278 -8.348 Cu 1.476 0 -10.435 Cu 0 0 -12.522 Cu 0.738 1.278 -14.609 Cu 1.476 0 -16.697 Cu"
>> edac-input.txt
echo "initial state 2p" >> edac-input.txt
echo "movable cluster" >> edac-input.txt
echo "beta 54" >> edac-input.txt
echo "emission energy E(eV) 807.2 807.2 1" >> edac-input.txt
echo "emission angle theta 0 90 46" >> edac-input.txt
echo "emission angle phi 0 360 360" >> edac-input.txt
echo "V0 E(eV) 13.5" >> edac-input.txt
echo "cluster surface l(A) 2.3" >> edac-input.txt
echo "imfp inline 1 l(A) $Imfp" >> edac-input.txt
echo "lmax $Lm" >> edac-input.txt
echo "iteration recursion" >> edac-input.txt
echo "orders 1 9" >> edac-input.txt
echo "muffin-tin" >> edac-input.txt
echo "temperature-T 300" >> edac-input.txt
echo "polarization LPx" >> edac-input.txt
echo "Debye-temperature Cu $DT-Cu" >> edac-input.txt
echo "muffin-tin" >> edac-input.txt
echo "scan pd edac-output.txt" >> edac-input.txt
echo "report natoms" >> edac-input.txt
echo "end" >> edac-input.txt
./edac_2geo_Td.exe edac-input.txt

#This interpolates edacoutput onto the angles of polardirections.in.
./interpolation.exe edac-output.txt edac-map.txt polardirections.in
cp edac-map.txt edacCuRm='echo $Rm'Lm='echo $Lm'DTCu='echo $DT-Cu'Im='echo

```

\$Imfp-9em.out

*#This calculates the R-factor value using the experiment.itp and the edac-map.txt files. Note that both files contain the same angles defined by polardirections.in.*

*#The LinCombSSCs.in is required.*

**./rfactor.exe**

rGBD='cat rfactor.txt'

echo "\$Rm \$Lm \$DT-Cu \$Imfp \$rGBD" >> R-factor.out

if [ \$level -eq 0 ]

then

echo "\$rGBD \$Rm \$Lm" >> stuff.txt

**./RfactMinLoc.exe**

Rm-min='cat x1val.txt'

Lm-min='cat x2val.txt'

Rfactor-min='cat xvalmin.txt'

echo "\$calc-nbr \$Rm-min \$Lm-min \$Rfactor-min" >> Status-check.out

fi

if [ \$level -eq 1 ]

then

echo "\$rGBD \$DT-Cu 0" >> stuff.txt

**./RfactMinLoc.exe**

DT-Cu-min='cat x1val.txt'

Rfactor-min='cat xvalmin.txt'

echo "\$calc-nbr \$DT-Cu-min \$Rfactor-min" >> Status-check.out

fi

if [ \$level -eq 2 ]

then

echo "\$rGBD \$Imfp 0" >> stuff.txt

**./RfactMinLoc.exe**

Imfp-min='cat x1val.txt'

Rfactor-min='cat xvalmin.txt'

echo "\$calc-nbr \$Imfp-min \$Rfactor-min" >> Status-check.out

fi

echo "now we do the next"

done

done

level=1

done

level=2

done

## Appendix B

# MSC calculated diffraction patterns for Cu(111) surface

The three following figures correspond to the MSC calculations obtained using the EDAC code applied on the well-known Cu(111) surface and largely discussed in Section 3.3.

They show how the  $l_{max}$  parameter strongly influences the diffraction pattern and that, in this case at least, the MSC calculations seem to be insensitive to the  $R_{max}$  value modification. Note that it is far from being the case for every systems. Moreover the calculations show that a  $d_{max}$  value can strongly affect the diffraction pattern, specially for small  $l_{max}$  values.

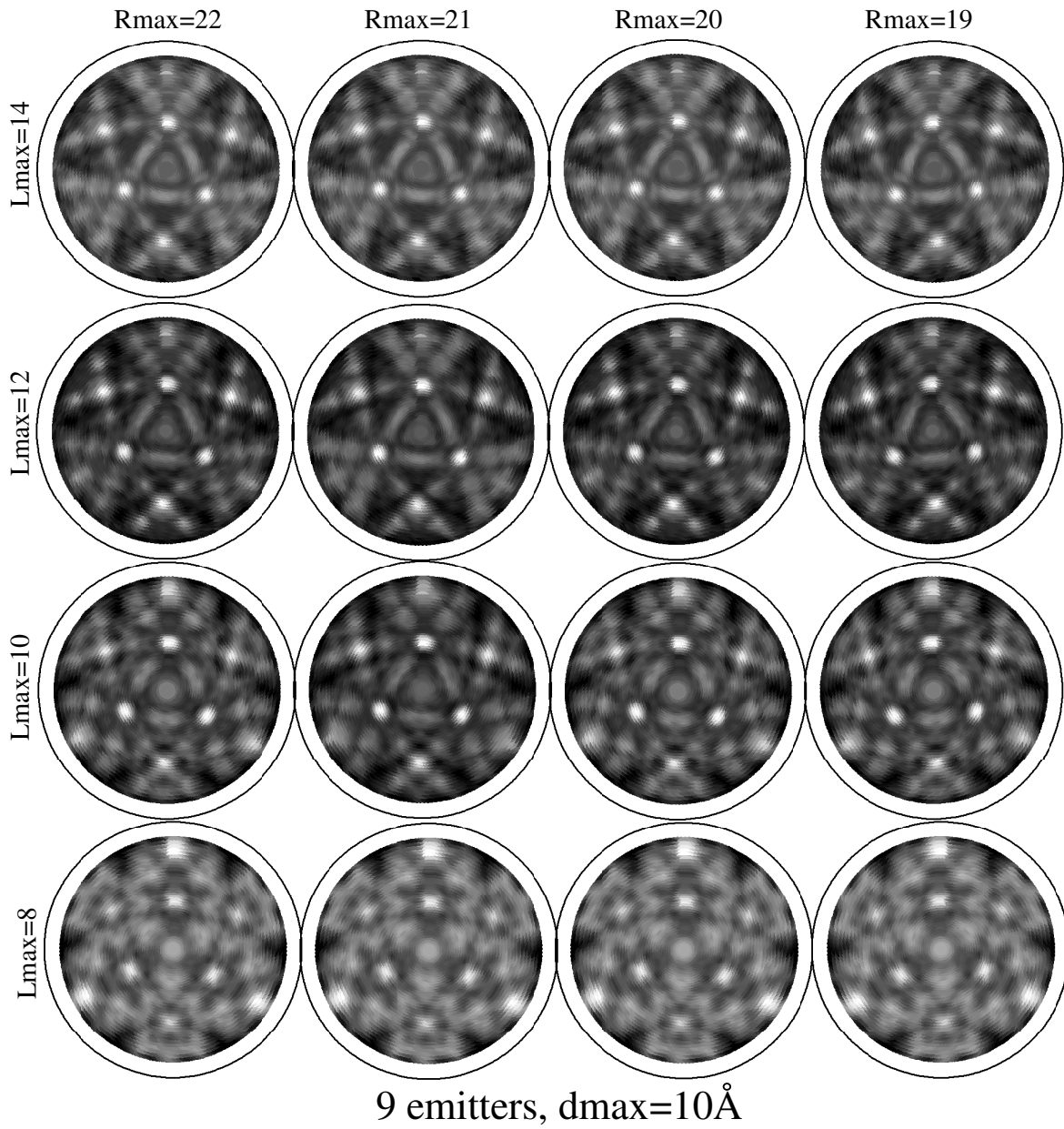


Figure B.1: Different MSC calculations for 9 emitters, Debye temperature=50K,  $imfp=11\text{\AA}$ ,  $d_{max}=10\text{\AA}$  and various  $R_{max}$ ,  $l_{max}$ . There are used for the R-factor grid plotted in Fig. 3.2a.

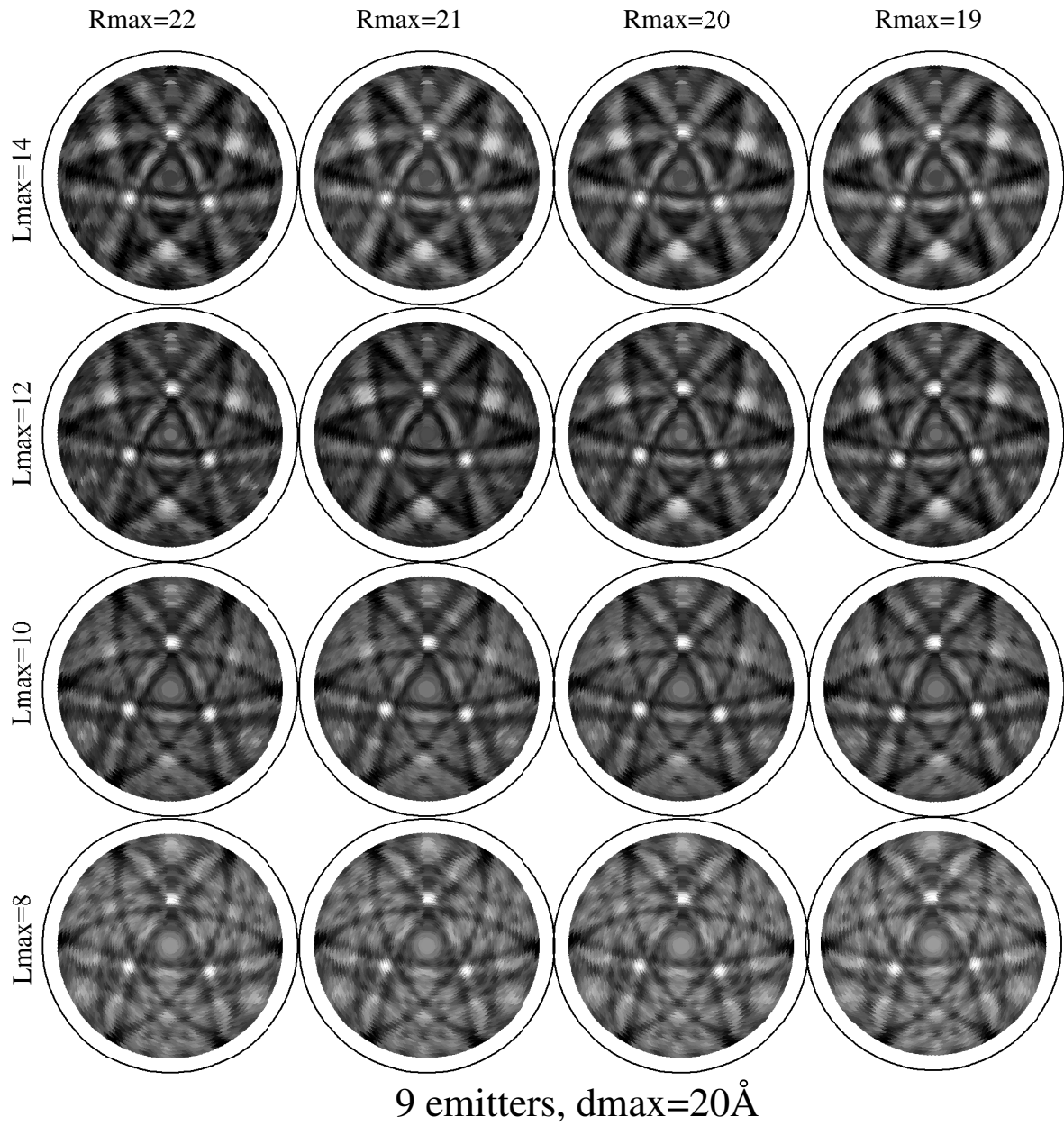
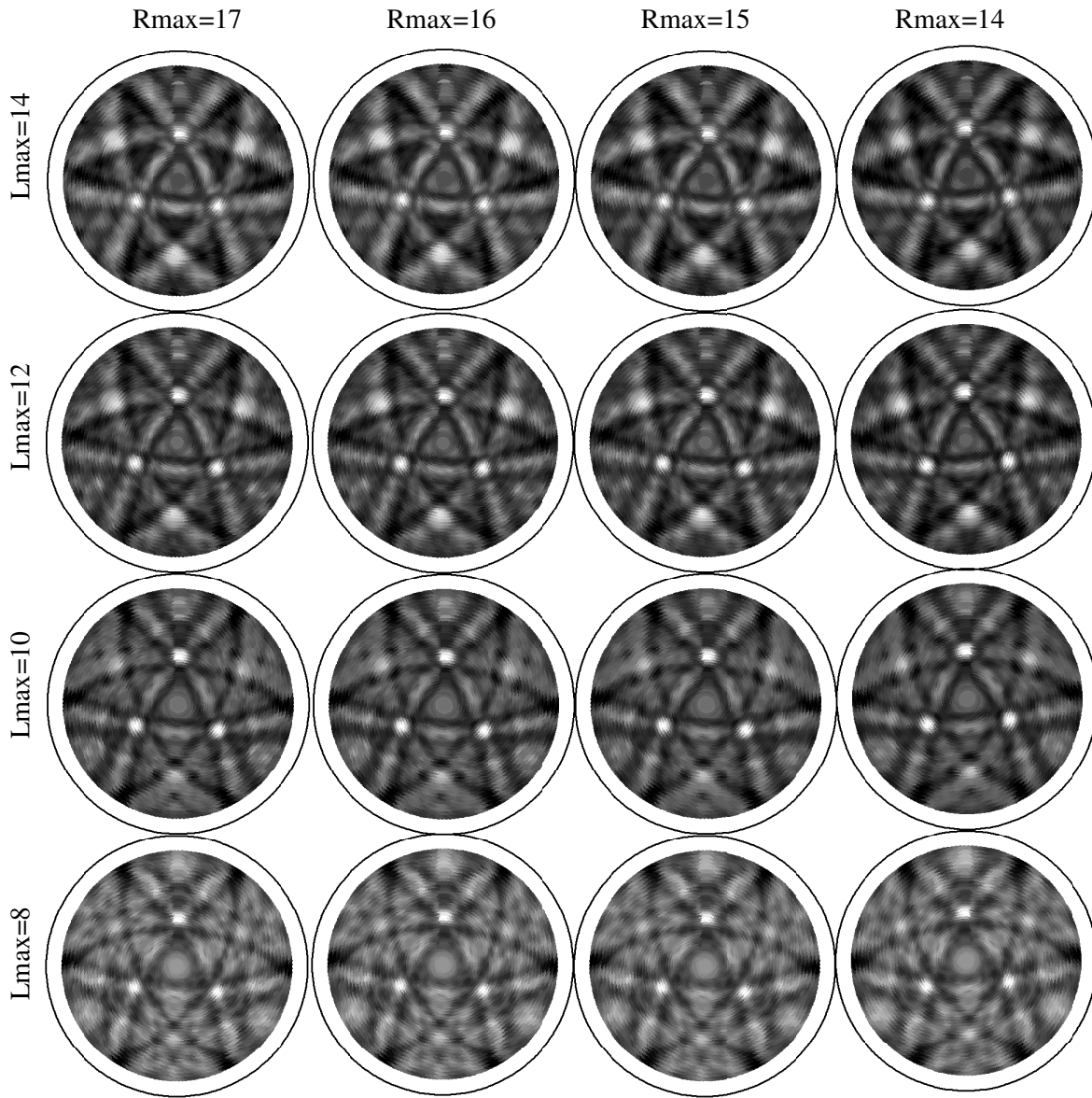


Figure B.2: Different MSC calculations for 9 emitters, Debye temperature=50K,  $imfp=11\text{\AA}$   $d_{max}=20\text{\AA}$  and various  $R_{max}$ ,  $l_{max}$ . There are used for the R-factor grid plotted in Fig. 3.2c.



6 emitters, “unlimited”  $d_{max}$

Figure B.3: Different MSC calculations for 9 emitters, Debye temperature=50K,  $imfp=11\text{\AA}$  ”unlimited”  $d_{max}$  and various  $R_{max}$ ,  $l_{max}$ . There are used for the R-factor grid plotted in Fig. 3.2e.





# Appendix D

## Plasma characterization

With the collaboration of Dr. M.G. Garnier.

### D.1 Introduction

The plasma can be employed as a soft cleaning procedure of *ex situ* prepared samples. It is based on the ion chemical reactivity instead of the ion mechanical sputtering. It can also be used for enhancing field emission from carbon nanotubes [1], for smoothing semiconductor surfaces [2], for influencing the oxygen content in thin oxide films or for preparing hydride films, and so on.

It appears necessary to have the smallest possible ion kinetic energy in order not to destroy the sample surface structure. Different measurements have shown that samples exhibiting LEED patterns have been destroyed (no LEED) using not adapted plasma parameters corresponding to too high ion kinetic energies. The ion kinetic energy minimization is thus a prerequisite for an efficient and soft cleaning. The plasma calibration is done using an homemade ion analyzer designed for measuring the ion kinetic energy at the sample position.

### D.2 How the ion analyzer works and how to calibrate the plasma

The ion analyzer is illustrated in Fig. D.1. It is made of three grids (in gray) separated from each other by insulators, inside a grounded shield. The first grid (labeled with q) corresponds to the sample surface. With this configuration, it is investigate the behavior of a grounded, biased or floating sample. When the plasma is started, the ions are first decelerated by the  $+V_{grid}$  electrode (2) and then accelerated by the -80V electrode (3). The electrons are decelerated by the third grid in such a way that only the ion current is measured at the end. Only the ions with a sufficiently large kinetic energy are thus collected. The current  $I_c$ , created by the ions achieving the electrode 3, is then measured as a function of the grid voltage  $V_{grid}$ , as shown in

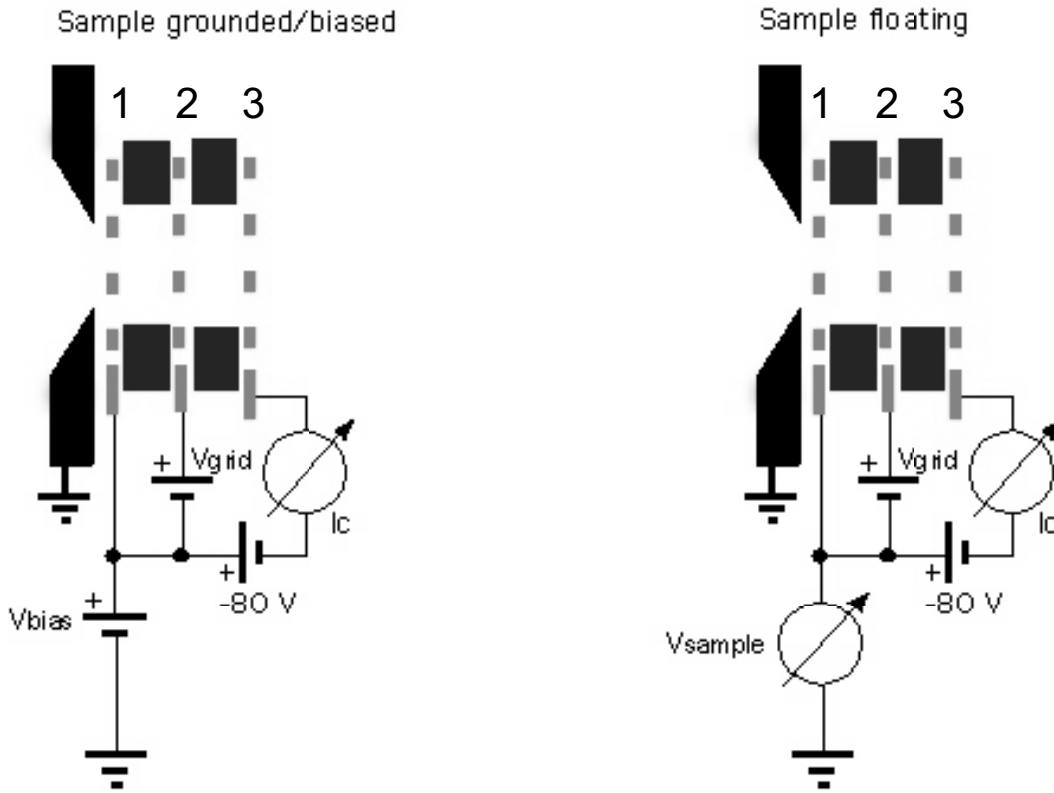


Figure D.1: Electrostatic analyzer simulating the sample holder.

Fig. D.2a. The average ion kinetic energy is given by the minimum of the  $dI_c/dV_{grid}$  derivative (Fig. D.2b).

### D.3 Results and discussion

For one given gas (argon, oxygen and hydrogen for instance), the plasma properties can be modified using different gas pressures, microwave power while the sample conditions depend on the distance to the plasma antenna, or its potential: grounded, biased or floating. An overview of the influence of all these parameters on the ion kinetic energy is given in Table D.1.

It is possible to decrease the ion kinetic energy by decreasing the microwave power or by increasing the gas pressure, but to the detriment of the "peak shape" (whatever it means for the ions). It is also possible to decrease the ion kinetic energy by applying a positive bias to the sample, but in this case the kinetic energy of neutral atoms will be unaffected making this kinetic energy minimization approach less meaningful. We will thus focus our attention to the microwave power and the gas pressure.

To get a minimal ion kinetic energy it is necessary to float the sample, and to monitor the potential on the sample, which encounters a drastic change when the microwave power is varying. The microwave power which corresponds to the minimal ion kinetic energy is slightly

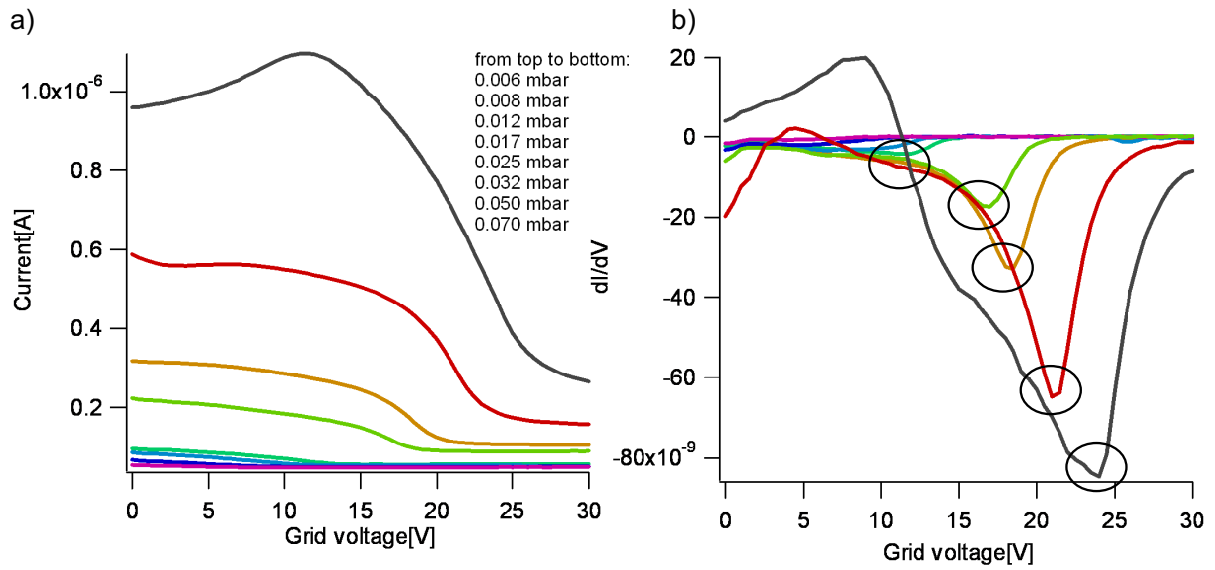


Figure D.2: (a) The measured current  $I_c$  as a function of the grid voltage  $V_{grid}$  for increasing Ar gas pressure and (b) its derivative  $dI_c/dV_{grid}$  for a grounded system.

Plasma change	Effects	Comments
Gas pressure ↗	$E_{kin}^{ion}$ ↘ $N^{ion}$ ↘	The ions encounters more collisions reducing their kinetic energy. The effect is weaker for floating than for grounded samples.
Microwave power ↘	$E_{kin}^{ion}$ ↘	The effect is weaker for floating than for grounded samples.
Time ↘	$E_{kin}^{ion}$ ↗	Probably due to parts of the plasma source that are heating.
Plasma source with grid and floating sample	$E_{kin}^{ion} \approx$ without grid but with grounded sample	The plasma does not seem to see the floating sample behind the grid.
Sample change	Effects	Comments
Distance ↗	$E_{kin}^{ion}$ ↘	Ions are faster near the antenna.
Bias ↗	$E_{kin}^{ion}$ ↘	The ions are decelerated by the bias.

Table D.1: Summary of the ion kinetic energy dependences.

above this abrupt change. The sample voltage depends also on the gas pressure and it appears that the ideal gas pressure to reduce the ion kinetic energy occurs when this voltage is the largest. The reflected power plays also an important role. An elegant way to find the "real" 0 W reflected power is to adjust the impedance adapter to obtain the maximal sample voltage.

To summarize, to get the minimal ion kinetic energy,

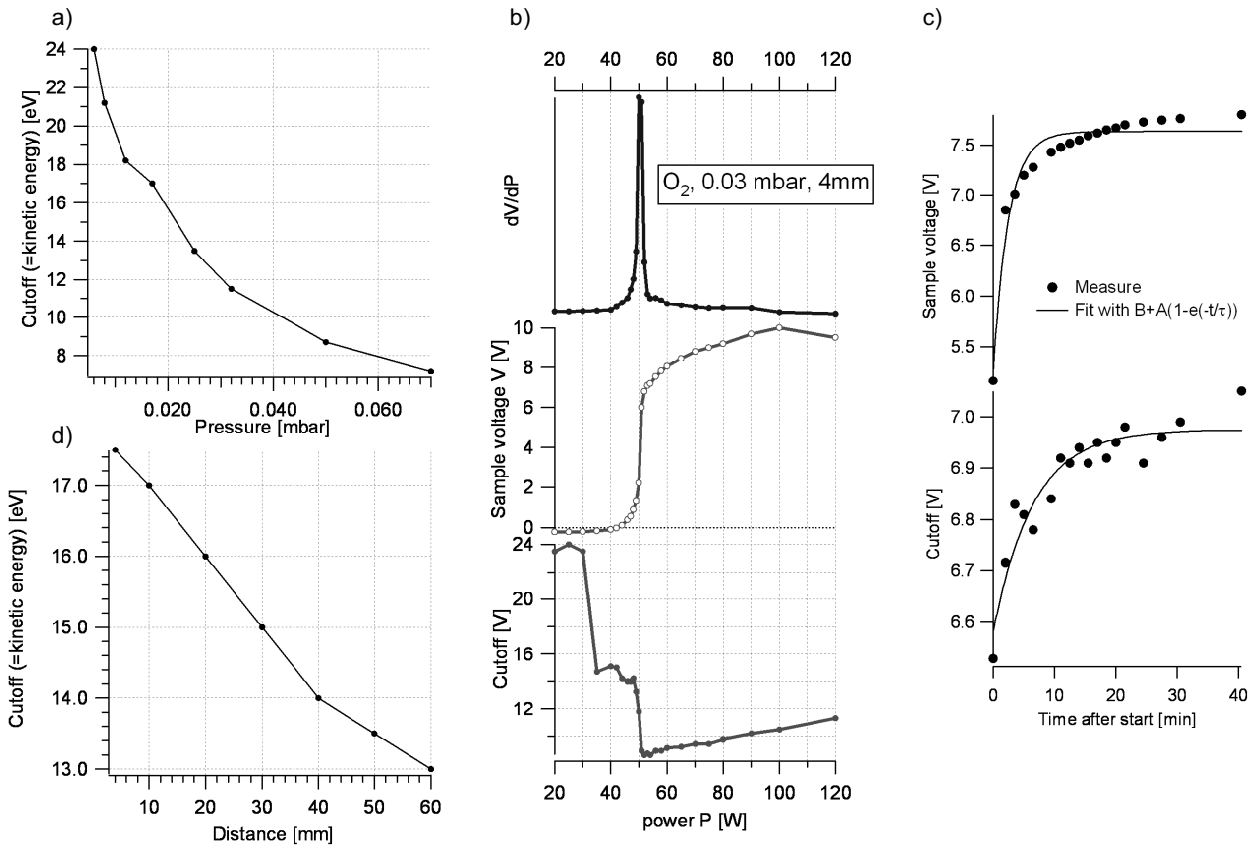


Figure D.3: For a floating sample in an oxygen plasma. (a) Cutoff vs pressure. (b) Sample voltage, its derivative and the deduced cutoff as a function of the microwave power. (c) Sample voltage and cutoff as a function of the elapsed time. (d) Cutoff vs the antenna-sample distance.

- Adjust the impedance adapter to obtain the maximal sample voltage. It corresponds to the real 0W reflected power.
- Scan the microwave power and measure the sample voltage. Find the cutoff and choose a power "slightly" higher.
- Scan the pressure to maximize the sample voltage.

Finally, a summary of the plasma parameters corresponding to the lowest ion kinetic energies is reported in Table D.2 with a precision of  $\pm 1\text{eV}$ . Note that without plasma parameter optimization, ion kinetic energies higher than 20eV are not surprising.

Gas and pressure	Microwave power	Ion kinetic energy
Ar, 0.02mbar	60W	8 eV
O, 0.05mbar	50W	8 eV
H, 0.05mbar	50W	4 eV

Table D.2: Summary of the plasma parameters corresponding to the lowest ion kinetic energies, at an antenna-sample distance of 100mm.

## D.4 Cleaning parameters for the $\text{PbTiO}_3$ surface preparation

The PTO surface preparation is made of three steps.

(1) The sample is slowly heated ( $\approx 4\text{h}$ ) up to  $490\text{-}520^\circ\text{C}$  (measured using a conventional pyrometer,  $\epsilon=0.5$ ). Note that there is a large delay (several minutes) between the start of the current passing through the sample and its degazing and heating. This reactivity diminishes when the sample begins to heat, certainly due to the electron mobility increase.

(2) Still while annealing, an 50W plasma is started with a 0.05mbar O partial pressure. During the increase of the gas pressure and during the plasma, the temperature increases (correlated to a modification of the current and the voltage). We can thus imagine that this temperature increase may be due to the additional current generated by the electrons of the plasma, or due to a modification of the surface conductivity in the O atomsphere. The O plasma cleaning duration is generally smaller than 10min but rarely smaller than 2min to entirely remove the C contaminant.

(3) The O plasma is then switched off and the sample is annealed ( $\approx 550^\circ$ ) during  $\approx 30\text{min}$  to show a LEED pattern<sup>a</sup>. The sample is then quenched.

### References for Appendix D

- [1] C.Y. Zhi, X.D. Bai and E.G. Wang, Appl. Phys. Lett. **81**, 1690 (2002).
- [2] E. Picard, P. Gentile, D. Martrou and N. Magnea, Appl. Phys. Lett. **75**, 677 (1999)

---

<sup>a</sup>If the heating current is switched off directly after the plasma extinction, no LEED will be obtained.



## Remerciements

Par défaut, la physique expérimentale est le résultat d'un travail d'équipe, qui plus est lorsque les appareils de mesure fonctionnent sous vide poussé. Je voudrais donc remercier toutes les personnes qui ont contribué directement ou indirectement à ce travail de thèse.

Tout d'abord je tiens à exprimer toute ma gratitude envers mon superviseur de thèse, le Prof. Philipp Aebi pour son support scientifique et ses qualités humaines qui contribuent quotidiennement à la bonne marche et à la motivation du groupe de spectroscopie.

Je souhaiterais également remercier les membres du jury, Jean-Marc Triscone et Christophe Ballif pour avoir accepté de juger mon travail ainsi que pour m'avoir consacré une partie de leur précieux temps.

Un grand merci à Philippe Ghosez pour son expertise théorique et la transparence de ses explications.

Igualmente he de agradecer a Francisco Javier Garcia de Abajo por su ayuda con el programa EDAC y las modificaciones del código, así como por la visita a San Sebastian en el País Vasco.

Naturellement, j'aimerais également adresser un tout grand merci aux membres actuels ainsi qu'aux anciens membres du groupe "10<sup>-11</sup>". Gunnar avec qui j'ai pu partager de passionnantes discussions suivies de tests pratiques sur l'aérodynamique quantique et l'hydrodynamique différentielle. Florian pour les nombreuses discussions qui ont ponctué plus de trois ans de face à face, et pour son amitié. Corsin pour avoir partagé avec moi de nombreux résultats de son approche pragmatique et pluridisciplinaire de l'analyse des milieux air-eau. Claude et Hervé pour leur bonne humeur et les pauses *krâfé*. Christian pour m'avoir initié aux *joies* du spectromètre.

Un grand merci également à Céline Lichtensteiger et Matthew Dawber pour leurs échantillons de qualité et nos discussions stimulantes.

Merci aux membres des ateliers de mécanique et d'électronique pour leurs disponibilités et leurs compétences, en particulier Christan Hêche et Daniel Varidel.

Merci au secrétariat (pour les petits chocolats) et à l'administration qui veillent à la bonne marche de l'institut.

Et finalement, je tiens à remercier tous mes amis et mes proches pour leur soutien moral, et sans qui ce travail n'aurait pas été possible.



# Curriculum vitae

## Personal details

Family name	Despont
First name	Laurent
Date of birth	September 18, 1978
Place of birth	Fribourg, Switzerland
Citizen of	Corminboeuf FR
Marital status	Single

## Studies

2003-2007	Ph. D. student in solid state physics at the University of Neuchâtel
2003	Diploma thesis: “Photodiffraction sur couches minces de $\text{PbTiO}_3$ ” Research group of Prof. Louis Schalpbach, University of Fribourg
1998 - 2003	Studies in Physics- Mathematics, University of Fribourg
1994 - 1998	High school graduation in Fribourg, Collège Ste-Croix Baccalauréat et maturité fédérale, type C (science)

## List of Publications

- **Investigation of effective screening length in ferroelectrics by photoemission**  
L. Despont, C. Monney, C. Battaglia, H. Cercellier, M. G. Garnier, C. Lichtensteiger, M. Dawber, J.-M. Triscone, P. Aebi, *To be submitted* (2007).
- **Structural investigations of epitaxial InN by X-ray photoelectron diffraction and X-ray diffraction**  
D. Hofstetter, L. Despont, M. G. Garnier, E. Baumann, F. R. Giorgetta, P. Aebi, L. Kirste, H. Lu, W. J. Schaff, *Appl. Phys. Lett.* **90**, 052907 (2007)
- **Fermi surface of layered compounds and bulk charge density wave systems**

F. Clerc, C. Battaglia, C. Monney, H. Berger, L. Despont, M. G. Garnier, P. Aebi, *Accepted for publication in J. Phys. C* (2007).

- **Electronic structure of ZrTe<sub>3</sub>**

P. Starowicz, C. Battaglia, F. Clerc, L. Despont, A. Prodan, H. J. P. van Midden, U. Szerer, A. Szytula, M. G. Garnier, P. Aebi, *J. Alloys Compd.* **442**, 268 (2007).

- **Monodomain to polydomain transition in ferroelectric PbTiO<sub>3</sub> thin films with La<sub>0.67</sub>Sr<sub>0.33</sub>MnO<sub>3</sub> electrodes**

C. Lichtensteiger, M. Dawber, N. Stucki, J.-M. Triscone, J. Hoffman, J.-B. Yau, C. H. Ahn, L. Despont, P. Aebi, *Appl. Phys. Lett.* **90**, 052907 (2007)

- **Multiple scattering investigation of the 1T-TaS<sub>2</sub> surface termination**

L. Despont, F. Clerc, M. G. Garnier, H. Berger, L. Forró, P. Aebi, *Eur. Phys. J. B* **52**, 421 (2006).

- **Direct evidence for ferroelectric polar distortion in ultrathin lead titanate perovskite films**

L. Despont, C. Koitzsch, F. Clerc, M. G. Garnier, P. Aebi, C. Lichtensteiger, J.-M. Triscone, F.G. Garcia de Abajo, E. Bousquet, Ph. Ghosez, *Phys. Rev. B* **73**, 094110 (2006).

- **X-ray photoelectron diffraction study of ultrathin PbTiO<sub>3</sub> films**

L. Despont, C. Lichtensteiger, F. Clerc, M. G. Garnier, F.G. Garcia de Abajo, M.A. Van Hove, J.-M. Triscone, P. Aebi, *Eur. Phys. J. B* **49**, 141 (2006).

- **X-ray photoelectron diffraction study of Cu(111): Multiple scattering investigation**

L. Despont, D. Naumović, F. Clerc, C. Koitzsch, M. G. Garnier, F.G. Garcia de Abajo, M.A. Van Hove, P. Aebi, *Surf. Sci.* **600**, 380 (2006).

- **Lattice-distortion-enhanced electron-phonon coupling and Fermi surface nesting in 1T-TaS<sub>2</sub>**

F. Clerc, C. Battaglia, M. Bovet, L. Despont, C. Monney, H. Cercellier, M. G. Garnier, H. Berger, L. Forró, P. Aebi, *Phys. Rev. B* **74**, 155114 (2006).

- **Non-uniform doping across the Fermi surface of NbS<sub>2</sub> intercalates**

C. Battaglia, H. Cercellier, L. Despont, C. Monney, M. Prester, H. Berger, L. Forró, M. G. Garnier, P. Aebi, *CondMat* 0611215 (2006).

- **Fermi surface induced lattice distortion in NbTe<sub>2</sub>**  
C. Battaglia, H. Cercellier, F. Clerc, L. Despont, M. G. Garnier, C. Koitzsch, H. Berger, L. Forró, C. Ambrosch-Draxl, P. Aebi, *Phys. Rev. B* **72**, 195114 (2005).
  
- **Photoemission of a Quantum Cavity with a Nonmagnetic Spin Separator**  
C. Koitzsch, C. Battaglia, F. Clerc, L. Despont, M. G. Garnier, P. Aebi, *Phys. Rev. Lett.* **95**, 126401 (2005).
  
- **Fermi Surface Topology of Rare Earth Dihydrides**  
C. Koitzsch, J. Hayoz, M. Bovet, F. Clerc, L. Despont, C. Ambrosch-Draxl, P. Aebi, *Phys. Rev. B* **70**, 165114 (2004).
  
- **Spin-orbit splitting in the valence bands of 1T-TaS<sub>2</sub> and 1T-TaSe<sub>2</sub>**  
F. Clerc, M. Bovet, H. Berger, L. Despont, C. Koitzsch, O. Gallus, L. Patthey, M. Shi, J. Krempaski, M. G. Garnier, P. Aebi, *J. Phys.: Condens. Matter* **16**, 32713278 (2004).
  
- **Charge density waves in 1T-TaS<sub>2</sub>: An angle-resolved photoemission study**  
F. Clerc, M. Bovet, H. Berger, L. Despont, C. Koitzsch, M.G. Garnier, P. Aebi, *Physica B: Condensed Matter* **351**(3-4), 245-249 (2004).